FABRICATION OF NANO-CHANNEL TEMPLATES AND A STUDY OF THE ELECTRICAL AND MAGNETIC PROPERTIES OF NANOWIRES GROWN IN TEMPLATE PORES

Abhay Pratap Singh

Dissertation Prepared for the Degree of

DOCTOR OF PHILOSOPHY

UNIVERSITY OF NORTH TEXAS

May 2020

APPROVED:

Usha Philipose, Major Professor
Vladimir Drachev, Committee Member
Yuankun Lin, Committee Member
Arup Neogi, Committee Member
Jingbiao Cui, Chair of the Department of Physics
Su Gao, Dean of the College of Science
Victor Prybutok, Dean of the Toulouse Graduate School

Singh, Abhay Pratap. *Fabrication of Nano-Channel Templates and a Study of the Electrical and Magnetic Properties of Nanowires Grown in Template Pores*. Doctor of Philosophy (Physics), May 2020, 110 pp., 3 tables, 60 figures, 141 numbered references.

This thesis is a study of the structural, electrical and magnetic properties of indium antimonide (InSb) nanowires (NWs), that were synthesized by a template-assisted ordered growth technique via electrochemical deposition. InSb was chosen for this study because of its intrinsic properties that make it a material of choice for applications in high channel mobility, infrared (IR) sensing, thermoelectrics, and magnetoresistive sensing martials. This work has four main components: (i) Growth in commercially available anodic aluminum oxide (AAO) template, where hole-dominated conduction was observed, following NW growth in a low pH electrolyte. The challenge in using these AAO templates was in covering the back surface of the pores with a metal film. Uncovered pores resulted in electrolyte leakage and non-reproducible results. (ii) Growth in flexible polycarbonate membranes, where the flexibility of the membranes resulted in polycrystalline or high defect density NW growth. (iii) Fabrication of an AAO template, where the barrier layer thinning technique was found to be efficient in removal of the think aluminum oxide barrier that exists at the interface between the template and the aluminum metal. This allows for direct growth of NWs into the template pores without the need for metal evaporation. (iv) Fabrication of a heterostructure comprising of an InSb layer sandwiched between two ferromagnetic contacts. Preliminary results show evidence of inverse spin-valve effect at the low temperature of 4K.

Copyright 2020

by

Abhay Pratap Singh

ACKNOWLEDGEMENTS

I express my deep sense of gratitude and indebtedness to my major advisor Prof. Usha Philipose; without whose inspiring guidance and consistent interest, this project was a virtual chimera for me. It has been a memorable, everlasting experience for me to work with her benign presence and guidance. It is impossible for me to bind my reverence for her in words. I also express my sincere obligation to Department of Physics, The Toulouse Graduate School (TGS) for providing continuous financial support.

I am deeply indebted to Prof. Diana Berman who helped in the magnetization studies. Her guidance and supoort was most valuable. I also owe my gratitude to dissertation committee members Dr. Arup Neogi, Dr. Yuankun Lin, Dr. Vladimir Drachev for their invaluable support, encouraging words, and simulative discussions during my research. I would like to thank Dr. Jianchao Li for training of the clean room equipments, and Mr. Saul Sepulveda for training me to operate surface microscopy and spectroscopy systems at Materials Research Facility (MRF) in Discovery park and providing valuable help during its operation. I would like to thank professor Teresa D. Golden for her help in electrochemistry. I would like to thank Department of Physics main office, machine shop (Tracy Lynch for making different new designed equipment's) and electronics shop (Gary Karnes for making different electronic circuits) staff members. I am grateful for my friend Kevin Roccapriore for all his help in the e-beam lithography and TEM experiment and analysis. I would like to thank all my research group members Gopal, Zaina, Yan, Javier, Alex, and all senior undergraduate students(Bryan, Oscar, Gavin, Chris), and Jitendra, Urmila, Aditya, Srujan, Yuba, Satyabrata for their continued cooperation during whole project work. I express my honest goodwill for all my colleagues at the University of North Texas for their sincere endeavors during my project work. Last but not the least I would like to pay my sincere tribute to almighty, my beloved parents and family whose spiritual omnipresence was an inspiring factor to carry on all this work to a satisfactory conclusion.

TABLE OF CONTENTS

Page

ACKNOWLEDGEMENTS iii

LIST OF TABLES vii

LIST OF FIGURES viii

LIST OF ABBREVIATIONS xvii

CHAPTER 1 INTRODUCTION 1

1.1. Semiconducting Nanowires: Significance and Applications 1

1.2. Significance of InSb NWs 1

1.3. Past, Present and Future of MOSFET Devices 3

1.4. Physics of Traditional Planar Metal Oxide Field Effect Transistor (MOSFET): MOS Transistor 4

1.5. Physics of NW FET 8

1.6. Spintronics 12

1.6.1. InSb NWs Based Spin-Valve Device 13

1.7. Motivation and Thesis Outline 13

CHAPTER 2 SYNTHESIS OF INDIUM ANTIMONIDE NANOWIRES - A REVIEW, AND STRATEGIES TO ACHIEVE ORDERED GROWTH IN TEMPLATE PORES BY ELECTRODEPOSITION 16

2.1. Introduction 16

2.2. High Vacuum Epitaxial Growth Techniques 17

2.3. Chemical Vapour Deposition (CVD) Technique 18

2.4. NW Growth Mechanism 18

2.5. Growth of NWs Using Electrochemical Deposition Technique 20

2.5.1. Electrochemical Growth Mechanism: Convection, Migration, and Diffusion 22

2.5.2. Diffusion Mechanism in NW Growth Process 23
2.5.3. Convection Mechanism in Growth of NWs 25
2.5.4. Migration of Ions During Growth of NWs 27

CHAPTER 3 TEMPLATE-ASSISTED GROWTH OF INDIUM ANIMONIDE NANOWIRES IN COMMERCIAL ANODIC ALUMINUM OXIDE TEMPLATE 30
3.1. Introduction 30
3.2. Experimental Method 32
3.3. Result and Discussions 34
3.4. Conclusion 42

CHAPTER 4 ELECTROCHEMICAL GROWTH OF INDIUM ANTIMONIDE NANOWIRES INFLEXIBLE POLYCORBONATE MEMBRANE 44
4.1. Introduction 44
4.2. Experimental Method 46
4.3. Results and Discussions 48
4.4. Conclusion 63

CHAPTER 5 FABRICATION OF NANOPOROUS ANODIC ALUMINUM OXIDE TEMPLATEBASED ON BARRIER LAYER THINNING AND SYNTHESIS OF COBAL TNANOWIRES IN THE TEMPLATE PORES 64
5.1. Introduction 64
5.2. Fabrication Method 68
5.3. Conclusion 75

CHAPTER 6 MAGNETIZATION STUDIES OF PURE NICKEL AND COBALT NANOWIRES AND A STUDY OF SPIN-VALVE EFFECT IN NI-INSB-CO HETEROSTRUCTURES 77
6.1. Introduction 77
6.2. Analysis of The Magnetic Properties of Ni and Co NWs 80

6.2.1. Magnetic Measurements of Ni NWs 80
6.2.2. Magnetic Measurements of Co NWs 84
6.3. Fabrication Method of Spin-Valve Device (Ni-InSb-Co) 87
6.4. Extraction of the Spin Diffusion Length in Co-InSb-Ni NWs 87
6.5. Working of The Spin-Valve Device 88
6.5.1. Device Characterization: Magnetoresistance (Spin-Valve) of Ni-InSb-Co NWs 89
CHAPTER 7 CONCLUSION 91
7.1. Contributions 91
7.2. First Focus: InSb NW Growth in AAO Template, Highlighting Growth Mechanism and Influence of Electrolyte on NW Stoichiometry and Morphology 91
7.3. Second Focus: InSb NW Growth in Polycarbonate Template, With Detailed Study of Effect of Membrane Flexibility on NW Crystallinity 92
7.4. Third Focus: Fabrication of AAO Template with Desired Pore Size and Length Followed by Growth of InSb NWs 93
7.5. Fourth Focus: Synthesis of a NW Heterostructure of Ni/InSb/Co for Potential Use as Magnetoresistive (Particularly spin-valve) Devices 93
7.6. Future Directions 94
7.7. Publications and conferences attended during this dissertation work 94
7.7.1. Refereed publications 94
7.7.2. Conference: Contributed Oral Presentations 95
7.7.3. Poster 96
7.7.4. Summer School 96
REFERENCES 97

LIST OF TABLES

Page

Table 1.1. Physical properties of bulk semiconductors, Si and InSb 2

Table 6.1. Coercivity H_c of Ni NW at different temperatures 83

Table 6.2. Coercivity H_c of Co NW at different temperature 86

LIST OF FIGURES

Page

Figure 1.1. Schematics of MOSFETs, past on the left (Planar FET), present in the middle (FinFET), and future on the right are Gate-All-Around (GAAFET) which is cylindrical shape NWs and at right most Multi-Bridge-Channel FET (MBCFET). In the case of planar FET only 1 top gate is required, and in the case of FinFET 3 gates are requited on each channel, however in the case of GAA (NW or nanosheet) there are 4 gates are requited on each channel [1]. 3

Figure 1.2. Schematic view of a traditional planer MOSFET. 5

Figure 1.3. Transfer characteristics of MOS transistor at drain bias of 50 mV. Linear drain current is plotted on right hand side of y-axis and logarithmic on the left hand side of y-axis [2]. 7

Figure 1.4. In both cases OFF current increases when (a) drain voltage is increased from 0.05 V to 1.0 V or (b) channel length is decreased. Both are examples of drain-induced barrier lowering (DIBL) effect [2]. 8

Figure 1.5. Schematic of NW field effect transistor (NSFET), where bottom layer is made of highly doped Si and NW is lying on Si substrate separated by thin film of oxide layer. Source and drain is made of gold(Au). 9

Figure 1.6. (a) Schematic view of a cylinder (NW) lying on a plane (highly doped Si) separated by a thin film layer silicon dioxide, and (b) cross-sectional view of the plane-and-cylinder model for NW on a sample with an oxide layer (t_{ox} acting as a dielectric with R radius of NW. 12

Figure 1.7. Schematic of a spin valve response. The coercivities of two ferromagnets are |H1| and |H2|. Magnetic field is swept from left to right (red line), when it reached to + $|H_1|$ then ferromagnet 1 (FM1) switched the magnetization to up direction and high Resistance state is experienced. again, when magnetic filed reached at + $|H_2|$ then ferromagnet 2 (FM2)

magnetization switches to down and experience a low resistance state. Similarly when we sweep the magnetic field in negative direction we experience again high resistance state between - $|H_1|$ and - $|H_2|$. 14

Figure 2.1. Schematic view of chemical vapor deposition (CVD) system for growth of InSb NWs 19

Figure 2.2. Schematic view of (a) electrochemical deposition setup for NWs growth, and (b) the cross-sectional view of NWs grown in anodic aluminum oxide (AAO) template. 21

Figure 2.3. Schematic view of (a) electrochemical deposition setup for NWs growth, and (b) the cross-sectional view of NWs grown in anodic aluminum oxide (AAO) template. 22

Figure 2.4. Schematic of growth of NW in a single nanopore: (a) linear diffusion, (b) linear and semi-infinite hemispherical diffusion, and (c) semi-infinite planar diffusion outside the pore [3]. 24

Figure 2.5. Schematic of cell designs: (a) cathode over anode; (b) anode over cathode; and (c) cathode and electrode placed laterally and parallel to each other. Letter A represents working electrode (Cathode), C represents secondary electrode (Anode), and B represents reference electrode [3]. 26

Figure 2.6. Optical images of electrochemical cell with 3 electrode (a) represents one of two vertical configurations of electrodes presented in Figure 2.5 (a) Figure 2.5 (b), in this case anode is over cathode representing figure 2.5 (b), However, (b) represent the horizontal electrode configuration where cathode and anode are placed horizontally and parallel to each, which avoids the convection and migration of ions into the pores of template. Symbol "1" in black color represents the working electrode, symbol "2" in green color represents the the reference electrode, and symbol "3" in red color represents the counter electrode. 27

Figure 2.7. Schematic diagram convection in and around nanoporous pores in the

configuration of anode over cathode. [3] 28

Figure 2.8. Optical image of electrodeposition setup, (a) shows the flexible PCtemplate and SEM image of template and after NW growth and partial eching to see the NWs, (b) circilar rigid AAO template, and SEM images with blank and after NWs growth and etching where NWs are bundled. 29

Figure 3.1. Evolution of NW growth in the AAO template pores: (a) Current-time plot of InSb NW growth showing different growth regions; (b) Cross-sectional SEM image of the template in region I. The thin bottom layer is a gold film. The pores are partially filled with InSb. This region corresponds to planar diffusion inside the pore; (c) Cross-sectional SEM image of region III where NWs have filled the pores and the dome shaped tips collapse to form mushroom shaped clusters, corresponding to semi-infinite planar diffusion at the mouth of the pore. 34

Figure 3.2. SEM images of (a) InSb NWs that were removed from the AAO template and dispersed on a cleaned Si substrate. Inset shows a single NW with roughened surface; (b) EDX spectrum of Sb-rich InSb NWs. 37

Figure 3.3. Raman spectrum obtained from two crossed InSb NWs; inset shows the region from where the Raman spectrum was collected. The two peaks at 150 and 110 cm^{-1} are most likely related to surface roughness and defects in the NW. The characteristic TO, LO peaks attest to crystallinity of the InSb NWs. 38

Figure 3.4. (a) Schematic of back-gated InSb NW field effect transistor, (b) SEM image of a single InSb NW contacted by two Cr/Au contacts. 39

Figure 3.5. Transfer characteristics of InSb NW back-gated FET at increasing V_{ds} from 0.2 V to 1.0 V. Inset shows a logarithm plot of the $I_{ds} - V_{gs}$ curve at $V_{ds} = 1.0$ V. The on-off current ratio is estimated to be of the order of 10^3. 40

Figure 3.6. (a) Temperature dependent I-V shows current increasing with

temperature, which is characteristic semiconducting behavior. (b) Temperature dependent conductivity measurements (Arrhenius plot) for the extraction of activation energy from a single InSb NW. Inset shows normalized resistance vs. temperature which shows the exponential decrease of resistance with increasing temperature. 42

Figure 4.1. Results from cyclic voltammogram showing variation of current with positive (oxidizing) potentials and negative (reducing) potentials. Increasing the negative potential beyond -1.5 V leads to hydrogen evolution. 49

Figure 4.2. Current transient of room temperature InSb NW growth in Au-coated polycarbonate membrane at three different deposition potentials: -1.0 V, -1.25 and -1.50 V. 51

Figure 4.3. SEM images of blank polycarbonate membrane before and after growth of InSb NWs (a) SEM image of bare polycarbonate template (b) Zoomed in SEM image of polycarbonate template with different diameters and shapes of pore, ranging from $\sim 150 - 200$ nm (c) SEM image of InSb NW exposed tips after 30 seconds of oxygen plasma etching, and (d) Zoomed in SEM image of exposed tips of InSb NWs. 52

Figure 4.4. (a) SEM images of bundle of InSb NWs after drop casting on silicon wafer (b) EDX spectrum of a single and short ($\sim$5 μm) InSb NW, that is shown in the inset of figure (b). 53

Figure 4.5. Raman spectrum of electrochemically grown InSb NW in porous polycarbonate template. (a) At a deposition potential of -1.0 V, spectrum shows characteristic defect related peak at 147 cm^{-1} and around cm^{-1}. No peaks were observed in the $180 - 190$ cm^{-1} range, which is the region where peaks corresponding to crystalline InSb are typically measured; (b) Spectrum obtained for growth at -1.25 V shows similar defect related peaks as observed in (a). Absence of any peak in the $180 - 190$ cm^{-1} range

(c) Spectrum obtained from NWs grown at -1.5 V. Well-defined peaks were observed at 149 cm^{-1} , around 120 cm^{-1} and around 181 cm^{-1}. The zoomed in Raman spectrum image shows two distinct peaks at 180.5 $cm^{-1}$and 188.7 cm^{-1} which is assigned to the c-InSb TO and LO phonon modes, respectively. In all three cases, the Raman peaks measured in the range from 145 – 149 cm-1 is attributed to TO-TA modes and is believed to originate from defects in the NWs, as is the peak around 119.7 cm^{-1}. 54

Figure 4.6. XRD spectrum of as grown InSb NW in polycarbonate template. 56

Figure 4.7. STEM images taken along a single InSb NW clearly showing the presence of an amorphous oxide shell: (a) ABF-STEM image of a relatively smooth NW that shows several crystal grains; inset shows FFT of the image indicating multiple crystallographic orientations; (b) magnified HAADF-STEM image of outlined region in (a), looking down the (111) direction of one of the larger grains, with a measured distance of 0.25 nm; (c) selected area diffraction pattern (SAED) shows indexed rings with discrete spots confirming polycrystalline nature of the NW. 57

Figure 4.8. (a) HAADF-STEM image taken from a significantly rougher NW; (b) HAADF image of outlined region in (a) showing presence of crystal defects which accounts for the observed roughness in the NW; (c) magnified HAADF image of (b) showing twin planes and stacking faults. 58

Figure 4.9. A schematic of the 'nucleation-coalescence' growth mechanism, where: (a) a few monolayers of InSb grow on the Au electrode; (b) islands from over the monloayer; (c) coalescence of the islands to form individual crystals/grains. 59

Figure 4.10. SEM image of single InSb NW contacted by four Ni electrodes. The NW was placed on a 200 nm thick silicon dioxide (SiO_2) grown over a highly dopedp^+ Si substrate. The channel length between each electrode is about 1.5 μm. The metal electrodes are Cr (5 nm)/Ni (200 nm). Cr enables

better adhesion of Ni film on the SiO_2 layer. 61

Figure 4.11. Current-voltage measurements on a single as-grown Insb NW. the NW diameter and electrode spacing are 190 nm and 1.5 μm respectively. (a) Symmetric non-linear I-V curve on linear scale. The curves are linear (ohmic) at small bias and transforms at high bias; (b) I-V curves plotted on a logarithmic scale, showing a crossover to SCLC at $V_x = 0.14$ V. 62

Figure 5.1. SEM images of top and bottom surfaces of AAO template (a) top surface at scale bar of 1 μm and (b)bottom surface with scale bar 2 μm, and after 800 mg of Au thermal evaporation (c) bottom surface at scale bar of 1 μm (d) bottom surface at scale bar of 500 nm. Open pores in (c), and (d) even after 800 mg of Au evaporation, is not ideal for electrochemical growth of NWs 65

Figure 5.2. SEM images of bottom surfaces of AAO template after ($\sim$ 500 nm) e-beam evaporated Au thin film. We can clearly see that pores are not completely filled. 66

Figure 5.3. SEM images of InSb NW grown in AAO template. Rough notched on the surface of NWs are shown by red arrows comes from the morphology of interior of AAO template 67

Figure 5.4. SEM image of polycorbonate (PC) template, zoomed in image shows the non-unoform pores of PC temnplate where pore are ranging from $\sim$ 150 to 200 nm in diameter. 67

Figure 5.5. Optical images of 2×2 cm^2 aluminum coupon at different stages of fabrication process of home-made AAO template (a) just after chemical polishing for smother surface of aluminum foil, (b) aluminum foil after the first step anodization, (c) aluminum foil after the second step anodization, and (d) circular AAO template separated from the aluminum foil after etching of aluminum using 1M $HgCl_2$ solution. 68

Figure 5.6. SEM images of top surfaces of AAO template (a) at scale bar of 2 μm and

(b) with scale bar 500 nm in pore diameter which shows that diameter of pore is ∼ 50 nm [3]. 69

Figure 5.7. SEM images of bottom side of AAO template: (a) hemispherical cap of barrier layer formed during anodization and (b) complete barrier lay er etching in 5% phosphoric acid at 30^0 C for 30 min. [3]. 70

Figure 5.8. SEM images of bottom and top surfaces after etching in 5% phosphoric acid (H_3PO_4) for 35 min at 30°C. (a) SEM image of bottom surface, which shows all the barrier layers are etched and pores are uniformly open and (b)SEM image of the same sample as in (a), which shows over etching of top surface which looks like pores are bundled together [3]. 71

Figure 5.9. SEM images of cross-section of home-made AAO template: (a) shows ∼50 μm long pore which was obtained after 250 min of second anodization, and inset shows smooth and straight pore and (b) shows 5-µm long pore which was obtained after 25 min of second anodization [3]. 72

Figure 5.10. SEM images of top surface of AAO template: (a) shows nonporous hexagonal AAO pores without any etching, (b) after 17 min etching in 1 M phosphoric acid at 30^0C and, (c) after 20 min etching in 1 M phosphoric acid at 30^0C [3]. 72

Figure 5.11. Schematic plot of voltage reduction steps vs time for thinning/rupturing the barrier layer at the bottom of the AAO pore. First, aluminum (99.999% was anodized (second anodization) for 250 min to grow 50 μm long pore at the rate of 1 μm/5 min at 40 V in 0.3 M oxalic acid ($C_2H_2O_4$) with platinum mesh as a counter electrode at room temperature. afterword, voltage was stepped down from 40 to 10 V in decrements of 0.1 V/ sec. 73

Figure 5.12. (a) Optical image of AAO grown on aluminum foil after barrier layer thinning and electrodeposition of InSb NWs, only top portion of AAO is filled with NWs. (b) SEM image of top of the AAO surface where there is

no growth of NWs, (c) SEM image of top surface of AAO (black region in (a) after partial etching with phosphoric acid, where bundles of wires are clearly visible, (d) optical image of bottom of the AAO template after aluminum removal in 1 M mercury(II) chloride, white area in (d) is the area where barrier layers (pores) are not open, (e) SEM image of the NW area in (d) where hemispherical closed tips are shown, and (f) SEM image of dark area in (d) where barrier layers are open. 74

Figure 5.13. SEM images of top surface of AAO templates (a) before etching and after 2nd anodization and BLT at scale bar 1 μm, (b) before etching and after 2nd anodization and BLT at scale bar 500 nm, (c) after etching and BLT at scale bar 1 μm, and (d) after etching and BLT at scale bar 500 nm 75

Figure 5.14. SEM image of bottom side of AAO template after aluminum removal in mercuric chloride. All the pores are open and suggesting this technique can be used to grow the NWs directly on anodized aluminum substrate. 76

Figure 5.15. Schematics of AAO template (left) after BLT where barrier layers are removed, and cross-section of AAO template after heterostructure (Ni-InSb-Co) NW growth. Length of each NW can be controlled via electrodeposition time. 76

Figure 6.1. Schematic diagram of an InSb spin-valve device. Bottom layer is coated with gold thin layer before electrodeposition of the NWs. Top and bottom contact were using metal wire to connect external circuit. 79

Figure 6.2. Schematic of pure Ni NWs, electrochemically grown in $\sim$ 20 μm long pore length of PC template with diameter ranging from $\sim$ 150 nm to 200 nm. 80

Figure 6.3. (a) SEM image of pure Ni NWs electrochemically grown in PC template. (b) EDX spectrum shows only Ni peak. 81

Figure 6.4. Magnetization hysteresis curve of Ni NWs array with applied field parallel to the wire axis.Magnetic hysteresis loop of Ni NWs at different temperatures (4, 50, 100, 150, 200, 250, and 300K) (a) magnetic field

applied from -10000 Oe to +10000 Oe, (b) Zoomed in data of magnetic field applied from -1000 Oe to +1000 Oe. We can see the coercivity of Ni NWs array is decreasing with increasing temperature. 82

Figure 6.5. Magnetization hysteresis curve of Ni NWs array with applied field parallel to the wire axis. 83

Figure 6.6. Schematic of pure Co NWs, electrochemically grown in $\sim$ 20 μm long pore length of polycarbonate (PC) template with diameter ranging from $\sim$ 150 nm to 200 nm. 84

Figure 6.7. (a) SEM image of pure Ni NWs electrochemically grown in PC template. (b) EDX spectrum shows only Ni peak. 84

Figure 6.8. Magnetization hysteresis curve of Co NWs array with applied field parallel to the wire axis. Magnetic field is applied parallel to the NW axis. (a) Hysteresis curve from -1 T to +1 T, (b) zoomed in version of data between -0.5 T to +0.5 T. 85

Figure 6.9. Temperature dependence of remnant magnetization(M_r) coercive field (H_C) of Co NWs array. 86

Figure 6.10. (a) shows the sample holder and electrical connections and (b) shows the I-V curve at the room teplerature. 88

Figure 6.11. Inverse spin valve effect at 4K. This data was collected at a bias current of 10 μA 88

Figure 6.12. Inverse spin valve effect at 4K. This data was collected at a bias current of 10 μA 89

Figure 6.13. Inverse spin valve effect at room temperature (300K). This data was collected at a bias current of 10 μA 90

LIST OF ABBREVIATIONS

NWs	Nanowires
InSb	Indium antimonide
Au	Gold
Ni	Nickel
Co	Cobalt
Cr	Chromium
Al	Aluminum
FET	Field effect transitor
MOSFET	Metal oxide semiconductor field effect transitor
NWFET	Nanowire field effect transistor
BGNWFET	Back-gated nanowire field effect transistor
GAA	Gate-all-around
ECD	Electrochemical deposition
AAO	Anodic aliminum oxide
PC	Polycarbonate
Al_2O_3	Aluminum oxide
BLT	Barrier layer thinning
SCLC	Space charge limited current
SEM	Scanning electron microscope
EDX	Energy dispersive X-ray
TEM	Transmission electron microscope
XRD	X-ray diffraction
MR	Magneto resistance
n_e or n_0	Carrier concentration in semiconducting materials
μ_{FE}	Field effect mobility
MBE	Molecular beam epitaxy
MOCVD	Metal organic chemical vapour deposition

CVD	Chemical vapour deposition
PVD	Physical vapor deposition
PMMA	Polymethyl methacrylate
PR	Photo-resist

CHAPTER 1

INTRODUCTION

1.1. Semiconducting Nanowires: Significance and Applications

Semiconductor nanowires (NWs) have awakened a lot of scientific interest and are regarded as one of the most promising candidates as possible building blocks in future nanoelectronics.

The significance of this class of materials arises from the fact that they are one-dimensional (1-D) materials with high surface to volume ratio. Typically their lengths range from one to several tens of microns. However, to be considered as NWs, their diameters are in the range of nanometers (nm). NWs are very thin and long semiconductor crystals in cylindrical form (1-D). In bulk materials, when growing heterostructures, the lattice-mismatch between different materials can cause challenges due to large strain energies at the interfaces resulting in defects and dislocations which are detrimental for the device performance. The extremely small volume of the nanostructures resulting from their small radial dimension relaxes the requirement for lattice-matching in heterostructure NWs. It is therefore possible to fabricate devices where different materials are sandwiched together to exploit the unique properties of each to achieve a certain functionality.

Another significant advantage of NWs is their vertical geometry which allows fabrication of vertical transistors where the gate length can be controlled accurately. It is also possible to have wrap-around gate electrodes. The NW geometry is therefore ideal for fabricating tunneling field effect devices. The ability to combine lattice-mismatched materials and the cylindrical NW geometry facilitating gate positioning at the tunneling junction coupled with one-dimensional electron transport allows for a potential breakthrough in electronic device performance.

1.2. Significance of InSb NWs

Since scaling of planar Si-CMOS devices is not a viable long-term option, several approaches to achieve improved electronic and spintronic devices are being investigated. As

part of this effort, this dissertation work focuses on the benefits of synthesizing and fabricating devices based on a popular group II-V semiconductor - Indium Antimonide (InSb).

An important parameter that governs the use of a material system in the fabrication of electronic devices like transistors is the speed with which electrons can move across a given length, since this determines how fast the transistor can respond to a varying gate potential. So, the electron transport properties of carriers in a semiconductor are determined by its carrier mobilities: electron mobility (μ_e) and hole mobility (μ_h). InSb has an extremely high electron mobility, roughly 55 times greater than bulk electron mobility compared to Si. The intrinsic properties of InSb are as indicated in Table 1.1.

TABLE 1.1. Physical properties of bulk semiconductors, Si and InSb

Parameter	Si	InSb
Lattice constant a_0 (A^0)	5.431	6.479
Energy band gap E_g (eV)	1.12	0.17
Electron mobility μ_e (cm^2/Vs)	1400	77000
Hole mobility μ_h (cm^2/Vs)	450	850
Conduction band effective mass m^c_{eff}	$m_e = 98$	1.4
	$m_h = 19$	

Despite its attractive properties, it is highly unlikely that InSb will replace Si in large scale electronic circuits. This is because Si wafers are the only economically viable option for mass production. Semiconductors like InSb have relied on expensive synthesis strategies. Moreover, there are years of research and billions of dollars already invested into Si-based device technology. The focus of this thesis is to demonstrate the ability to synthesize large arrays of InSb NWs using relatively inexpensive growth techniques. The device potential of this material for electronic and spintronic devices will also be demonstrated. Interest in InSb is triggered by the fact that it is the lowest narrow band gap semiconductor, has highest carrier mobilities and lowest charge carrier effective masses and very high lattice constant. On account of its small electron effective mass, InSb exhibits quantum confinement effects

in much larger structures since its Bohr radius is ≈ 60 nm. So, quantum confinement or size-effects are observable in NWs as thick as 60 nm in diameter.

1.3. Past, Present and Future of MOSFET Devices

The design, architecture, size and density of MOSFETs have been continuously evolving, as shown in Figure 1.1 . From planar design (where only 1 gate on the channel) to FinFET , three sides of channel are surrounded by gate electrodes. This three sides of gate electrode in FinFET enhance the gate controllability of channel charge, improves the performance, reduce leakage current and ultimately reduces the gate length scaling. Due to all above quality, FinFETs have allowed successful scaling of technology upto 14 nm and beyond. However, further scaling is reaching to its technological limit, and operating voltage at this scale is extremely challenging. To circumvent this limit, Gate-All-Around (GAA) FETs have been introduced by researcher and semiconductor industries. This GAAFETs , allow a significant improvement on performance with reduced operating power [1]. There are

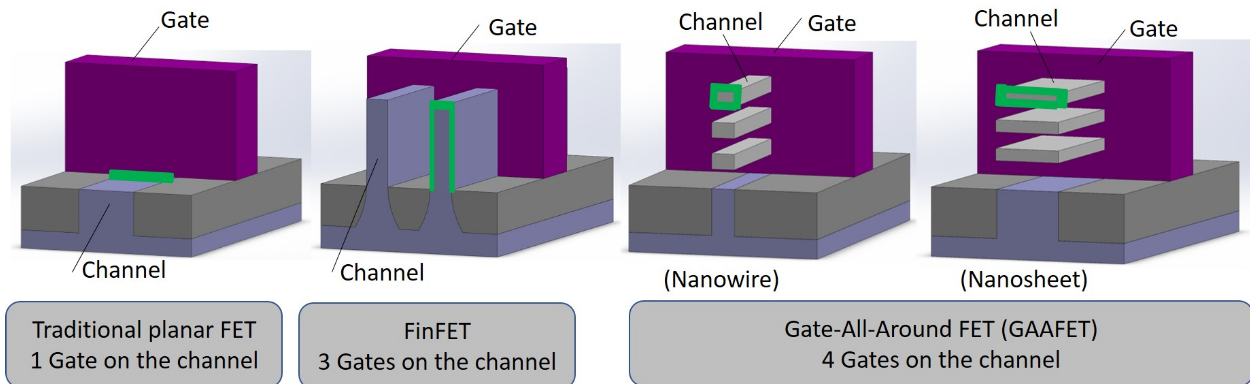

Figure 1.1. Schematics of MOSFETs, past on the left (Planar FET), present in the middle (FinFET), and future on the right are Gate-All-Around (GAAFET) which is cylindrical shape NWs and at right most Multi-Bridge-Channel FET (MBCFET). In the case of planar FET only 1 top gate is required, and in the case of FinFET 3 gates are requited on each channel, however in the case of GAA (NW or nanosheet) there are 4 gates are requited on each channel [1].

many challenges and difficulties as the processing continues with relentless focus on Moore's Law of transistor scaling. However in recent years, there has been less focus on scaling and more importance on performance such as engineering of high k-metal gates.

1.4. Physics of Traditional Planar Metal Oxide Field Effect Transistor (MOSFET): MOS Transistor

A schematic of a metal oxide semiconductor field effect transistor (MOSFET) device is shown in Figure 1.2. The MOSFET in this case consists of a p-type semiconductor substrate in which two n^+ or n-type regions have formed via ion implantation of pentavalent impurity atoms (for example: Phosphorus (P), Arsenic (As), Antimony (Sb), and Bismuth (Bi)). These n-type regions function as the source and drain electrodes. Silicon is used as a typical semiconducting material, even though germanium (Ge), silicon germanium alloys (SiGe), indium arsenide (InAs), and indium gallium arsenide (InGaAs) can also be used as other semiconducting materials for FET applications [2, 4].

A "gate dielectric", is a thin layer of insulating material which covers the region between the source and drain. Silicon dioxide (SiO_2) was used as a standard dielectric for many years. However in recent years, silicon oxynitride (SiON) and stacks (lower and upper interface of high dielectric layer) composed of insulators with high dielectric constant known as "high-κ dielectrics" have become common. Hafnium oxide (HfO_2) is an example of high-κ dielectric ($\kappa = \sim 22-25$) [5] material which has dielectric constant approximately five times higher than SiO_2 ($\kappa = \sim 4.5$) [6].The "gate" electrode is formed by deposition of metal on the top of gate dielectric.

To explain the operation of a planar MOSFET, we consider the case when the p-type substrate and the source are held at zero bias ($V_{SUB} = V_S = 0$ V), and a positive drain voltage (V_D) is applied. The gate bias is also set at 0 V. This transistor has two p-n junctions: substrate-source and substrate-drain. A space charge region exists around the drain and the source electrodes. The width of this space-charge region can be modulated by an applied bias. When the drain is positive with respect to the substrate (held at 0V), no current flows between the drain and the substrate because the drain p-n junction is reverse

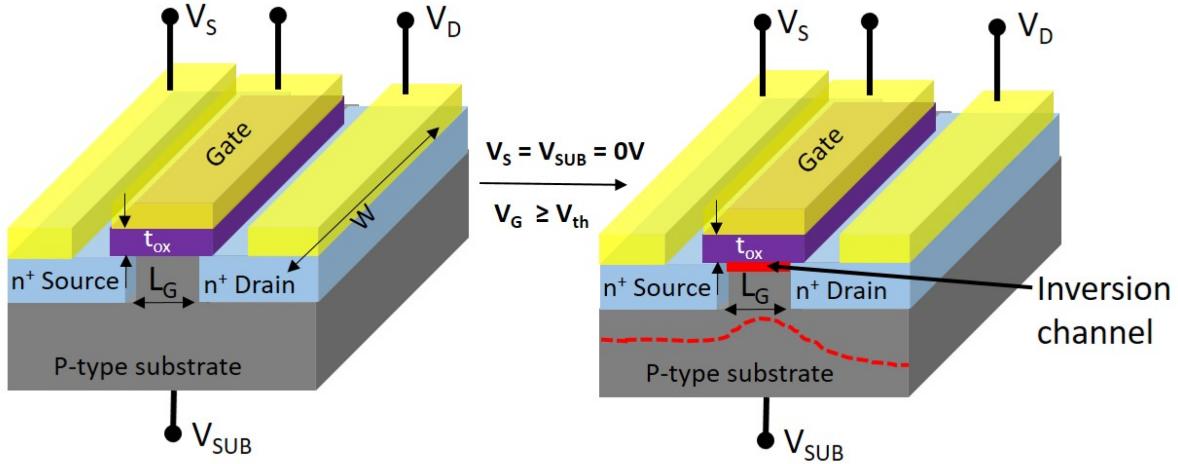

FIGURE 1.2. Schematic view of a traditional planer MOSFET.

biased. Since the substrate and source are held at 0 V, there is no current flowing across the source pn junction too. As a result, there is no current flow between the source and the drain. The transistor is in "OFF" state, acting as an open switch.

If a positive bias is applied to the gate, the holes which are the majority carriers in the p-substrate underneath the gate are repelled away from the surface and a "depletion region" that is void of holes is created in the region below the gate. The depletion region width is dependent on the p-type doping concentration and the magnitude of the positive gate voltage. When the gate bias reaches a critical threshold voltage, the depletion region width reaches a maximum and cannot be further controlled by the gate bias. Under this condition, the gate-induced depletion region merges with the source and drain junction depletion region that exists on the source and drain side of the device. It is therefore noted that the channel is pinched off near the drain as the depletion region width increases for increasing drain voltage ($V_D > V_G - V_{TH}$) and the drain current saturates (i.e. no longer increase in drain current with increasing drain voltage V_D. In this scenario, the ""saturation" drain current is given by

$$I_{Dsat} = \frac{1}{2}\mu C_{ox}\frac{W}{L}(V_G - V_{TH})^2 \qquad (1)$$

At any gate bias greater than the critical threshold gate voltage, electrons that are

the majority carriers in the source and drain electrodes are attracted towards the gate and form an electron-rich layer underneath the gate insulator. This layer is called an "inversion channel", because the channel that originally had holes as the majority carrier is now void of holes and rich in electrons, implying that the channel region is converted from p-type to n-type, with electrons tunneling between the source and drain electrodes. Under this condition, the transistor is in an "ON" state and behaves like a closed switch.

The MOSFET is not a perfect switch because even in the OFF-state there is a small current flow. Moreover, the switching from "OFF" to "ON" state does not occur suddenly at a specific gate voltage; rather there exists a range of gate voltage values, over which the switching takes place. The variation of drain current with gate voltage at a fixed value of drain voltage (50 mV) is shown in Figure 1.3. As seen in the Figure 1.3, the ON current is ∼1 mA and the OFF current is ∼50 pA. The right side axis of this plot shows the variation in a linear scale. In this scale, there is negligible drain current below a certain gate voltage. This gate voltage is called the "threshold gate voltage" and in the cited example, the value is ∼0.5 V. For low drain voltage (∼ 50 mV in this case), the drain current increases linearly with gate bias above threshold voltage. .

The "linear" or "non-saturation" current, is expressed as: [7]

$$I_{D(lin)} = \mu C_{ox} \frac{W}{L} \left[(V_G - V_{TH}) V_D - \frac{1}{2} V_D \right] \tag{2}$$

where μ, C_{ox}, L, W, V_G, V_{TH}, and V_D are the carrier mobility in the channel ($m^2V^{-1}s^{-1}$), the gate capacitance (Fm^2), the gate length (m), the the gate width (m), the gate voltage (V), the threshold voltage (V), and the drain voltage (V) respectively. As described in the device design, it is assumed that the source and substrate are grounded.

The left side of the plot in Figure 1.3 shows the dependence in logarithmic scale, where the drain current is seen to vary exponentially with gate voltage below threshold, but the "OFF" current is not equal to zero. The "sub-threshold slope" (also called sub-threshold swing (SS)) is a parameter that describes rate of increase of current below threshold gate voltage: $SS = dV_G/d(log(I_D))$. A typical value for SS slope of a bulk MOSFET is ∼ 80 mV

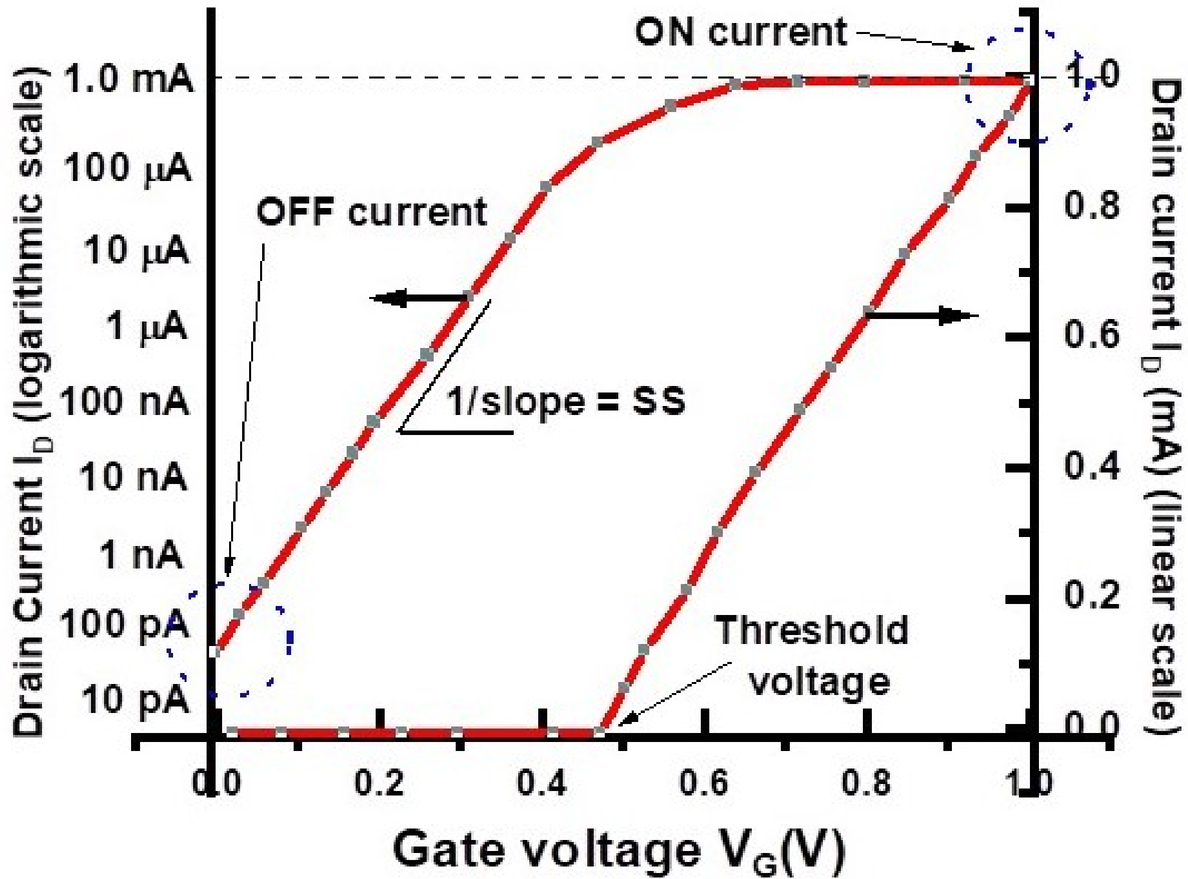

FIGURE 1.3. Transfer characteristics of MOS transistor at drain bias of 50 mV. Linear drain current is plotted on right hand side of y-axis and logarithmic on the left hand side of y-axis [2].

/dec, which means that an 80 mV increase of the gate voltage results in a tenfold increase of drain current.

In reality, the gate control of the channel region in a practical MOSFET is not perfect. This is due to the electrostatic coupling between the substrate through depletion layer. The value of SS can be reduced by impact ionization effects [8, 9], quantum tunneling effects [10, 11, 12], and by using ferroelectric gate materials [13], but none of these techniques have delivered success. This fundamental challenge for the MOSFET design is referred to as the "Boltzmann tyranny" [14, 15]. The limitations in terms of time period of scaling [16], and improved performance in terms of microprocessor clock frequency, has reached its limit due to the so-called "short channel effect"; an effect the arise due to very small

separation between source and drain. Short channel effect increases as devices are scaled down in length. The consequence of short channel effect is evident in Figure 1.4 (a), where any increase in the drain voltage results in a decrease in the threshold voltage, but there is a simultaneous increase in the "OFF" current. This is not desirable. Similarly, in Figure 1.4 (b), as the channel length is reduced the "OFF" current increases by orders of magnitude, an undesirable effect.

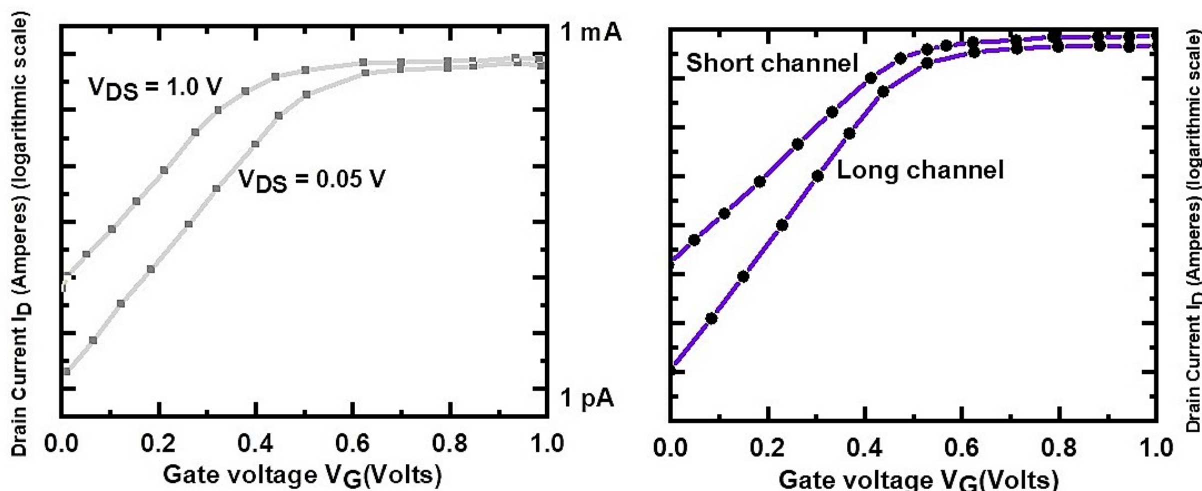

FIGURE 1.4. In both cases OFF current increases when (a) drain voltage is increased from 0.05 V to 1.0 V or (b) channel length is decreased. Both are examples of drain-induced barrier lowering (DIBL) effect [2].

It is therefore evident that a novel design involving low-dimensional materials with unique electronic properties needs to be developed to address challenges faced by the planar MOSFET technology.

1.5. Physics of NW FET

Back-gated geometry is generally used for NW field effect transistor as shown in Figure 1.5. This requires relatively little effort during fabrication compared to top-gated NW FET. It involves creating source-drain electrodes on a highly doped Si (p-type or n-type) substrate coated with thermally grown dry silicon dioxide (SiO_2) to act as a the metallic gate and gate dielectric, respectively.

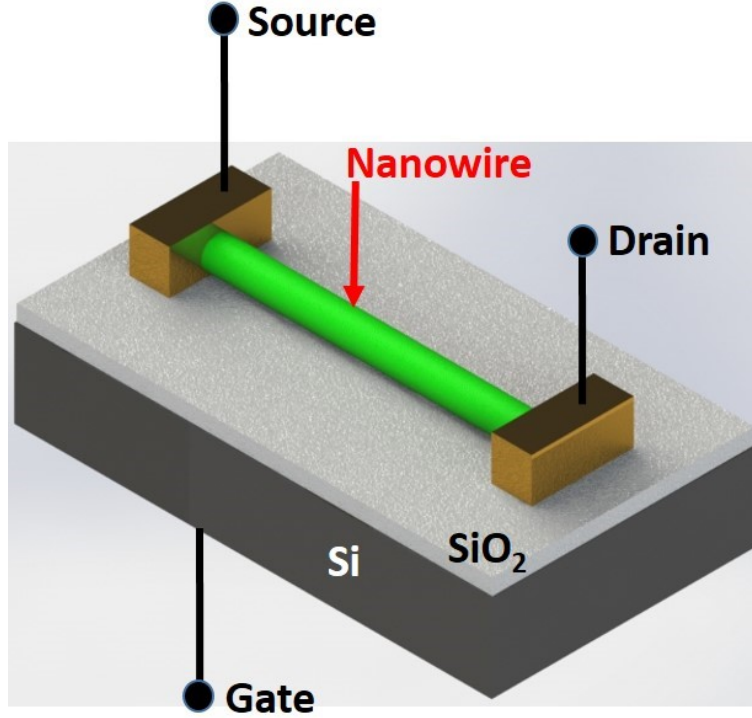

FIGURE 1.5. Schematic of NW field effect transistor (NSFET), where bottom layer is made of highly doped Si and NW is lying on Si substrate separated by thin film of oxide layer. Source and drain is made of gold(Au).

In an FET device, the most important parameter is the field effect mobility and to determine this, the device with three contacts is modelled as a NW field effect transistor (NWFET). In this model, represented by Figure 1.5, the NW is the channel, the Au contacts are our source and drain, and the Si substrate serves as a back gate. The current between the source and drain is expressed as:

$$I_{DS} = \int qnv_d dA \tag{3}$$

where q is the carrier charge, v_d is drift velocity, A is the cross-sectional area of the NW, and n is the number of carriers per unit volume. The drift velocity v_d is expressed by the equation:

$$v_d = \mu_{FE} E \tag{4}$$

where the electric field E is caused by the potential difference between the source and

the drain. So, E = V_{DS}/L where L is the gate length. Equation (3) can be rewritten as:

$$I_{DS} = \int \frac{qn\mu_{FE}V_{DS}}{L} dA \tag{5}$$

Defining the accumulation charge Q_{acc}

$$\int qndA = \frac{Q_{acc}}{L} \tag{6}$$

Equation 5 is rewritten as:

$$I_{DS} = \frac{\mu_{FE}Q_{acc}V_{DS}}{L^2} \tag{7}$$

According to S. Dayeh et al. [17], the accumulation charge can be expressed in terms of experimental parameters as $Q_{acc} = C(V_{GS} - V_t)$, where C is the capacitance between the gate and the NW and V_t is the threshold voltage. Using these equations, the field effect mobility can be expressed as:

$$\mu_{FE} = \frac{L^2}{CV_{DS}(V_{GS} - V_t)/I_{DS}} \tag{8}$$

Assuming a negligible contact resistance and defining transconductance as $g_m = \frac{\partial I_{DS}}{\partial V_{DS}}$, the field effect mobility equation is rewritten as:

$$\mu_{FE} = \frac{g_m L^2}{CV_{DS}} \tag{9}$$

A few basic assumptions were made related to negligible contact resistance and effect of interface states.

The second important parameter that can be calculated with the NW in an FET type configuration is the carrier concentration. The number of carriers N is expressed as the ratio of the total charge Q and the charge per carrier (q). The carrier concentration by definition is $n = Q_{tot}/qV$. For the gated NW shown in the schematic of Figure 1.6, $V = \pi R^2 L$. Assuming $Q_{tot} = Q_{acc}$, the carrier concentration n is defined as:

$$n = \frac{C(V_{GS} - V_t)}{q\pi R^2 L} \tag{10}$$

The absolute value of $V_{GS} - V_t$ is considered since the majority carriers could be either electrons or holes.

Since equations 9 and 10 for field effect mobility and carrier concentration contain the capacitance of the device, a strategy has to be developed for determining device capacitance. To determine the FET device capacitance, the NW is considered as a conducting cylinder that is sitting on plate (highly doped Si substrate) which is coated with a dry oxide (SiO_2) thin film. To obtain the capacitance of cylinder on plane separated by an insulating oxide layer, we must start with the definition of the capacitance between two electrodes:

$$C = \frac{Q}{\phi_a - \phi_b} \tag{11}$$

where Q is the total charge on the electrode and $\phi_a - \phi_b$ is a potential difference between the two electrodes. For our purpose, we will take C equal capacitance per unit length. then our equation will be changed to:

$$C = \frac{\rho_l L}{\phi_{cyl} - \phi_{pln}} \tag{12}$$

where ρ_l is charge per unit length and $\phi_{cyl} - \phi_{pln}$ is potential difference between a NW, modeled as a conductive cylinder of radius R, and a plane conductor. First, we will discuss the potential for the cylinder, which requires that we use the method of images. The potential at a distance r from a line charge can be taken as $\phi = \int_{r_0}^{r} Edr$ where E is the magnitude of the electric field due to the line charge. since $E = \frac{\rho_i}{2\pi\epsilon r}$, $\phi = \frac{\rho_i}{2\pi\epsilon} ln(\frac{r_0}{r})$. If this is true and we take $\rho_i = -\rho_l$, then $\phi_{cyl} = \frac{\rho_l}{2\pi\epsilon} ln(\frac{r_i}{r})$. Due to the nature of the method of images, triangle OPP$_i$ and OP$_l$P are similar. Thus, $\frac{r_i}{r} = \frac{R}{2d+d_i}$. Also, d$_i$ will get smaller as $\frac{t_{ox}}{R}$ gets larger. Thus, if $\frac{t_{ox}}{R} \ll 1$, then d $\approx$ t$_{ox}$+R and $\frac{R}{2d+d_i} \approx \frac{R}{2d}$.We know that $\phi_{pln} = 0$ because for a point charge near a conducting plane, the potential on the surface of the plane is zero. Therefore,

$$C = \frac{\rho_l L}{-\frac{\rho_l}{2\pi\epsilon} ln(\frac{R}{2d+d_i})} = \frac{2\pi\epsilon L}{ln(\frac{2d}{R})} \tag{13}$$

We know that: $ln(x + \sqrt{x^2 = 1}) = cosh^{-1}(x)$, since we are assuming $\frac{t_{ox}}{R} \gg 1$, then

$$ln\left(\frac{2d}{R}\right) \approx ln\left[\frac{d}{R} + \sqrt{\left(\frac{d}{R}\right)^2 + 1}\right] \tag{14}$$

$$ln\left(\frac{2d}{R}\right) \approx cosh^{-1}\left(\frac{d}{R}\right) \tag{15}$$

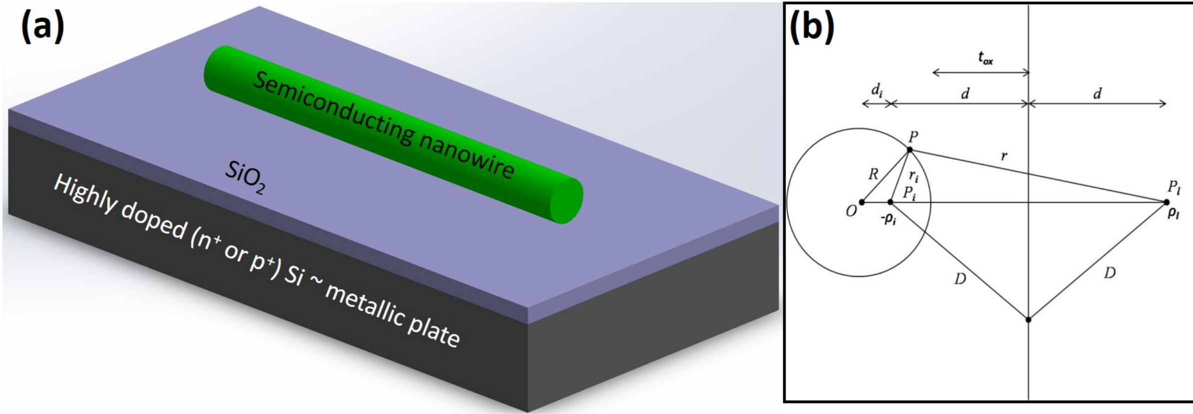

FIGURE 1.6. (a) Schematic view of a cylinder (NW) lying on a plane (highly doped Si) separated by a thin film layer silicon dioxide, and (b) cross-sectional view of the plane-and-cylinder model for NW on a sample with an oxide layer (t_{ox} acting as a dielectric with R radius of NW.

$$ln\left(\frac{2d}{R}\right) \approx cosh^{-1}\left(\frac{t_{ox}+R}{R}\right) \tag{16}$$

Thus,

$$C = \frac{2\pi\epsilon_0\epsilon_r L}{cosh^{-1}\left(\frac{t_{ox}+R}{R}\right)} \tag{17}$$

In order to arrive at this equation, a couple of assumptions had to be made. Firstly, we had to assume that the NW would act as a conductor. This assumption must be made in order to treat the NW and the substrate as a capacitor. In practice, there are several NWs that do meet this requirement, so this is a reasonable assumption. We also had to assume that the thickness of the oxide dielectric far exceeds the radius of the NW in question. This also is a reasonable assumption since in many cases, $\frac{t_{ox}}{R} > 6$.

1.6. Spintronics

Electronic and spintronic devices use the same elementary particles, electrons, for their operation. However, they use a different fundamental property of the particle. In electronics it uses the charge and in spintronics it uses the angular momentum, also better known as spin. For the latter, placing the particle in a magnetic field results in a coupling of its magnetic moment (generated by its spin) to the magnetic field. If now the spin is

measured we obtain only two possible states, the spin-up state and the spin-down state. This last spintronic property can be used to perform Boolean logic operations, in a similar way as is already done in nowadays computer chips. For this type of logic operations two states are needed, a zero and a one state. This can be easily found in a spintronic device just by assigning the spin-down state to the zero and the spin-up state to the one state. However, to be able to create a computer chip containing only spintronic devices it is necessary to build fundamental spintronic devices in which the spin state can be manipulated [18, 19].

1.6.1. InSb NWs Based Spin-Valve Device

Electron has both property spin and charge and in spintronics we can exploit the spin property of electron in addition to charge. The change in resistance of a material when placed in a magnetic field is described by the phenomenon of giant magnetoresistance (GMR). In this thesis, the GMR effect of InSb NW array and single NWs will be studied. A simple schematic shown in Figure 9 below shows the case where electrons with spin oriented parallel to the magnetization of the metal have a lower resistance than those whose spins are oriented anti-parallel. Experiments have shown that in bulk materials, due to the presence of magnetic domains, it is difficult to align the spins with perfectly parallel or anti-parallel alignment. However, with 1-D NWs, the diameter and morphology can be controlled such that the NW is a single crystal and hence a single domain. Thus, it should be possible to enhance the amplitude of the GMR effect in nanostructured materials.

Experimental detail and results of tri-layer (Ni-InSb-Co) magnetoresistance will be presented in detail in chapter 6.

1.7. Motivation and Thesis Outline

The scope of this thesis is fourfold. At the heart of this thesis is understanding the synthesis mechanism of semiconducting InSb NWs using a template assisted electrodeposition approach.To show that the synthesized NWs can be integrated in nano-micro and macro circuitry, the insertion of these wires was manipulated by drop cost followed by UV-lithography or e-beam lithography. A direct application using a single InSb NW in a back-gated field

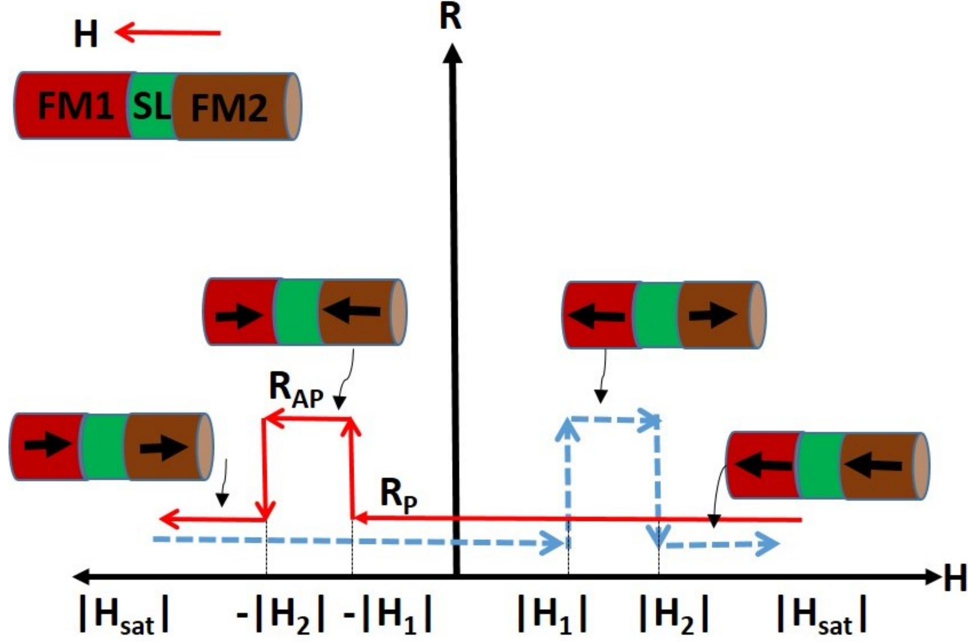

Figure 1.7. Schematic of a spin valve response. The coercivities of two ferromagnets are |H1| and |H2|. Magnetic field is swept from left to right (red line), when it reached to + $|H_1|$ then ferromagnet 1 (FM1) switched the magnetization to up direction and high Resistance state is experienced. again, when magnetic filed reached at + $|H_2|$ then ferromagnet 2 (FM2) magnetization switches to down and experience a low resistance state. Similarly when we sweep the magnetic field in negative direction we experience again high resistance state between - $|H_1|$ and - $|H_2|$.

effect transistor configuration is presented, with qualitative and quantitative analysis of carrier concentration and field effect mobility. Finally, using the established recipe for InSb NW growth, a heterostructured array comprising of Ni-InSb-Co NWs grown in polycarbonate membrane was established along with structural and electrical characterization of the heterostructure array.

This thesis is divided into seven chapters:

Chapter 2 is a review of general synthesis techniques of semiconducting NWs. This includes review of NW growth by high vacuum techniques like molecular beam epitaxy (MBE), and Metal-Organic Chemical Vapor Deposition (MOCVD). High temperature growth like

Chemical Vapor Deposition (CVD), as well as room temperature electrochemical deposition techniques will also be presented. Considering the goals of this thesis which focuses on electrochemical NW growth, this chapter will present determination of optimal deposition parameters like acidity of electrolyte solution, deposition potential, cell geometry and template type and geometry.

Chapter 3 is a discussion about template assisted growth of InSb NW in commercial anodic alumina oxide (AAO) template. These NWs were characterized via Raman and SEM and finally a back-gated field effect transistor was fabricated using the NW as the channel and the NW was found to exhibit p-type behaviour.

Chapter 4 is a presentation of our results based on the electrochemical growth of InSb NWs in polycarbonate (PC) template. These NWs were characterized via FESEM, Raman, XRD and STEM. The structure of these NWs in terms of their crystallinity as well as their defect configuration is also presented. Current-voltage characteristics of these NWs showed space charge limited current (SCLC) to be the dominant conduction mechanism in these wires.

Chapter 5 will summarize the fabrication of home-made anodic aluminum oxide (AAO) template. The need to grow AAO membranes is justified and the challenges faced during this membrane growth is also presented.

Chapter 6 focuses on growth of heterostructured NWs with composition of Ni-InSb-Co. These NWs were grown in the pores of a PC template. Initially pure Ni and Co NW arrays that were grown in PC template was characterized to study their magnetic properties. Following this, attempts were made to measure magnetoresistance (spin-valve) of Ni-InSb-Co heterostructure.Preliminary results are analyzed and conclusions drawn about the experimental results.

Chapter 7 summarizes the conclusions of the previous chapters and provides an outlook of the possibilities of using NWs grown via template assisted electrodeposition techniques.

CHAPTER 2

SYNTHESIS OF INDIUM ANTIMONIDE NANOWIRES - A REVIEW, AND STRATEGIES TO ACHIEVE ORDERED GROWTH IN TEMPLATE PORES BY ELECTRODEPOSITION

2.1. Introduction

Semiconductor NWs can be fabricated using a variety of techniques. These techniques are based on the semiconductor industry legacy of using lithography patterning and material removal methods to etch semiconductor layers into different dimensionalities like two-dimensional thin films, one-dimensional NWs and zero-dimensional quantum dots. This technique is the so-called "top-down" fabrication technique. A typical example is the patterning of photoresist lines on top of a silicon-on-insulator layer followed by the removal of excess silicon using a plasma etch tool in order to create silicon NWs. Another example is the patterning of an array of "dots" on a silicon substrate and the use of plasma etching to fabricate vertical silicon columns.

An alternate and more versatile technique is based on the direct epitaxial growth of a low-dimensional structure like a NW from a seeding substrate without using material removal techniques. In this approach, the low-dimensional structure is grown, epitaxially, layer by layer and hence this approach is called "bottom-up" growth. A classical example of this technique is the vapor–liquid–solid (VLS) growth of silicon NWs on a silicon substrate using gold eutectic droplets [20, 21].

To enable the use of NWs for different applications, it is extremely important to understand their synthesis process. As mentioned in the preceding section, the two main strategies for NW growth are: (a) bottom up approach and (b) top-down approach. These strategies, irrespective of material type can be used to growth one-dimensional NWs of any size, morphology and composition. In this chapter, the basic physics and chemistry of semiconductor NW growth will be presented along with a discussion of the fundamental challenges faced during their synthesis using either complex, expensive techniques or low-

cost, high-efficiency and bottom-up approaches.

During the growth of arsenide, phosphide or antimonide semiconductors, the biggest challenge arises from maintaining the correct ratio between the group-V and group-III precursors, called the V/III ratio. In most synthesis recipes, the V/III ratio is typically kept rather high because the group V element has a high vapour pressure. It therefore evaporates from the growing crystal without incorporating into the crystal structure, thus causing a loss in crystal stoichiometry. Irrespective of the growth strategy, the challenge is in carefully maintaining a balance of the V/III ratio.

The first part of this chapter is a brief introduction to the growth of InSb NWs using various techniques . Details of the chemical vapor deposition (CVD) will then be discussed, followed by advantages and challenges faced. Finally, in this chapter, the advantages of using electrochemical deposition for NW growth will be presented along with different approaches that were used to overcome challenges inherent in this growth technique.

2.2. High Vacuum Epitaxial Growth Techniques

Epitaxy comes from the Greek words (above and in an ordered manner). It is used to describe the growth of a crystalline material on a crystalline substrate, when there is a relationship between the two crystals. Several techniques can be used for epitaxial growth. The most common ones are: 1. Metal-Organic Chemical Vapour Deposition (MOCVD) and 2. Molecular Beam Epitaxy (MBE).

1. For MOCVD, the growth is based on metal-organic precursors which decompose on the substrate surface. The advantage of this technique is that it is more easily scalable than other epitaxy techniques, and therefore interesting for industrial applications. The drawback is the possibility of unintentional doping of the materials due to incorporation of parts of the organic precursors.

2. MBE on the other hand is based on the evaporation of pure materials that are supplied into the growth chamber from pure sources contained in Knudsen cells. It is therefore ensured that the high purity of the source is transferred to the high purity of the growing crystal. MBE chamber consists of an ultra-high vacuum chamber, which is kept at a base

pressure of 1×10^{-10} Torr by cryo-pumps and cryo-panels (liquid nitrogen circulating in the reactor walls). Ultra-high vacuum is an important requirement for MBE growth, not only to avoid unintentional incorporation of atoms, but also to ensure that atoms which are emitted from a cell can travel almost ballistically to the substrate. The sample is mounted on a manipulator, which can be heated and rotated. Low growth rates at substrate temperatures at 820^0C are reported to grow GaN and AlGaN NWs with diameters from 50 to 250 nm and lengths from 2 to 7 μm [22, 23]. Hydrogen silsesquioxane (HSQ) was used and converted to SiO_x by thermal treatment before the growth of GaAs NWs on GaAs (111)B substrate [24]. Most od the MBE NW growth parameter are growth substrate, growth time, substrate temperature, and source beam fluxes.

2.3. Chemical Vapour Deposition (CVD) Technique

This is an example of a physical vapor deposition system in which atoms, molecules or films of a chosen material are deposited onto a select substrate from the vapor phase. The impinging molecules condense from the vapors and react on the surface of a substrate. The CVD process has different approaches that are based on how the source material is vaporized to produce the vapors. Very often, the process is thermally driven, but there are CVD approaches where light or plasma-assisted methods are used. This technique is considered more versatile than many traditional methods. In CVD, the film or structure growth occurs at close to atmospheric pressure, under non-equilibrium conditions. The composition and morphology of the CVD grown structures depend on several factors including: (i) the chemical precursor, (ii) growth temperature, (iii) growth time and (iv) environment on growth substrate and in the growth chamber.

2.4. NW Growth Mechanism

As mentioned in the previous section there are different techniques that can be employed to grow NWs. Irrespective of the growth technique, most NWS grow by a mechanism called the Vapor-Liquid-Solid (VLS) growth mechanism.

The most popular, simple and versatile physical vapor deposition technique for growth

of nanostructures is achieved by thermally evaporating and sublimating a source material(s) in powder form, During this high temperature process the vapors of the sublimed material is transported into the growth zone where the vapors subsequently condense and deposit onto the substrate that is held at a certain temperature region to form desired nanostructures.

A standard CVD system is shown in Figure 2.1

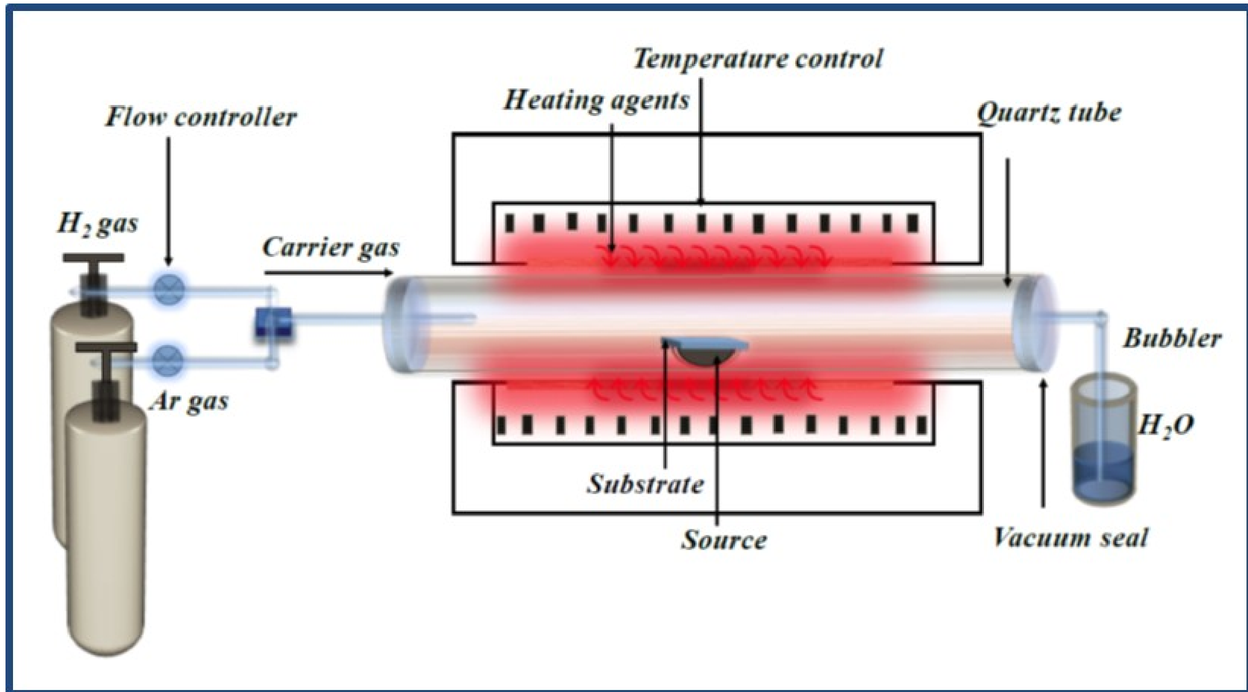

FIGURE 2.1. Schematic view of chemical vapor deposition (CVD) system for growth of InSb NWs

In a CVD system, NW growth typically occurs by supplying vapors of the desired material to a molten metal droplet. For the growth of InSb, a self-catalyzed growth process is typically used. This means that NW growth is initiated by supplying In and Sb vapors to a molten In droplet. A standard recipe used by our research group [25, 26, 27, 28] is where the Si substrate is coated with a thin film of In and subsequently placed into the growth chamber. As the temperature in the growth zone of the CVD system rises and reaches about 300 ^{0}C, the In film melts and forms droplets on the Si surface. During this period, the source that is held at a slightly higher temperature will sublime and vapors of In and Sb reach the molten In droplet. The droplet gets saturated with these vapors and as more

and more vapor condense on the molten droplet, it becomes supersaturated with In and Sb atoms. This stage of supersaturation determines the onset of NW growth. At this stage, a solid phase precipitates out of the molten droplet. The solid phase continues to grow and the NW increases in length. Its diameter is determined by the growth kinematics and also by the size of the molten droplet. NW growth continues as long as the source and substrate temperature are maintained and vapors of In and Sb are supplied to the growth region.

The biggest challenge in the growth of NWs by CVD using the VLS growth mechanism is the difference in vapor pressure of In and Sb. Since Sb has a high vapor pressure, it re-evaporates from the growing crystal. Hence, it is important to maintain a high Sb vapor pressure in the growth chamber.

Another challenge arises from the fact that CVD growth of NWs occurs at close to atmospheric pressure. Due to this, any trace of oxygen in the growth chamber results in the formation of In and/or Sb oxides. It is therefore critical that all traces of oxygen be eliminated from the growth region. A previous work, in reference [25], showed that any variation in the growth temperature can result in NWs that are metallic, semiconducting or semi-metallic. As seen in Figure 2.2, NWs grown at 400^0C are semi-metals of Sb. A slight increase of temperature to 450^0C results in growth of semiconducting (InSb) NWs. Further increase to about 600^0C results in growth of metallic (In) NWs. All temperature dependent stoichiometry of InSb NWs grown at different temperatures are shown in Figure 2.2.

On account of these challenges, high-temperature growth of compound III-V semiconductors like InSb by CVD is not viable for mass-production of these NWs. An alternate to this is growth of InSb NWs by electrochemical technique - the objective of this thesis.

2.5. Growth of NWs Using Electrochemical Deposition Technique

There electrode cell configuration was used to grow the NWs (InSb, Co, and Ni). In this thesis two different kind of template were used. First, commercial free standing anodic aluminum oxide (AAO) wafers purchased from Synkera technologies. Inc.(now became InRedox). Average AAO template pore diameter were 100 ± 10 nm and pore length of 50 ± 1 μm. Second, ion-track etched polycarbonate (PC) templates were purchased from GE

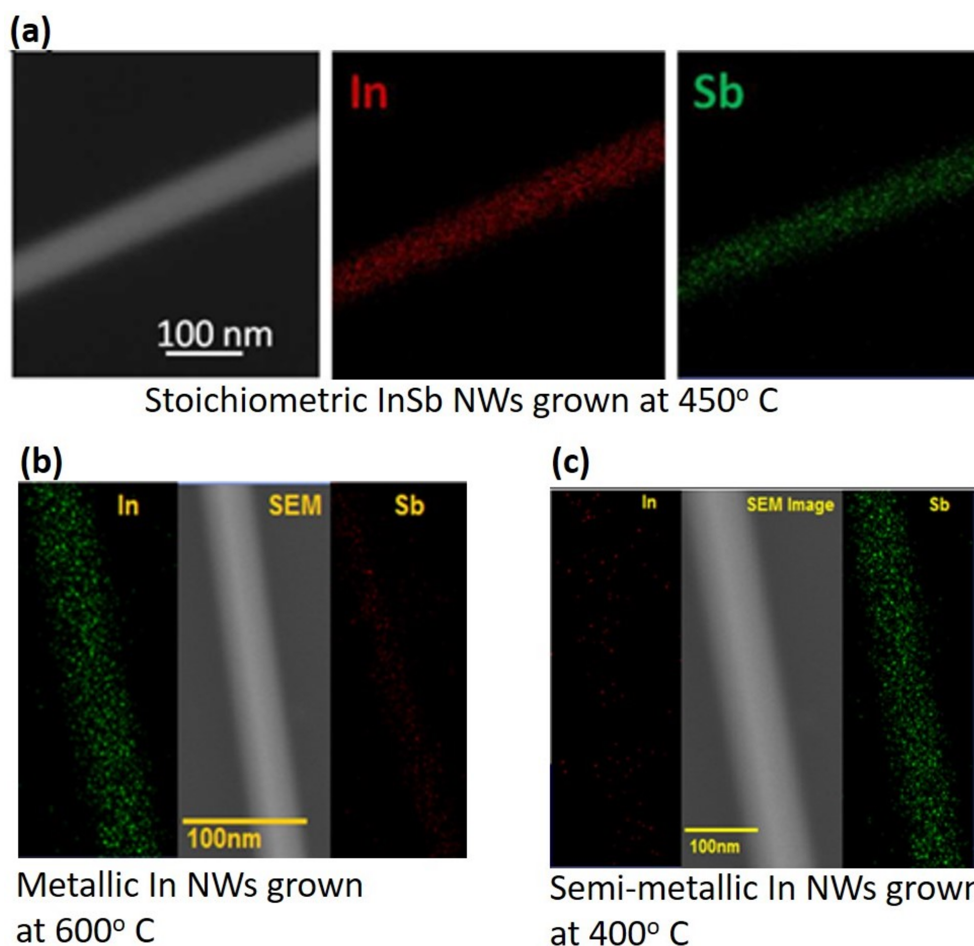

FIGURE 2.2. Schematic view of (a) electrochemical deposition setup for NWs growth, and (b) the cross-sectional view of NWs grown in anodic aluminum oxide (AAO) template.

and their pore diameter were $\sim$ 150–200 nm and pore length of 20 μm.

Since both (AAO and PC) templates are free standing (pores are open both sides), its is necessary to cover one side with metal (Au) film so that metal film side can work as a working electrode. Thermal evaporation is used for Au thin film deposition on both of templates (AAO and PC). Since AAO templates are rigid and fragile, it is not suitable for attachment in a sample holder. So, the AAO template was coated on one side with Au thin film, which was then attached to sticky conducting copper tape (which works as a working electrode). For counter electrode, platinum (Pt) mesh was used. Solution of silver Chloride (Ag/AgCl) was used in reference electrode with semipermeable membrane at the bottom of

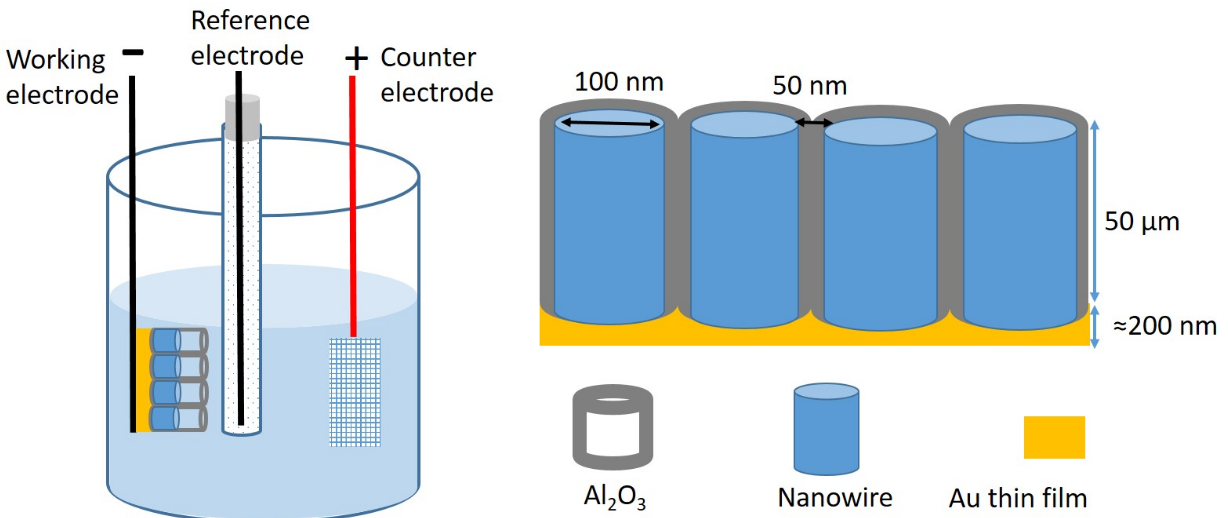

FIGURE 2.3. Schematic view of (a) electrochemical deposition setup for NWs growth, and (b) the cross-sectional view of NWs grown in anodic aluminum oxide (AAO) template.

the electrode. For InSb NW growth, indium chloride ($InCl_2$), antimony chloride ($SbCl_3$) , citric acid, and potassium citrate/or sodium citrate were used with specific concentrations as an electrolyte. Detail of InSb NW growth in AAO template via electrochemical deposition is presented in Chapter 3. Growth of InSb NW in PC template is presented in detail in Chapter 4. Irrespective of flexible (PC) and hard (AAO) template, growth mechanism is almost similar as described in next subsection.

2.5.1. Electrochemical Growth Mechanism: Convection, Migration, and Diffusion

The benchmark method for synthesis of NW was suggested in 1986 by Martin et al. [29], where NWs were grown inside polycarbonate membranes. This method has since been widely used to synthesize NWs in both polycarbonate and anodic aluminum oxide (AAO) membranes. These membranes contain a high density of cylindrical pores that are perpendicular to the membrane surface and in most cases, these pores penetrate the entire membrane thickness. There have been several studies on electrochemical growth of NWs but very small number of investigations on understanding the growth mechanism of NWs in AAO pores.

Template-assisted NW growth process consists of two major steps: electrochemical reduction of the cation inside the pore, followed by removal of the template. Several studies [30, 31] have shown that during the pore-filling stage (NW growth), the total constant current density is independent of flux variation inside the pore and concentration of electrolyte at the mouth of pore during electrodeposition. Recently, another study [32] showed that the electrolyte concentration at the mouth of the pore remains constant and current decays with time; a fact that contradicts the previous study where current remains constant. Here, we discuss the more realistic model that describes a situation where the electrolyte concentration at the mouth of the pores is different than the bulk during electrodeposition.

The electrodeposition growth process of NWs in porous templates has been modeled by considering different mechanisms of mass transport at different stages of the growth process [33]. There are mainly three different mechanisms that could explain the growth process: (i) diffusion process (arising from concentration gradients existing between electrolyte in the template pores and in the solution), (ii) convection process (arising from movement of deposition ions in the electrolyte), and (iii) migration of ions into the template pores. Contribution of each process can be controlled by modifying the cell design, reducing depositing ion concentrations compared to mixing electrolyte, and stirring the electrolyte during growth process to avoid the concentration gradient.

2.5.2. Diffusion Mechanism in NW Growth Process

Mass transport of ions during NW growth is mainly controlled by a diffusion process. The three main stages of this process are shown in Figure 2.4. Figure 2.4(a) shows the earlier stage of diffusion where diffusion front propagates in only one dimension inside the pores. Figure 2.4(b) shows the second stage where diffusion front reached the mouth of the pore and opens in three-dimensional hemispherical front. As soon as diffusion front reaches at the mouth, then there is a concentration gradient builds up between the mouth and the bulk. Figure 2.4(c) shows the third stage where linear diffusion happens inside and outside of the pores. This diffusion-limited electrodeposition results in a morphological instability driven by individual NWs [34]. In template-assisted electrodeposition, NW length must follow the

length of AAO pore, but some NW grows fast compared to others and ends up mushroom-like structures at the top surface of AAO template [35, 36, 37, 38, 39, 40]. Recent study [34] also showed that this growth instability can be avoided by introducing temperature gradient between bottom and top of the AAO pores. The diffusion mechanism during various stages of NW growth is described by the S-curve of current-time plot, as shown in Figure 2.4(a).

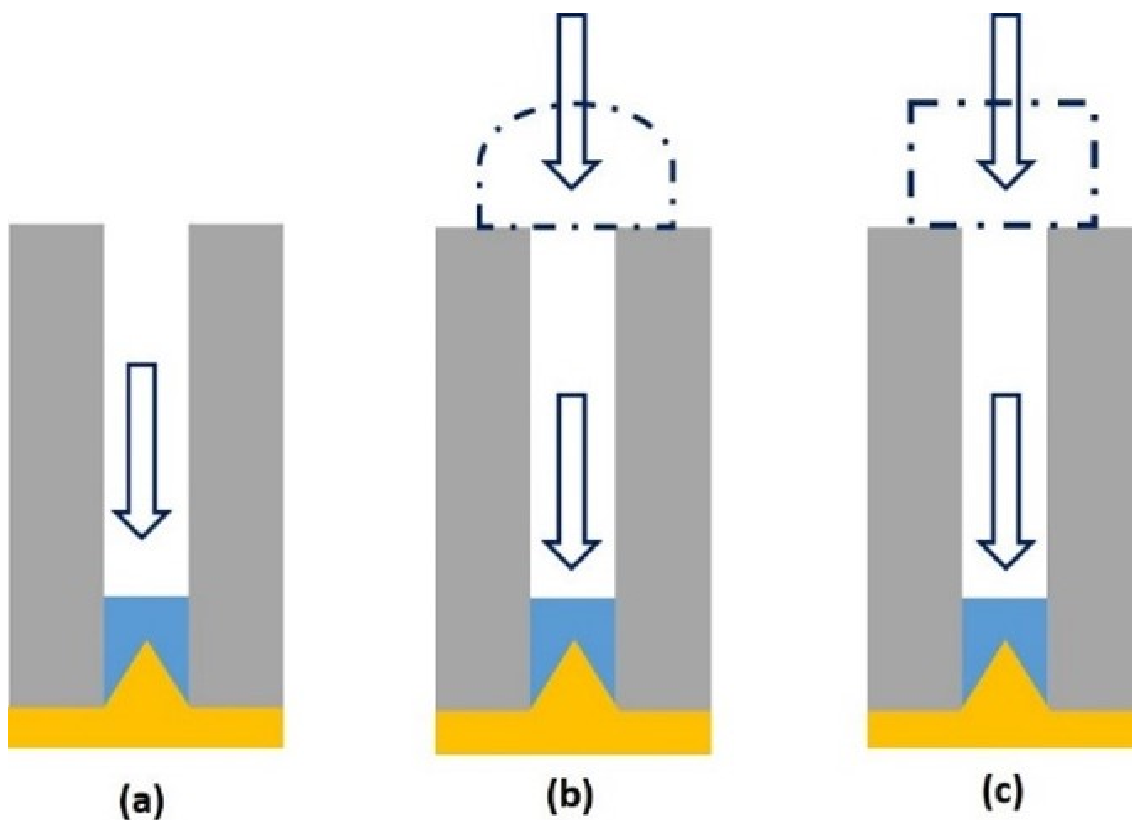

FIGURE 2.4. Schematic of growth of NW in a single nanopore: (a) linear diffusion, (b) linear and semi-infinite hemispherical diffusion, and (c) semi-infinite planar diffusion outside the pore [3].

The entire mechanism involves three consecutive growth stages: (i) one dimensional diffusion front inside AAO pores; (ii) linear diffusion inside the pores and hemispherical diffusion at the mouth of the pores; and (iii) merging of hemispherical diffusion front and resulting in planned front over the surface of the mouth. The electrodeposition time and average length of wire have been controlled by monitoring the deposition current versus time at given deposition voltage -1.5 V which was maintained with respect to reference electrode.

Inset of Figure 4(a) shows the schematic of the various stages of electrodeposition.

In first stage of growth process, concentration of the electrolyte at the mouth of pores matches the concentration of the bulk of the electrolyte (c^b). The linear diffusion front passing through pore length results in transportation of In and Sb ions inside the pores of the AAO template. The diffusion fronts between individual pores have not been overlapped at this stage. The concentration within the pore changes as NW growth starts and it has been expressed by Fick's law as: $c(x,t) = c^b erf\left[\frac{x}{2\sqrt{Dt}}\right]$, where $2\sqrt{Dt}$ is the diffusion length (L) that corresponds how far concentration varies along the pore length at time t. The initial pore length is L0 at t = 0. There is a sharp decrease in electrodeposition current during this time, as is expected for diffusion-controlled process. The current was observed to decrease from 35 to 20 mA in region (I) of the plot in Figure 2(a) which corresponds to region (i) of growth process. In region (i), In and Sb ions diffuse to the bottom of the pore in the tubular column of AAO template to initiate NW growth.

During region (II) of the growth process, initial linear diffusion front reaches the mouth of the pores and three dimensional hemispherical diffusion front develops at the mouth. During this stage in region (II) of plot Figure 4, the steady increase in current has been observed and is believed to increase the diffusion of ions to the NW growth front. During the final stage in region (III), the NWs have filled the pore completely and the hemispherical cap merges with each other and formed a continuous rough film on the surface of template. In the region (III) of the S-curve plot, current does not increase significantly and tends to saturate, as compared to region (II) of the plot. Figure 2(b) and (c) shows cross-sectional SEM images of template in the region (I) and (III), respectively. Figure 2(b) shows partially filled pores, which correspond to a linear diffusion in region (I) of the S-curve. Figure 4(c) shows the completely filled pores and hemispherical caps that merge to form a dense mushroom-like overgrowth on the surface of the pores.

2.5.3. Convection Mechanism in Growth of NWs

The effect of convection on NW growth process is dependent on cell design. The three electrodes in an electrochemical cell are: (i) working electrode (substrate); (ii) counter

electrode (Pt wire/mesh); and (iii) reference electrode.

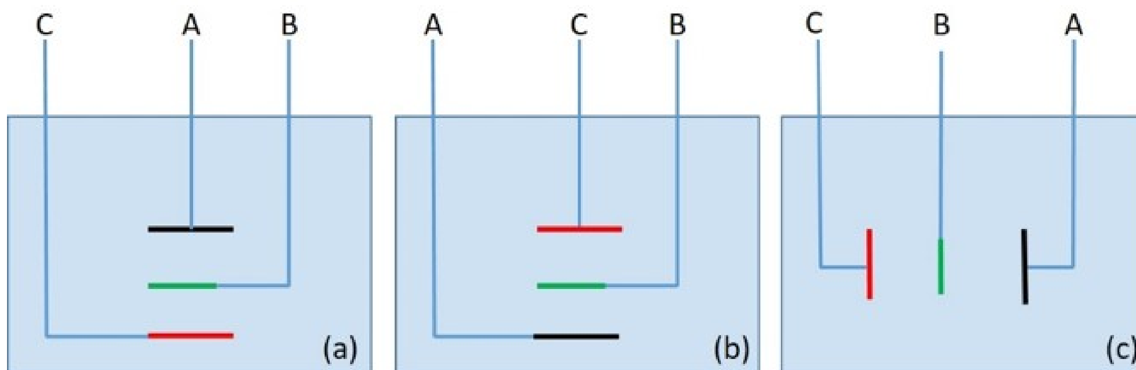

FIGURE 2.5. Schematic of cell designs: (a) cathode over anode; (b) anode over cathode; and (c) cathode and electrode placed laterally and parallel to each other. Letter A represents working electrode (Cathode), C represents secondary electrode (Anode), and B represents reference electrode [3].

To minimize the mechanism of natural convection, electrodeposition cell configuration is an integral part of NW growth in nanoporous templates. In Figure 3(a) and (b), the cathode and anode are placed vertically above each other, whereas in Figure 3(c), the cathode and anode are placed parallel to each other.

The effects of convection are considered to be minimal for the design in Figure 3(c). Konishi et al. [41] reported that the electrodeposition current increases in the case of anode over cathode Figure 3(b) configuration, and current decreases in the case of cathode over anode configuration Figure 3(a) during early stages of the electrodeposition. They have found the considerable difference in the transient behavior of the current in 100- and 200-nm-sized pores in certain stage of electrodeposition, which is caused by the electrolytic cell configuration.

Figure 2.6 shows the optical image of three electrode electrochemical cell which was used for some of the experiments. Figure 2.6(a) shows the vertical configuration where migration and convection of ions are favorable, which can be avoided with the Figure 2.6(b) configuration.

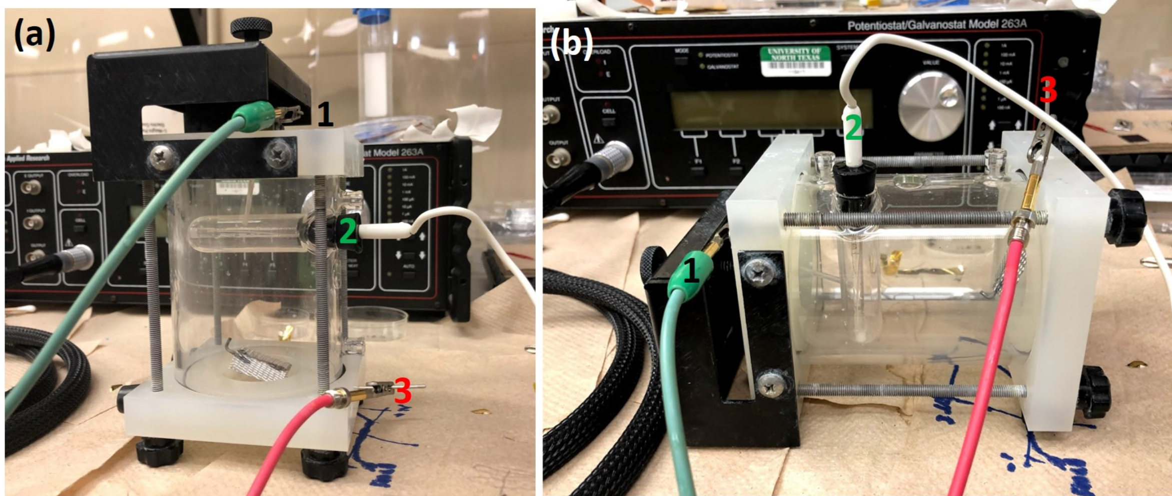

FIGURE 2.6. Optical images of electrochemical cell with 3 electrode (a) represents one of two vertical configurations of electrodes presented in Figure 2.5 (a) Figure 2.5 (b), in this case anode is over cathode representing figure 2.5 (b), However, (b) represent the horizontal electrode configuration where cathode and anode are placed horizontally and parallel to each, which avoids the convection and migration of ions into the pores of template. Symbol "1" in black color represents the working electrode, symbol "2" in green color represents the the reference electrode, and symbol "3" in red color represents the counter electrode.

2.5.4. Migration of Ions During Growth of NWs

The effects of natural convection are proven to be significant and reported in Reference [42] for the schematic shown in Figure 4, where an increase in convection current because of this mechanism is shown for pores size as small as 100 nm. This effect was observed during Cu electrodeposition.

To explain the InSb NW growth process in the following section, the effect of migration of In and Sb ions has not been considered in this discussion. Since concentration of these ions in supporting electrolyte is low, the contribution of ion migration is considered to be lower than diffusion.

To conclude the discussion on mechanisms affecting NW growth in template pores, we

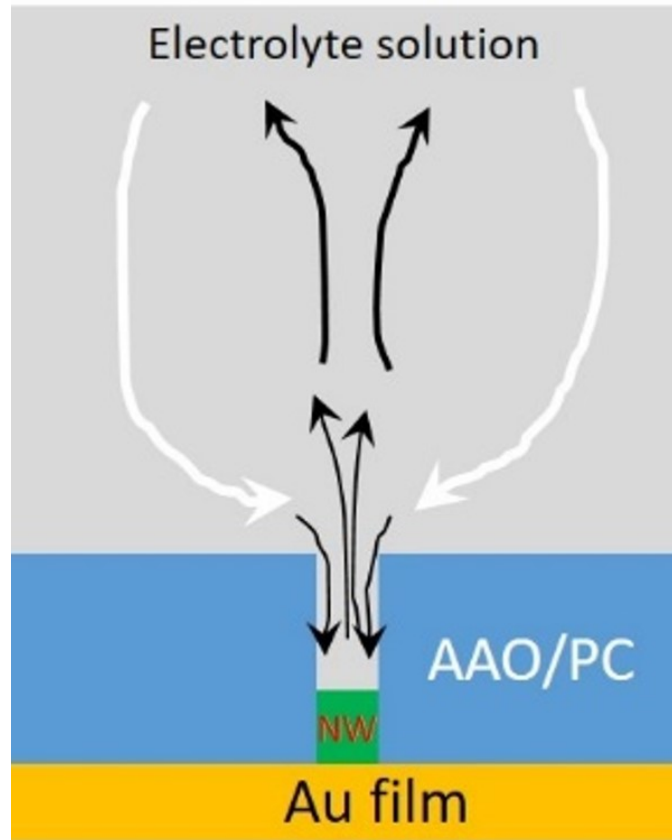

FIGURE 2.7. Schematic diagram convection in and around nanoporous pores in the configuration of anode over cathode. [3]

can say that there are various parameters that affect the NW growth such as cell design, pH of electrolyte, applied bias as well as various growth mechanisms like convection, migration and diffusion. However, of these, diffusion-controlled mass transfer flux is more important. Influence of migration can be ignored by lowering the concentration of depositing metal and increasing the concentration of supporting electrolyte. The contribution due to natural convection can be avoided by electrodeposition cell design in which working electrode can be placed in up or vertical positions.

In this thesis, only linear difusion dominated growth of NWs is considered as shown in Figure 2.5(c), and Figure 2.6(b). We have used two different kinf of template to grown InSb NWs (a) flexible ion-track-etched polycorbonate template with average pore diamter of 175 nm (ranging from 150 to 200 nm) and pore length 20 μm, and (b) commercial anodic

alumium oxide (AAO) template with pore diameter 100 nm and pore legth of 50 μm as shown in Figure 2.8

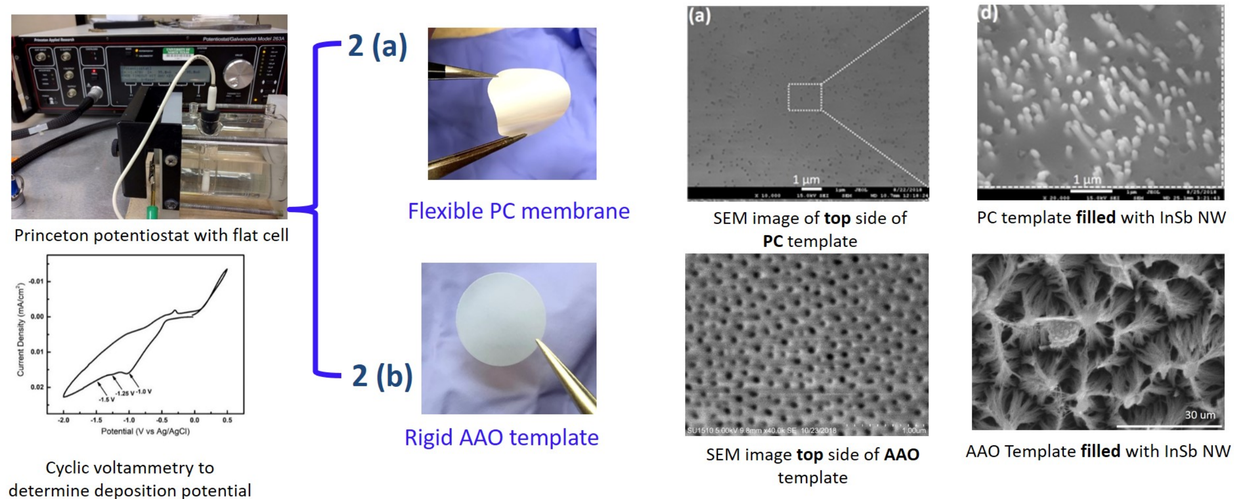

FIGURE 2.8. Optical image of electrodeposition setup, (a) shows the flexible PCtemplate and SEM image of template and after NW growth and partial eching to see the NWs, (b) circilar rigid AAO template, and SEM images with blank and after NWs growth and etching where NWs are bundled.

CHAPTER 3

TEMPLATE-ASSISTED GROWTH OF INDIUM ANIMONIDE NANOWIRES IN COMMERCIAL ANODIC ALUMINUM OXIDE TEMPLATE[1]

This chapter based on published results (indicated in footnote) is a report on the growth of Sb-rich indium antimonide (InSb) NWs fabricated by dc electrodeposition in the pores of a gold-coated nanoporous anodic alumina oxide (AAO) template. An explanation of the various mechanisms of mass transport during successive stages of the growth process is also presented with experimental results confirming different growth stages. The 100 nm thick InSb NWs that were grown using an electrolyte of pH 1.7 were found to be rich in antimony (Sb). The electrical properties of a single InSb NW was investigated by connecting the NW in a field-effect-transistor type configuration. The NWs showed p-type conduction with a hole concentration of $\sim 1.9{\times}10^{16}$ cm^{-3} and field effect hole mobility of ~ 507 cm$^2V^{-1}s^{-1}$. The device had a high on-off current ratio of the order of 10^3. Temperature-dependent transport measurements showed thermally activated Arrhenius conduction in the temperature range from 200–325 K, yielding an activation energy of 0.1 eV. The ability to obtain high density of p-type InSb NWs without addition of any dopants opens up new opportunities for using these NWs in fabrication of electronic devices.

3.1. Introduction

In recent years, there has been increasing interest in nanostructured III–V semiconducting materials due to their potential applications in electronic and optoelectronic devices [43]. Of these, indium antimonide (InSb) with a direct band gap of 0.17 eV at 300 K is extremely promising since it has high electron and hole mobility [44, 45] of 77000 $cm^2V^{-1}s^{-1}$, and 850 $cm^2V^{-1}s^{-1}$ respectively. With a small electron effective mass of 0.014,[44, 46] and large Lande g-factor of 51[46, 47], InSb is a material of choice for use in high-speed electronic devices, low-power logic transistors,[48, 49] NW field effect transistors (FETs),[50, 51, 52]

[1]This chapter has been reproduced as is from the publication "Template-Assisted Electrochemical Synthesis of p-Type InSb NWs", ECS Journal of Solid State Science and Technology, Volume 6, Number 5, Pages N39-N43, Published 6 April 2017 , with permission from ECS.

infrared (IR) nano-optoelectronics,[53, 54, 55] thermoelectrics,[56, 57, 58, 59, 60] and magnetoresistive sensors[61]. Among various techniques such as chemical vapor deposition (CVD)[62] and molecular beam epitaxy (MBE)[63] used to synthesize NWs, electrodeposition in nanoporous anodic alumina oxide (AAO) template is a relatively inexpensive and versatile method that can be performed at room temperature. This low-temperature growth technique is preferred for growth of compound semiconductors like InSb where the difference in vapor pressures between In and Sb can result in non-stoichiometric growth at high temperatures. The technique is especially desirable for growing heterostructures since it prevents heat-induced inter-diffusion of elements across adjacent layers in the heterostructure. Another advantage is the possibility that the NW can be doped during the electrodeposition process, thus making it the method of choice for synthesis of nanostructured materials at low cost.

In recent years, electrochemical growth of NWs in AAO templates has received much attention. AAO is a self-organized nanostructured material containing a high density of uniform cylindrical pores that are aligned perpendicular to the surface and penetrates the entire thickness of the template [64, 65, 66, 67]. AAO is also optically transparent, electrically insulating, thermally and mechanically robust and chemically inert[68, 69, 70]. NW arrays grown in template pores can be used for a wide range of applications such as energy[71, 72, 73] and electronic[74, 75, 76] devices that requires density, scalability, reproducibility and cost effectiveness[70]. In this regards, template-assisted electrodeposition offers distinct advantages[64, 66] since it is readily scalable to mass production.

There are works on InSb growth in AAO template pores. InSb that is not intentionally doped typically show n-type behavior since their electron-rich surface layer pins its Fermi level in the conduction band. To develop this material for CMOS applications it is required to have both n and p-type InSb. Doping InSb with carbon has been shown to result in p-type transport [77], but the addition of carbon was found to result in mobility reduction. This is one of the major contribution of this work where p-type doping of InSb was achieved without the addition of any dopant resulting in a higher value of field effect hole mobility.

There are also several challenges that affect the growth of uniform InSb NWs in the template pores. These challenges have resulted in a number of theoretical papers modeling the growth process of NWs in porous membranes [78, 79]. Experimental evidence validating the model has also been presented [70, 80]. In this paper, we present our results and discuss the growth mechanism, highlighting the challenges of template assisted growth.

InSb NW arrays have important technological applications and there are works where the aspect ratio of the NWs size (diameter/length), shape and periodicity have been engineered for applications in NW-based photovoltaics and photodetectors[81, 82, 83]. An important characteristic of template grown InSb NWs is their surface roughness, which makes them attractive for thermoelectric applications.

3.2. Experimental Method

The NWs were grown in a commercial self-organized porous anodic aluminum oxide (AAO) template purchased from Synkera Technologies, Inc, with pore length and diameter of $\sim 50\ \mu m$ and $\sim 100\ nm$ respectively. The template pores were first widened by soaking the template in 5% phosphoric acid (H_3PO_4) for 5 min at $30^\circ\ C$. This also resulted in removal of any unintentional oxide at the barrier end of the template. It most likely also resulted in moderate pore wetting. One side of the AAO template was then coated with a thin gold (Au) film (150 nm) using thermal evaporation (HHV Technologies, Linde: Auto 306). The template was subjected to pore wetting and de-aeration by placing it in an ultrasonic bath with DI water for 2-3 minutes.

The electrodeposition process was conducted in a three electrode cell with the Au side of the AAO template functioning as the working electrode, platinum wire as the counter electrode and Ag/AgCl as the reference electrode. The experiment was done under potentiostatic conditions, where a constant potential of -1.5 V is maintained between the Au at the bottom of the pores (working electrode) and the reference electrode (Ag/AgCl) immersed in the electrolyte and placed fairly close (about 1 cm) to the working electrode. The Au-plated side of AAO template was then attached to a conducting copper tape and an insulating polymer was applied to the template edges in order to avoid any conducting path for the

electrolyte, except through the open AAO pores which terminate at Au thin film at the bottom of the pores. The entire electrodeposition process was controlled and carried out using a Princeton potentiostat (Potentiostat/Galvanostat 263A). The electrolyte used in this experiment was: 0.15 M $InCl_3$, 0.1 M $SbCl_3$, 0.36 M $C_6H_8O_7H_2O$, and $C_6H_5Na_3O_7$ [43], and its pH value was adjusted to 1.7. During this room-temperature electrodeposition process, the citrate ions were used as complexing agents to bring the deposition potential of In and Sb closer to maintain a binary growth of InSb NWs[43, 84, 85]. On completion of the deposition process the AAO template was carefully removed from the electrodeposition cell, rinsed several times with DI water, and removed from copper tape for further processing by soaking in acetone for removal of the protective polymer. The NWs were then extracted by dissolving the AAO template in 1 M KOH. To remove all traces of KOH, the NWs were cleaned with DI water and the solution centrifuged (Fisher Scientific Centrifuge 228 Benchtop Centrifuge) at 3000 rpm, resulting in the NWs being present as a residue at the bottom of the centrifuge vial. The NWs were subsequently dispersed on a clean silicon (Si) substrate and its surface morphology and composition was studied using scanning electron microscopy equipped with energy dispersive X-ray (EDX) spectroscopy (SEM, Hitachi SU 1510).

The InSb NWs were also characterized by Raman Spectroscopy at ambient temperature using a Nicolet Almega XR–Raman spectrometer with a 532 nm green laser. For electrical measurements, the NWs were dispersed on a n^+ Si substrate (resistivity of 0.001–0.005 Ωcm) covered with a 250 nm thick SiO_2 layer. Two metal (Cr/Au) contacts were established at the NW ends to function as the source and drain electrodes. To facilitate three terminal measurements, the NWs were used in a field-effect transistor type configuration, with the highly doped n^+ Si substrate serving as the back gate. The contacted NW was placed in a temperature controlled cryostat (Lakeshore 330), and carrier transport measurements were made using a semiconductor parametric analyzer (Agilent Technologies B1500A). This also allowed for temperature dependent conductivity measurements in the temperature range from 100 to 450 K.

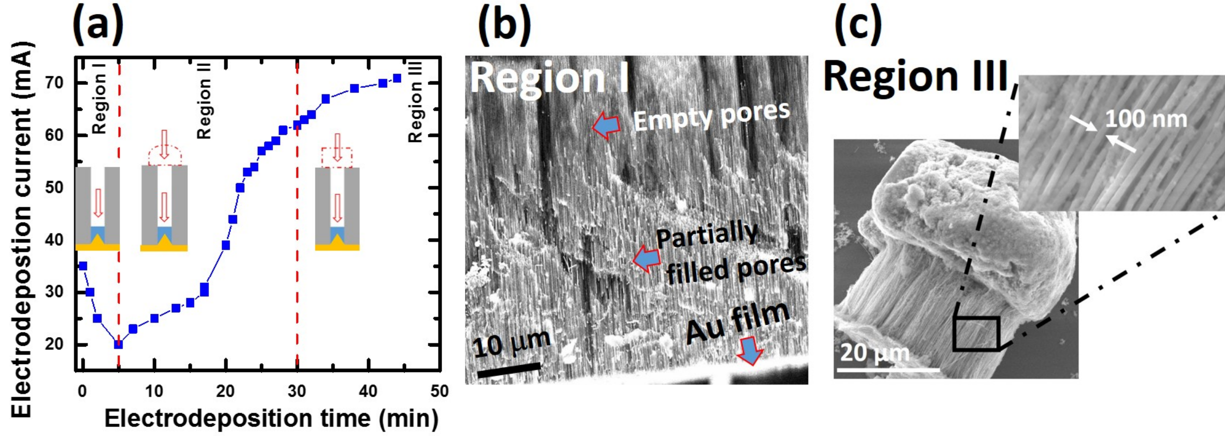

FIGURE 3.1. Evolution of NW growth in the AAO template pores: (a) Current-time plot of InSb NW growth showing different growth regions; (b) Cross-sectional SEM image of the template in region I. The thin bottom layer is a gold film. The pores are partially filled with InSb. This region corresponds to planar diffusion inside the pore; (c) Cross-sectional SEM image of region III where NWs have filled the pores and the dome shaped tips collapse to form mushroom shaped clusters, corresponding to semi-infinite planar diffusion at the mouth of the pore.

3.3. Result and Discussions

In references [78, 79], the authors have modeled the electrodeposition NW growth in porous membranes by considering the various mechanisms of mass transport during different stages of the growth process. The overall growth process includes the mechanism of diffusion (arising from a concentration gradient), convection (arising from movement of ions in the electrolyte) and migration of ions into template pores. The contribution of each of these mechanisms to the overall growth can be controlled by modifying cell design, varying concentration of electrolyte and by introducing other experimental variables like solution stirring and maintaining a temperature gradient across the pore length[70] during the growth process. The effects of migration of In and Sb ions during the electrodeposition process is not considered in this discussion. Due to the relatively low concentration of these ions in the supporting electrolyte, we consider their contribution to the growth process to be sig-

nificantly lower than that due to diffusion. Similarly, the effect of convection is also most likely minimal. In the works by Blanco et al.[78], and Konishi et al.[86], the dependence of convection on the cell design has been studied and it was shown that the effect of natural convection at the short time periods required for growth is minimized when the working electrode points down and the NWs grow downwards towards the gravitational field. This design favored larger electrodeposition currents compared to the design in which the working electrode is below the counter electrode. In the cell design used in our experiment, the working electrode (anode) and the counter electrode (cathode) are placed adjacent to each other, with the reference electrode placed in between the two. We therefore base the analysis of our time dependent current response during the growth process on the assumption that the InSb NW growth was governed mainly by the process of diffusion.

The correlation between the S-curve of the current-time plot [Fig.3.1(a)] and the various stages of the NW growth process is best described by three successive growth stages: (i) one-dimensional diffusion front inside the pores, (ii) linear diffusion front inside the pores and hemispherical diffusion front at the mouth of the pores, (iii) coalescing of the hemispherical fronts resulting in a planar front over the pore surface. The electrodeposition time and consequently the average length of the InSb NWs was controlled by monitoring the deposition current (I) vs. deposition time (t) for the given deposition voltage of -1.5 V maintained at the alumina template with respect to the reference electrode. The inset of the current-time plot [Fig.3.1(a)] shows the corresponding schematic of the growth stage.

During the initial stage of the growth process, the concentration of the electrolyte at the mouth of the pores matches the concentration in the bulk of the electrolyte (c^b). The one-dimensional diffusion front passing along the pore length results in transport of In and Sb ions inside the pores of the template. At this stage, the diffusion fronts between individual pores do not overlap. The concentration within the pore changes as growth commences and is expressed by Fick's law as: $c(x,t) = c^b erf[\frac{x}{2\sqrt{Dt}}]$, where $2\sqrt{Dt}$ is the diffusion length (L) that characterizes how far the concentration varies along the length of the pore in time t. At time t = 0, $L = L_o$, which is the initial pore length. As time increases, L decreases as

small sections of the pores get filled. During this time of the growth process there is a sharp decrease in the electrodeposition current, as is expected for diffusion-controlled processes. The decrease in current from 35 mA to about 20 mA in Region (I) of the plot [Fig.3.1(a)] corresponds to stage (i) of the growth process, during which the In and Sb ions diffuse to the bottom of the narrow pore in the tubular columns of the AAO template to initiate NW growth.

During the second stage of the growth process, the initial linear diffusion front reaches the mouth of the pores and a three-dimensional hemispherical diffusion front develops at the mouth. The hemispheres do not coalesce with each other and at this stage the material flux into each pore is determined by the ratio of the flux inside and outside the pore. During this stage, shown in Region (II) of the plot [Fig.3.1], the steady increase in current with the growth of the NWs is believed to be due to an increased diffusion of ions to the NW growth front. During the final stage of the growth, the NWs fill the pores completely and the hemispherical caps coalesce with each other and forms a continuous rough film on the template surface. As can be seen in region III of the graph, the current does not vary much with time during the stage of pore filling. Fig.3.1(b) and (c) shows SEM image of the template corresponding to region I and III of the growth process as described by the current-time plot of Fig.3.1(a). Fig.3.1(b), is a cross-section SEM image of the alumina template with a thin Au film coating one side of it. The image also shows partially filled tubes, corresponding to linear diffusion within the pores (stage 1 of the growth process). Fig.3.1(c) is an SEM image showing the completely filled pores and the hemispherical caps that have coalesced to form a dense overgrowth on the surface.

Following growth, the crusty surface layer was removed from the surface by mechanical polishing. The template was subsequently dissolved in KOH. The average length and diameter of the InSb NWs after processing was about 20–30 μm and 100 nm respectively [Fig.3.2(a)]. The NWs were found to have a rough jagged surface, attributed to roughness of the template tube walls. This is clearly visible in the SEM image of a single InSb NW shown in the inset of Fig.3.2(a). EDX spectrum [Fig.3.2(b)] obtained along the NW length

showed the NWs to be rich in Sb with an average In:Sb weight ratio of 40:60.

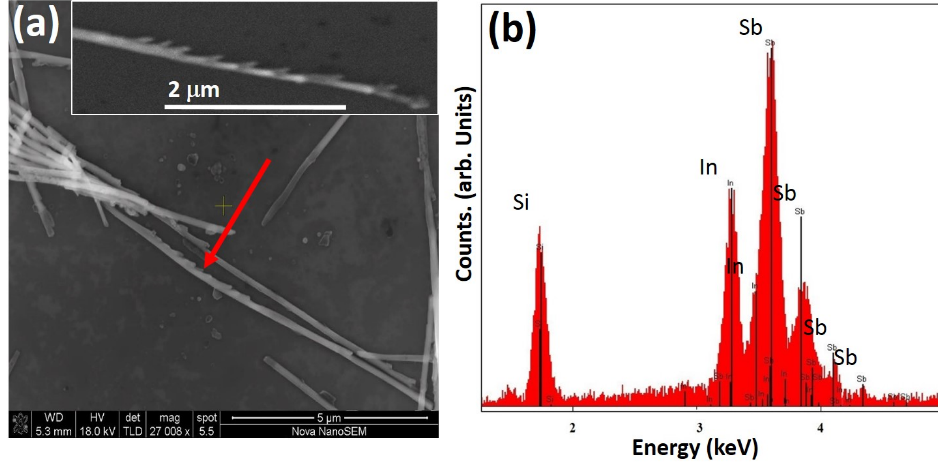

FIGURE 3.2. SEM images of (a) InSb NWs that were removed from the AAO template and dispersed on a cleaned Si substrate. Inset shows a single NW with roughened surface; (b) EDX spectrum of Sb-rich InSb NWs.

Fig.3.3 shows the Raman spectrum obtained from two crossed InSb NWs that were placed on a Si substrate (optical image shown in inset of Fig.3.3). Room temperature Raman spectrum reveals distinct peaks of TO and LO phonon modes at 178 cm^{-1} and 188 cm^{-1} respectively, which matches closely with the TO and LO peaks of prior studies on InSb NWs [43, 87, 88, 89, 90]. The observation of these two distinct peaks for the TO and LO modes of phonon vibration is indicative of the high quality of InSb NWs. However, in comparison with bulk InSb, there are a number of important differences in the Raman spectra of InSb NWs. Though the phonon peaks in bulk InSb are symmetric, they are asymmetric in the NWs and are shifted in comparison to the bulk values. More importantly, the peaks at about 150 cm^{-1} and 108 cm^{-1} are not reported in bulk InSb, but they are prominent in our InSb NWs and has been reported by other works[91]. The additional peaks (TO-TA and 2TA) can be attributed to surface roughness and defects in the NW [92]. There is also the possibility that in NWs, phonons away from the Brillouin zone could participate in the scattering process due to relaxation of the q = 0 Raman scattering rule, resulting in asymmetric broadening and downshifting of the Raman peaks. Additional peaks at 150 cm^{-1} and 110 cm^{-1} were

reported earlier in InSb nanorods by Wada et al. [92]; assigned to TO-TA and 2TA phonon modes, respectively.

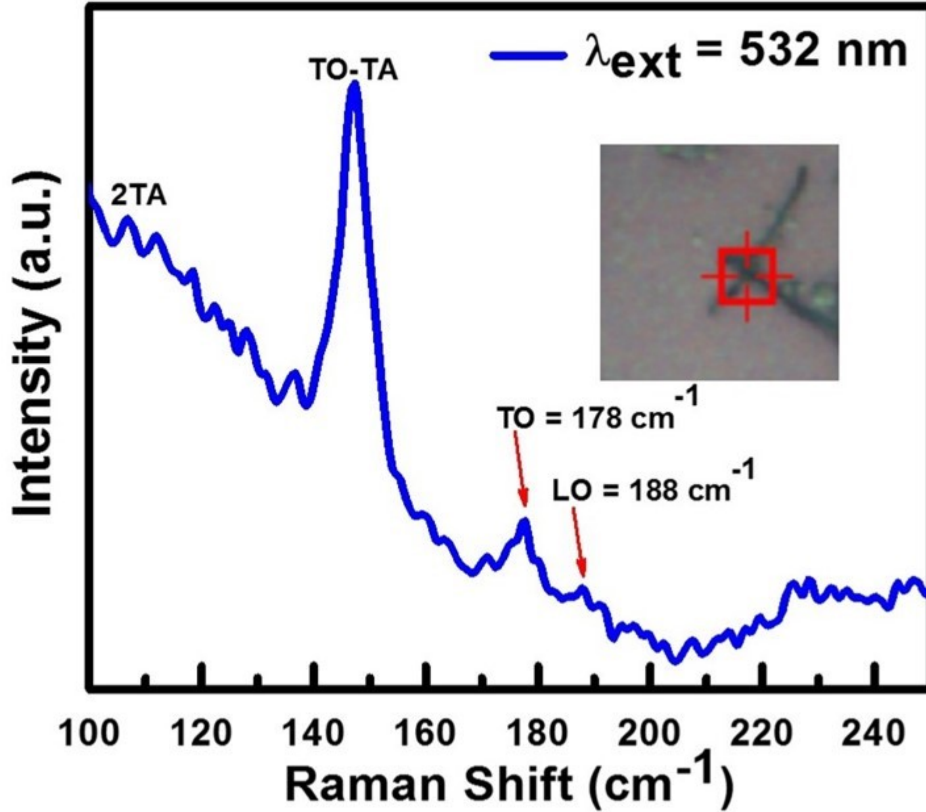

FIGURE 3.3. Raman spectrum obtained from two crossed InSb NWs; inset shows the region from where the Raman spectrum was collected. The two peaks at 150 and 110 cm^{-1} are most likely related to surface roughness and defects in the NW. The characteristic TO, LO peaks attest to crystallinity of the InSb NWs.

To determine the type, concentration, and mobility of carriers in the Sb-rich InSb NWs, current-voltage measurements (2-terminal and 3-terminal) were made on the fabricated device. The device schematic and SEM image of a single InSb NW that is contacted by Cr/Au electrodes on both ends is shown in Fig.3.4. The results of electron transport measurements made on the back-gated NW at different V_{ds} (varying from from 0.2 V to 1.0 V in steps of 0.2 V) are shown in Fig.3.5. The transfer curves at V_{ds} = 1.0 V, both on linear and on log scale (inset) shows a sub-threshold region between -0.5V and +0.5V. This value most likely

corresponds to complete depletion of the NW. As seen in Fig.3.5, the InSb NW conductance was found to decrease with increasing V_{gs}, indicative of a p-channel FET behavior.

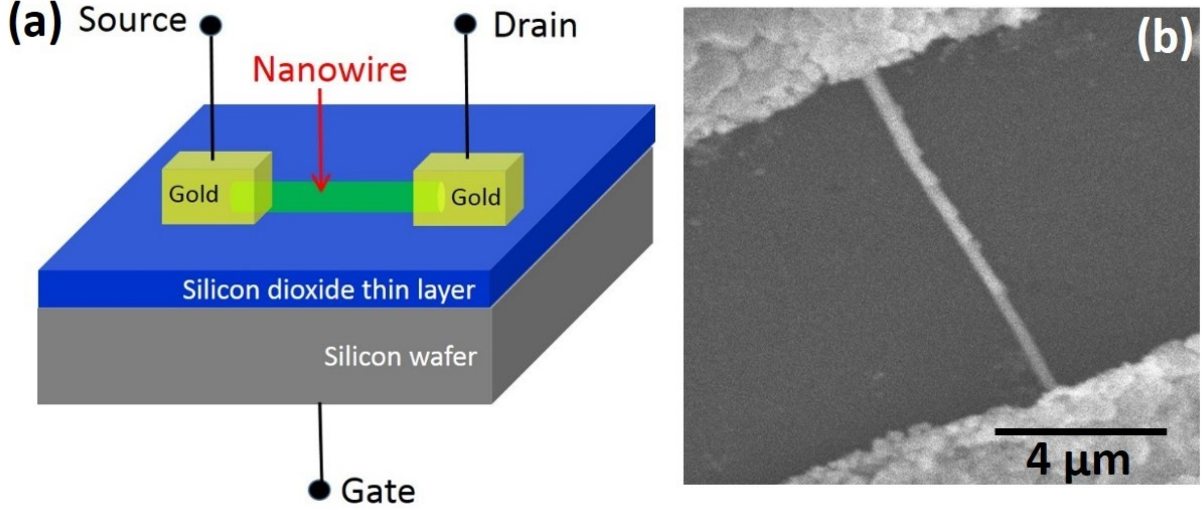

FIGURE 3.4. (a) Schematic of back-gated InSb NW field effect transistor, (b) SEM image of a single InSb NW contacted by two Cr/Au contacts.

The equilibrium hole concentration p_0 in the NW was found using the equation 18 [93, 94]:

$$p_0 = \frac{C|V_T|}{(q\pi R^2 L)}. \tag{18}$$

where the gate capacitance (C) was determined from the equation 19 [95] :

$$C = \frac{2\pi\epsilon_0\epsilon_{eff}L}{\cosh^{-1}\left(\frac{t_{ox}+R}{R}\right)}. \tag{19}$$

with $\epsilon_{eff} \approx 2.2$ is the effective dielectric constant of the SiO_2 dielectric, ϵ_0 is the permittivity of free space, t_{ox} = 250 nm is the thickness of dielectric, R = 50 nm is the NW radius and L = 10 μm is the channel length of NW FET. Equation 19 is the capacitance of a structure comprising of a metallic cylinder above a conducting plate and its use in this work with NWs of radius 50 nm positioned over an oxide of thickness 250 nm is justified.

Using equations (18) and (19), the hole concentration in the NW at room temperature is estimated to be 1.96×10^{16} cm^{-3}. From the linear part of the I_{ds} vs V_{gs} dependence Fig.3.5,

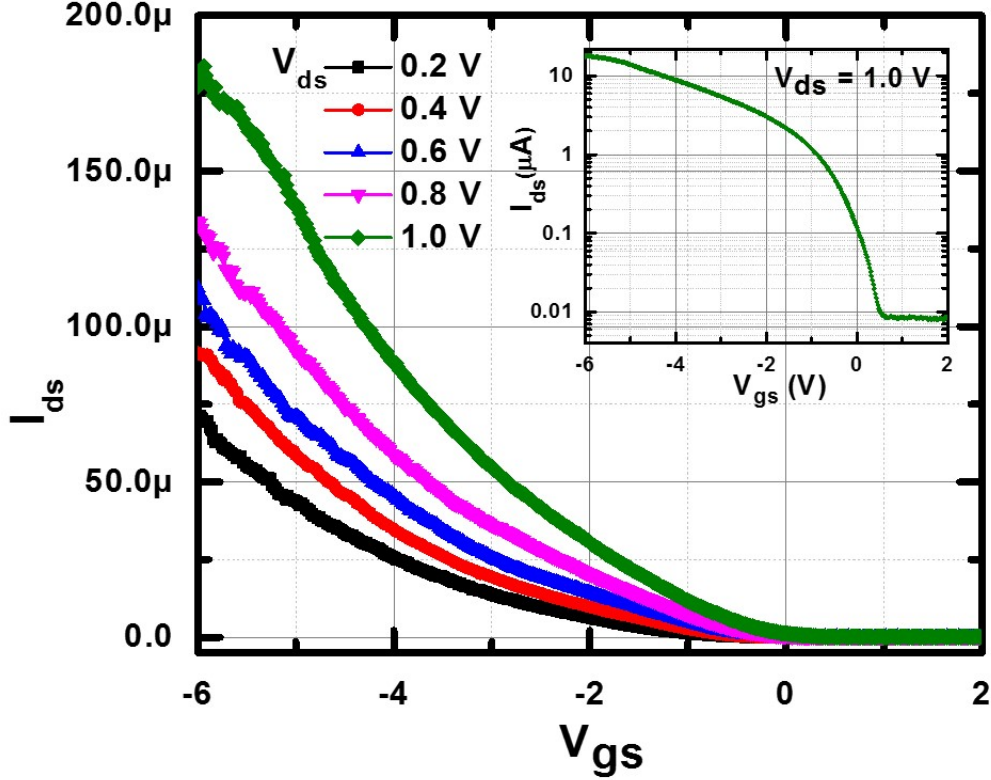

FIGURE 3.5. Transfer characteristics of InSb NW back-gated FET at increasing V_{ds} from 0.2 V to 1.0 V. Inset shows a logarithm plot of the $I_{ds} - V_{gs}$ curve at V_{ds} = 1.0 V. The on-off current ratio is estimated to be of the order of 10^3.

the field effect mobility (μ_{FE}) is determined at different constant V_{ds} by applying equation 20:

$$\mu_{FE} = \frac{L^2}{CV_{ds}} \times \left(\frac{dI_{ds}}{dV_{gs}}\right). \tag{20}$$

where transconductance $g_m = \left(\frac{dI_{ds}}{dV_{gs}}\right)$ is deduced at different constant V_{ds}. The peak field effect mobility was found to be 507 $cm^2V^{-1}s^{-1}$ at V_{ds} = 0.8 V. Our lowest mobility is 277 $cm^2V^{-1}s^{-1}$ at V_{ds} of 0.2 V which is higher than previously reported [96] value of 57 $cm^2V^{-1}s^{-1}$ obtained at V_{ds} = 0.1 V on unintentionally doped 5 μm long p-type InSb NWs grown by electrochemical method. Similarly, carbon doped p-type InSb NWs of length 1.8 μm were reported to have a mobility of 127±21 $cm^2V^{-1}s^{-1}$ at V_{ds} = 0.05 V [77]. As seen in the logarithm plot of I_{ds}–V_{ds} plot (inset of Fig.3.5), the p-type NW FET has a relatively

high on/off current ratio of 10^3. Though the surface and bulk of a stoichiometric InSb NW is intrinsically n-type, it was found when InSb is grown as an Sb-rich material it shows p-type behavior. This can be attributed to the two common defects in Sb-rich InSb: Sb antisite and In interstitial defects[97]. It is likely that the lower-pH (1.7) of the electrolyte favors adsorption of Sb anions on the growing crystal[98]. As the concentration of Sb in the NW increases, it introduces Sb antisite and In interstitial defects and this could account for the NW exhibiting p-type FET behavior.

Results of temperature dependent I-V measurements are shown in Fig.3.6(a). The linear nature of the I–V characteristics indicate that the Cr/Au contacts to the NW are ohmic contacts. The InSb NW was found to have a resistivity of 248 Ω.cm, which is higher than those reported for bulk InSb. Intrinsic defects like the Sb antisites and In interstitials as well as surface roughness of the NW (Fig.3.2(b)) are responsible for the extremely high resistivity. An increased resistivity was also measured by Alexander et al.[45] and V.N. Brudnyi et al.[99], attributed to a significantly reduced hole mobility caused by scattering at NW surface. As shown in the inset of Fig.3.6(b), the resistance of the InSb NW decreases with increasing temperature; the dependence being rather large at temperatures below room temperature. Such large temp dependence of resistance has been observed previously in InSb NWs[45, 100] and is characteristics of a semiconductor where carrier concentration varies exponentially with temperature. Using the device geometry, the NW conductivity was determined and a study of the variation of conductivity with temperature (Fig.3.6(b)) shows that below T = 200 K, the NW conductivity (σ) has a thermally activated character with equation 21:

$$\sigma = \sigma_0 exp\left(\frac{-E_a}{k_B T}\right), \tag{21}$$

where σ_0 is the pre-exponent factor, E_a is the activation energy, k_B is Boltzmann's constant (8.617×10^{-5} eVK^{-1}) and T is the absolute temperature. E_a is estimated to be about 0.1 eV corresponding to carrier generation across the band gap with activation energy equal to half of the band gap.

The roughness of the NW surface can be exploited to control phonon transport.

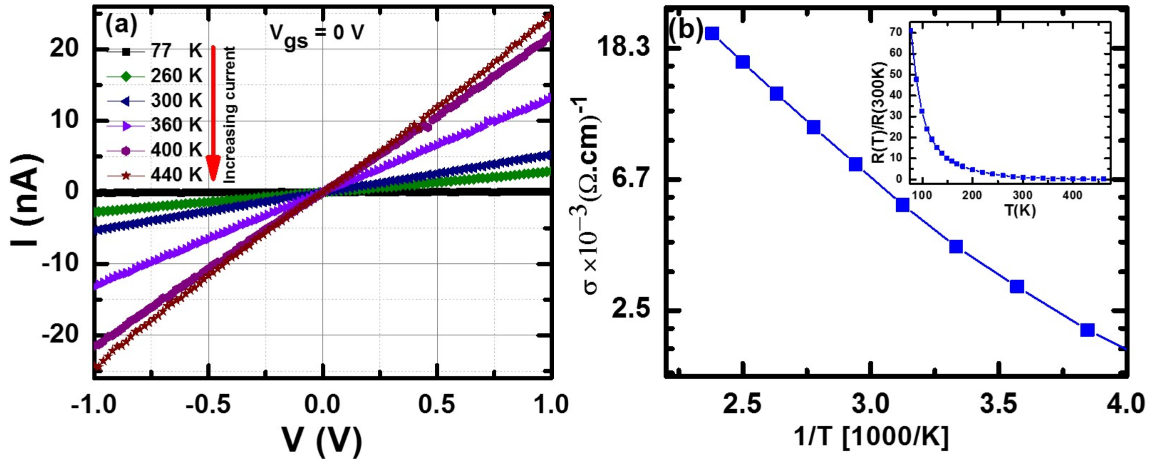

FIGURE 3.6. (a) Temperature dependent I-V shows current increasing with temperature, which is characteristic semiconducting behavior. (b) Temperature dependent conductivity measurements (Arrhenius plot) for the extraction of activation energy from a single InSb NW. Inset shows normalized resistance vs. temperature which shows the exponential decrease of resistance with increasing temperature.

Future work will hence be directed towards reducing the intrinsic point defects within the NW so that electrical conductivity can be enhanced, while the surface roughness can impede transport of phonons to reduce the lattice contribution to thermal conductivity, making it a promising material for thermoelectric applications.

3.4. Conclusion

Crystalline p-type InSb NWs of diameter $\sim$ 100 nm and tens of microns in length were grown at room temperature using a DC electrodeposition process. The NWs were found to be rich in Sb and had rough surfaces. Surface roughness, elemental analysis and the good crystalline quality of the NWs were confirmed via SEM, EDX, and Raman spectroscopy respectively. A p-channel InSb NW field effect transistor (NW FET) was fabricated using the electrochemically grown InSb NWs and the transfer characteristics at room temperature show decreasing drain-source current with increasing gate bias. The p-type behavior is most likely caused by a high concentration of Sb antisite and In interstitial defects in the NW.

These defects and the NW surface roughness adversely affect the NW conductivity and mobility, a fact that was verified by temperature-dependent conductivity measurements and three-terminal gate measurements.

CHAPTER 4

ELECTROCHEMICAL GROWTH OF INDIUM ANTIMONIDE NANOWIRES INFLEXIBLE POLYCORBONATE MEMBRANE[1]

This chapter is based on published work (indicated in the footnote) in which a dense array of vertically aligned InSb NWs with high aspect ratio (diameter 150 nm, length 20 μm) were grown in the pores of a track-etched polycarbonate membrane via a one-step electrochemical method. There are several reports on InSb NW growth in the pores of mechanically rigid, nano-channel alumina template (NCA), where NW growth occurs in the pores of the NCA. This work on InSb NW growth in pores of track-etched polycarbonate (PC) membrane sheds light on the various factors that affect nucleation and NW growth. The average length and diameter of the as-grown NWs was about 10 μm and 150 nm respectively. Two possible mechanisms accounting for two different morphology of the as-grown NWs are proposed. The polycrystallinity observed in some of the NWs is explained using the 3D 'nucleation-coalescence' mechanism. On the other hand, single crystal NWs with high density of twin defects and stacking faults grow epitaxially by a two-dimensional (2D) nucleation/growth mechanism. To assess the electrical quality of the NWs, two- and four-terminal devices were fabricated using a single InSb NW contacted by two Ni electrodes. It was found that at low bias, the ohmic current is controlled by charge diffusion from the bulk contacts. On the other hand, at high bias, the effects of space charge limited current (SCLC) is evident in the current-voltage behavior, characteristic of transport through structures with reduced electrostatic screening. A cross-over from ohmic to SCLC occurs at about 0.14 V, yielding a free carrier concentration of the order of 10^{14} cm^{-3}.

4.1. Introduction

One-dimensional NWs exhibit novel physical, optical and electronic properties, making them attractive for applications as interconnects and as nanoscale electronic, optoelec-

[1]This chapter has been reproduced as is from the publication "Structure and Electronic Properties of InSb NWs Grown in Flexible Polycarbonate Membranes", Nanomaterials,Volume 9, Page 1260, Published 5 September 2019.

tronic devices. Several types of NWs including metallic, semiconducting and organic NWs have been synthesized and of the semiconducting class of NWs, group III–V materials like indium antimonide (InSb) show great promise as devices [43]. InSb has a direct band gap of 0.17 eV at 300 K, and high electron mobility [44, 45] of 77000 $cm^2V^{-1}s^{-1}$. The small electron effective mass of 0.014,[44, 46] and large Lande g-factor of 51[46, 47], makes it a promising material in applications such as high-speed electronic devices, low-power logic transistors,[48, 49] NW field effect transistors (FETs),[50, 51, 52] infrared (IR) nano-optoelectronics,[53, 54, 55] thermoelectrics,[56, 57, 58, 59, 60] and magnetoresistive sensors[61].

There are several NW growth techniques including high temperature growth by chemical vapor deposition (CVD)[62] and high-vacuum growth by molecular beam epitaxy (MBE)[63]. In these cases, ordered growth of dense NW arrays requires patterning of the substrate with seed layers, the entire process requiring very sensitive control of the growth environment, resulting in a complex, expensive and non-scalable NW growth technique. An extremely successful approach for growing ordered arrays of NWs with high aspect ratio is electrochemical growth in non-conducting porous membranes. This relatively inexpensive and versatile growth can be performed at room temperature, and is preferred for growth of compound semiconductors like InSb where the difference in vapor pressures between In and Sb can result in non-stoichiometric growth at high temperatures. The technique is especially desirable for growing heterostructures since it prevents heat-induced inter-diffusion of elements across adjacent layers in the heterostructure. Another advantage is the possibility that the NW can be doped during the electrodeposition process, thus making it the method of choice for synthesis of nanostructured materials at low cost. There are several reports on growth of metallic NWs in pores of polycarbonate membranes, whereas most semiconductor NWs are grown in alumina templates. So, the first challenge is to determine an appropriate template, with the required geometry in terms of pore diameter, channel length and surface chemistry that will facilitate total removal of template after NW growth without compromising the surface or composition of the NWs.

The motivation for this study is the low-temperature synthesis of NWs in pores of a

flexible template. This is of interest in fabrication of stretchable devices that leads to promising applications in wearable and futuristic technology, including biometric and optoelectronic devices. Moreover, InSb NW growth in polycarbonate membranes allows producing NWs with uniform diameters and relatively smooth surfaces when compared with NW growth in alumina template. Though the pore density is significantly lower than anodized alumina templates, the realization of an array of NWs in a flexible PC membrane raises the possibility of realizing composite nanosctrutures with unique functionalities.

In this work, we study the efficacy of using track-etched polycarbonate (PC) membranes as a template for InSb NW growth. The PC membranes contain a high density of uniform cylindrical pores aligned perpendicular to the surface and penetrating the entire thickness of the template [64, 65, 66, 67]. It therefore allows for ordered growth of NWs, promising for applications related to energy[71, 72, 73] and electronic devices[74, 75, 76] where the array format of NWs is preferred; the major advantages of array-based devices being device density, process scalability, reproducibility in terms of dimensions and cost effectiveness[70]. There are works on InSb NWs grown in AAO template pores, but to the best of our knowledge there are no reports on InSb NW growth in PC membrane. In this paper, we present our findings on the synthesis and characterization results of InSb NWs that are electrochemically grown in template pores and we present a model explaining the role of electrodeposition parameters on the sample crystallinity.

4.2. Experimental Method

A commercial nanoporous PC track-etched membrane (Millipore Sigma), of pore length and diameter of ~ 20 μm and ~ 100 nm respectively was used for NW synthesis. A thin layer of gold (Au) (~ 200 nm) was thermally evaporated on to one side of the membrane using an Auto 306 (HHV Technologies) thermal evaporator. The Au layer functions as a contact electrode and also as the nucleation site for NW growth inside the porous template. Electrodeposition of InSb was conducted in a three electrode flat cell (Model K0235, Princeton Applied Research) with the template functioning as the working electrode, platinum mesh (2.54 cm $\times$ 2.54 cm) as a counter electrode, and Ag/AgCl as a reference electrode.

A potentiostat (Princeton Applied Research, model: 263A) was used to apply a constant potential (between -1.0 and -1.5 V) with respect to the reference electrode (Ag/AgCl) for the entire electrodeposition time period of 15 mins. The value of the applied potential was decided based on data obtained from cyclic voltametry experiment discussed in the next section. The electrolyte was a solution containing 0.15 M indium chloride ($InCl_3$), 0.1 M antimony chloride ($SbCl_3$), 0.36 M citric acid ($C_6H_8O_7H_2O$), and 0.17 M potassium citrate ($C_6H_5K_3O_7$) and its pH value was adjusted to 1.8.

Post-growth, the PC membrane was carefully rinsed several times with DI water and subsequently placed in a clean Corning Centristar centrifuge vial as part of the procedure to dissolve the template and allow NWs to be extracted from the template pores. Using a disposable pipette, few drops of dichlorobenzene solution were added to the vial and after 10 minutes of gentle agitation, the solution was sonicated for about 5 seconds. The visual impression at this stage was that the PC membrane was completely dissolved. However, there are some traces of the membrane that remain in solution. The sonication process was found to be aggressive and resulted in breakage of NWs and so its duration was kept very short. To remove traces of the membrane that stick to the NW surface, the solution containing NWs was diluted with isopropyl alcohol (IPA) and centrifuged (Hermle model Z206A) at 3000 rpm for 2 minutes. The residue at the bottom of the vial contains the NWs and so this residue was repeatedly ($\sim$4 to 5 times) treated with dichlorobenzene followed by IPA wash. The NWs were finally placed in a vial containing IPA and its concentration in solution was adjusted by varying the volume of IPA.

To characterize the as-grown InSb NWs, an electron microscope (JEOL JSM 7001F SEM and Hitachi SU1510) equipped with energy dispersive x-ray spectroscopy (EDX) was used to study the morphology and composition of the NWs. To study the crystalline nature of the NWs, the NWs were placed on a lacy carbon TEM grid and studied by transmission electron microscopy (TEM: A NION UltraSTEM 200 scanning transmission electron microscope equipped with a 3rd generation C3/C5 aberration corrector operating at 200kV) and Selected Area Electron Diffraction (SAED). The NWs were also characterized by Raman

spectroscopy where the spectrum was recorded at ambient temperature on a Nicolet Almega XR Dispersive Raman spectrometer, using a 532 nm green laser. High resolution X-ray diffraction studies were performed using a Rigaku Ultima III XRD with CuKα tube (λ = 1.5406 A^0). For electron transport measurements, a droplet of the solution containing the NWs was placed on $SiO_2(200\ nm)/n^+Si$ substrate and an isolated, sufficiently long NW was identified under a scanning electron microscope (JEOL JSM 7001F) and its position marked with reference to pre-patterned markers. Two electrodes separated by 1.5 μm were defined by electron beam lithography (JEOL JSM 7001F with XEON patter writer). Prior to metal (300 nm thick Ni film) deposition, a reactive ion etch (AGS RIE MPS-150) "descum" process was used to ensure excellent metal film adhesion by removing any remaining resist not fully washed away by development. Nickel has a work function that closely matches that of InSb and so is expected to provide good ohmic contact to the NW. Following lift-off of the resist, the device comprising of a single NW contacted by Ni electrodes was studied using an Agilent B1500A semiconductor parameter analyzer.

4.3. Results and Discussions

InSb NW growth occurred under potentiostatic conditions through a multi-step reaction process involving various ions responsible for the electrochemical deposition of InSb [101, 102]. With reference to Ag/AgCl electrode, the balanced reaction and the overall electrode potential for indium (In) and antimony (Sb) deposition is expressed as:

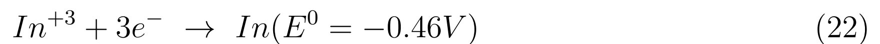

$$In^{+3} + 3e^- \ \rightarrow \ In(E^0 = -0.46V) \tag{22}$$

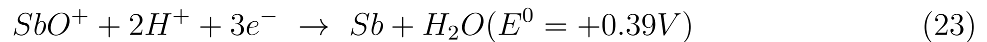

$$SbO^+ + 2H^+ + 3e^- \ \rightarrow \ Sb + H_2O(E^0 = +0.39V) \tag{23}$$

Prior to electrodeposition, the equilibrium deposition potential was determined using cyclic voltammetry and three different deposition potentials of -1.0. -1.25 and -1.50 V was used to grow NWs. A reduction potential more cathodic than -0.46 V is needed to deposit the NWs. Cyclic voltammetry (CV) was used to help determine the best deposition potential for the plating bath. Fig. 4.1 shows the data from the CV experiment, where the potential

was swept in the cathodic direction beginning at +0.0 V to -2.0 V and back to +0.5 V. There is minimal current flow until close to ≈ -0.5 V, where the current increases rapidly to the final potential at -2.0 V. A small reduction peak can be seen at ≈ -1.0 V corresponding to the deposition of InSb. At a more cathodic potential than -1.0 V, the current continues to increase and bubbles can be observed corresponding to hydrogen evolution at the substrate surface. To ensure a stoichiometric InSb deposition, potential values greater than -1.0 V are applied to the working electrode. The rates of reduction for both In^{+3} and Sb^{+3} ions in solution can be controlled by careful selection of the electrochemical parameters (i.e. pH, temperature, potential, concentrations) facilitating co-deposition.

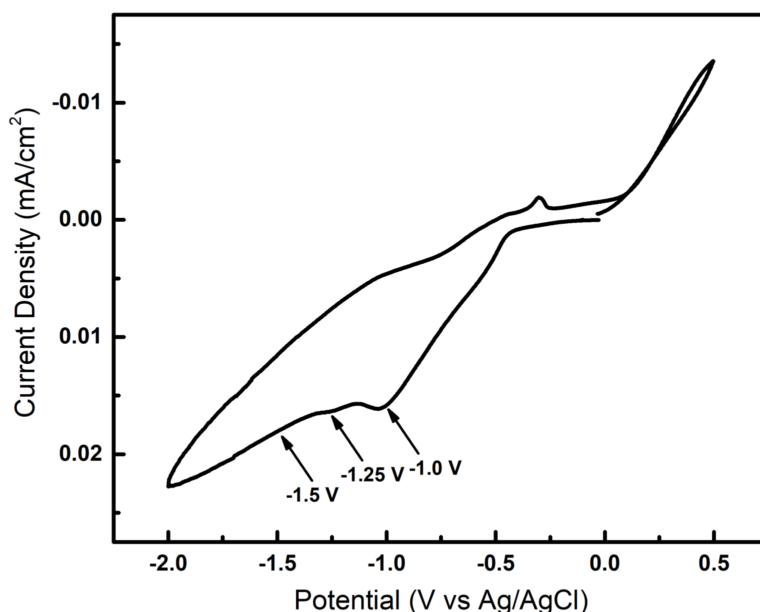

FIGURE 4.1. Results from cyclic voltammogram showing variation of current with positive (oxidizing) potentials and negative (reducing) potentials. Increasing the negative potential beyond -1.5 V leads to hydrogen evolution.

Likely In and Sb exhibit an anomalous codepostion mechanism where the nucleation of one species affects the deposition of another species in solution. This is common in iron based alloys and also seen in other semiconductor electrodepostion reactions[103, 104]. The

implication of a high negative electrode potential on the stoichiometry of InSb thin films has been discussed by Ortega et al.[105]. Most InSb electrochemical depositions therefore occur at about -1.5 V. The reactions involved in the NW growth mechanism is most likely more complex and the quality of the growing crystal, its morphology and composition were found to be critically dependent on the pH value of the electrolyte, the applied potential as well as the type and aspect ratio of the template pores in case of template-assisted electrochemical growth. As seen in Fig.4.1, as the voltage is swept to -2.0 V, a reduction peak occurs around -1.1 V; the increase in cathodic current beyond this voltage results in hydrogen evolution. Based on the cyclic voltammetry data, InSb NW synthesis was performed under potentiostatic conditions at three different potentials: -1.0, -1.25 and -1.50 V.

The nucleation and growth kinetics of InSb deposition on Au electrode in the PC membrane was studied using the current transient technique for the three different applied potentials (Fig.4.2).

The mechanism depends strongly on the InSb–Au interaction and since the Au film was thermally evaporated on the back of the PC membrane it is most likely an amorphous film which does not provide any epitaxial influence to the NW growth process, which is not a steady state process. As seen in the curves of Fig.4.2, the plot resembles the classical Stranski-Krastanov (S-K) (layer + island) growth model with the current–time transient showing four characteristic regions: (i) a sharp drop in the initial current density due to discharging of the double layer. The thickness of the double layer depends on the total ion concentration in the electrolyte. The decrease in current signifies the stage where NW growth is initiated as the In and Sb ions diffuse through the double layer to the Au electrode at the bottom of each pore, following Fick's first law. (ii) a constant low current region (induction period t_{ind}) corresponding to the nucleation time, when many nuclei with random orientation form on the Au nanostructured surface inside the pores. As seen in the plot, t_{ind} varies with deposition potential and in this particular experiment, its value was a minimum at the higher deposition potential of -1.50 V. t_{ind} varies for each run, indicative of the randomness of the nucleation stage. It was also noted that at the large negative potential of -1.5 V, there was

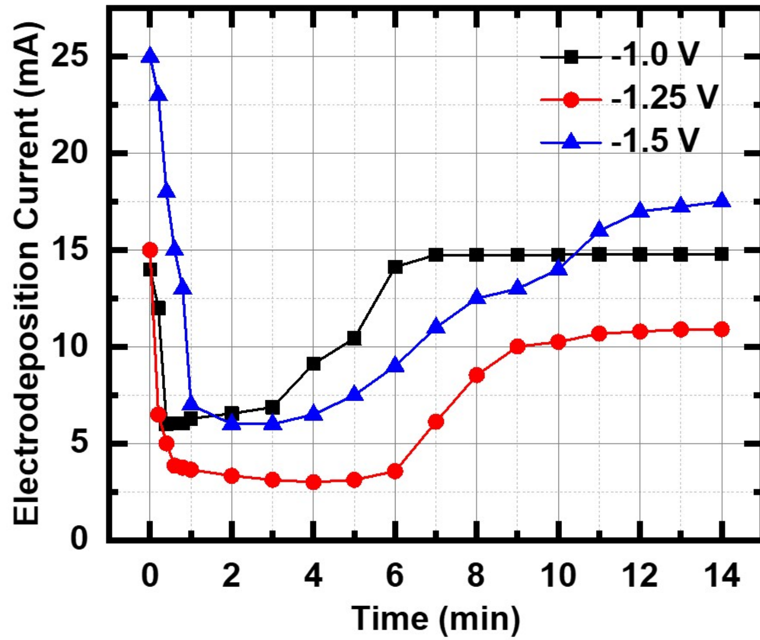

FIGURE 4.2. Current transient of room temperature InSb NW growth in Au-coated polycarbonate membrane at three different deposition potentials: -1.0 V, -1.25 and -1.50 V.

some hydrogen evolution from the pores, a process that gets faster as the negative potential is increased. (iii) an increase in the current density corresponding to growth of columnar structure inside the pores. The magnitude of the current density and the growth period depend on the electrolyte composition, nature of the working electrode, pH of solution, deposition potential etc. (iv) a limiting (steady state) current, where the current magnitude is limited by diffusion of the ions to the top surface of the template [91].

To investigate the effect of electrodeposition on the template morphology, the PC membrane was first studied to verify the pore density and pore-size. Fig.4.3(a) is an SEM image of the blank PC template, showing variable pore diameters and shapes and indicating about 20% porosity.

A magnified section of the template (indicated by the square in Fig.4.3(a)) clearly shows that the pores are not uniformly spread out over the membrane surface (Fig.4.3(b)),

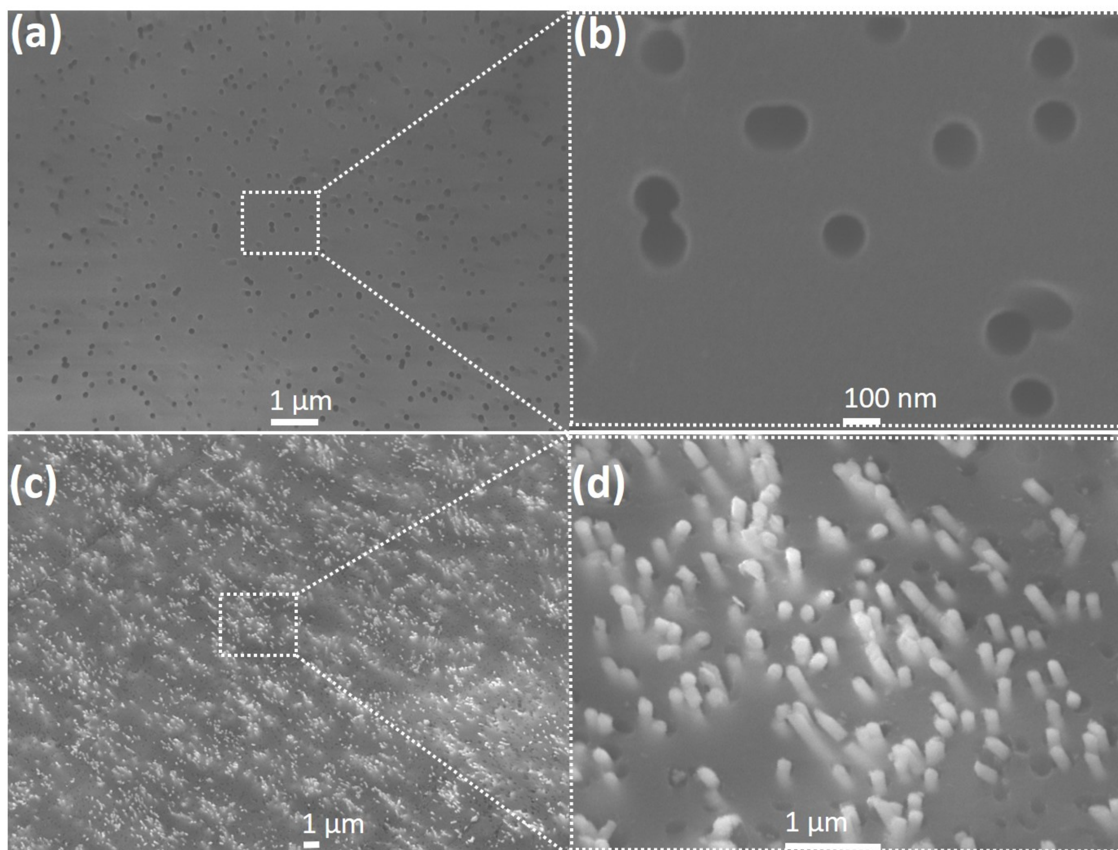

FIGURE 4.3. SEM images of blank polycarbonate membrane before and after growth of InSb NWs (a) SEM image of bare polycarbonate template (b) Zoomed in SEM image of polycarbonate template with different diameters and shapes of pore, ranging from $\sim 150 - 200$ nm (c) SEM image of InSb NW exposed tips after 30 seconds of oxygen plasma etching, and (d) Zoomed in SEM image of exposed tips of InSb NWs.

unlike those found in alumina templates. Following InSb NW growth at -1.5 V, the template surface was etched with O_2 plasma for 5 min at 100 Watts and 100 mTorr pressure and examined under the SEM. As seen in Fig.4.3(c), NWs grew profusely in the template pores and their tips are clearly visible. A zoomed-in version of the marked section of the membrane is shown in Fig.4.3(d). This image showing protruding tips of the NWs verifies that NW growth occurred in the template pores. The NWs were then released into solution (following procedure explained in previous section); a droplet of this solution was found to contain a

high density of uniform NWs, as seen in the SEM image of Fig.4.4(a).

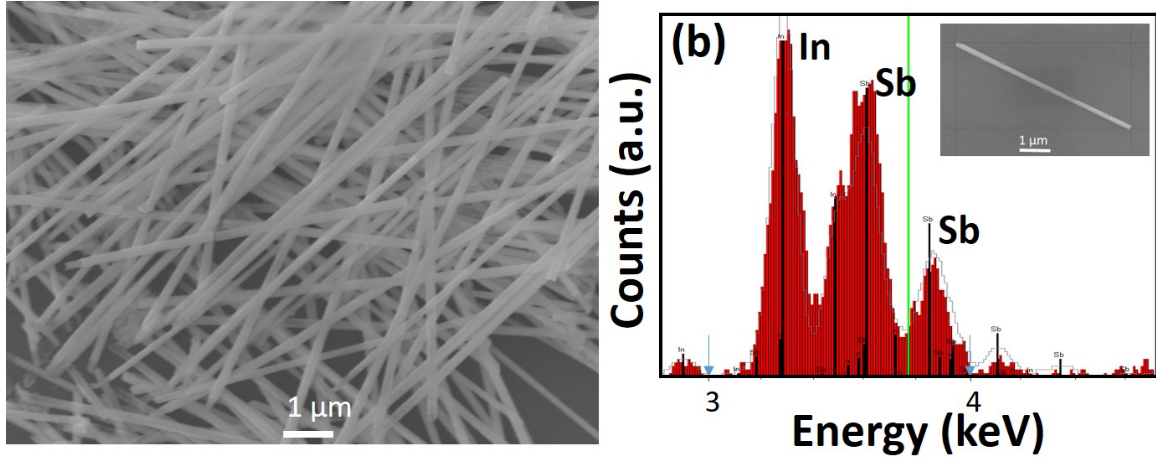

FIGURE 4.4. (a) SEM images of bundle of InSb NWs after drop casting on silicon wafer (b) EDX spectrum of a single and short (∼5 μm) InSb NW, that is shown in the inset of figure (b).

The NWs tend to clump together and efforts to separate them by sonication resulted in breakage, most likely caused by mechanical stress induced by the process. The as-grown NWs were found to have uniform diameters but varied lengths; the average length of the NWs was determined to be about 10 μm, comparable to the thickness of the template. The NWs had diameters in the range of 120 – 150 nm, corresponding to the template pore diameter. EDX analysis of a single NW (inset of Fig.4.4(b)) shows a stoichiometric composition (Fig.4.4(b)).

Fig.4.5(a-c) shows the Raman spectrum obtained from a single or a few InSb NWs (shown in figure inset). The Raman spectrum for all three deposition potentials is dominated by the peak at about 147-149 cm^{-1} and a wide peak centered at 120 cm^{-1}. These peaks have been reported by other works[91, 92], and are assigned to TO-TA and 2TA phonons. They have been attributed to defects and also to the amorphous/polycrystalline nature of the NWs [106, 107, 108]. The peak at 149 cm^{-1} has been attributed to a high density of Sb-Sb bonds, typically found in a-InSb [109].

The presence of Sb related defects is most likely related to growth related parameters

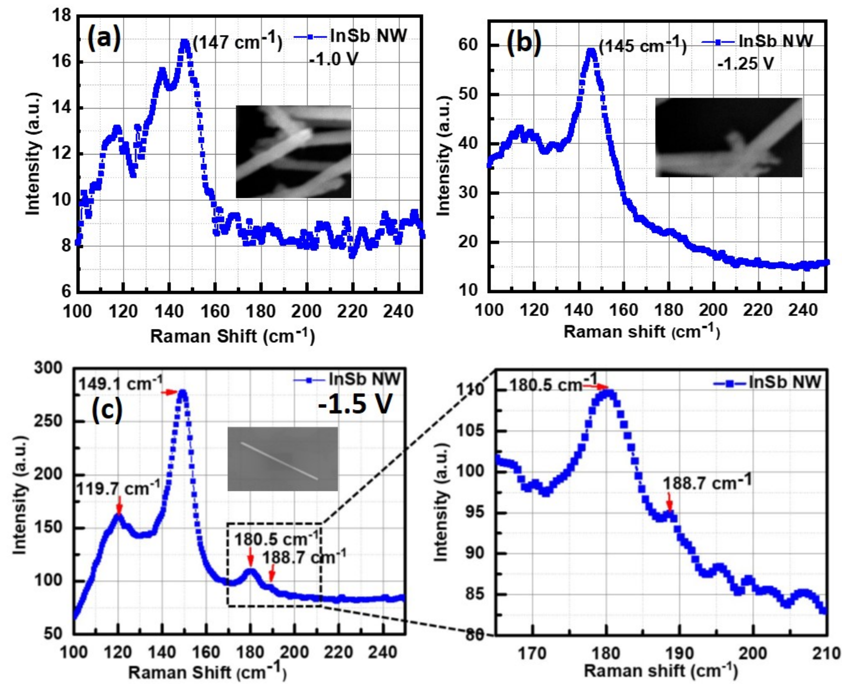

FIGURE 4.5. Raman spectrum of electrochemically grown InSb NW in porous polycarbonate template. (a) At a deposition potential of -1.0 V, spectrum shows characteristic defect related peak at 147 cm^{-1} and around cm^{-1}. No peaks were observed in the 180 – 190 cm^{-1} range, which is the region where peaks corresponding to crystalline InSb are typically measured; (b) Spectrum obtained for growth at -1.25 V shows similar defect related peaks as observed in (a). Absence of any peak in the 180 – 190 cm^{-1} range (c) Spectrum obtained from NWs grown at -1.5 V. Well-defined peaks were observed at 149 cm^{-1} , around 120 cm^{-1} and around 181 cm^{-1}. The zoomed in Raman spectrum image shows two distinct peaks at 180.5 $cm^{-1}$and 188.7 cm^{-1} which is assigned to the c-InSb TO and LO phonon modes, respectively. In all three cases, the Raman peaks measured in the range from 145 – 149 cm-1 is attributed to TO-TA modes and is believed to originate from defects in the NWs, as is the peak around 119.7 cm^{-1}.

like the deposition potential and pH of electrolyte. So, though the SEM images showed relatively smooth NWs, the amorphous/polycrystalline nature of the as-grown NWs was first

evident in the Raman spectrum. There was a difference in the Raman spectrum obtained from a single InSb NW grown at -1.5 V. The room temperature spectrum reveals peaks of TO and LO phonon modes at 180.5 cm^{-1} and 188.7 cm^{-1} respectively, which matches closely with the TO and LO peaks reported in previous studies on InSb NWs [43, 87, 88, 89, 90]. Fig.4.5(b) is a zoomed-in view of these two peaks, which are typically reported in c-InSb NWs.The lack of crystallinity in NWs grown at very low deposition potentials deserves further investigation. Since the crystalline peaks were only found in NWs grown at -1.5 V, all further analysis including XRD measurements, HRTEM and electron transport measurements were done on NWs grown at this potential (-1.5 V).

To verify the findings from Raman measurements and to further investigate the orientation and crystalline quality of the NWs, x-ray diffraction studies were performed on the NW array grown at -1.5 V. Since it is very difficult to get XRD pattern from a single NW, XRD pattern was taken from NWs embedded in the PC membrane. It was first verified that a bare template does not give any XRD signal. Only templates that were filled with NWs produced an XRD pattern (shown in Fig.4.6).

Inset of Fig.4.6 shows the SEM image from where XRD data was collected. The InSb diffraction pattern matched the JCPDS file (00-006-0208) for a cubic zinc blende crystal structure. The sharp peak around $2\theta = 23.70^o$ corresponds to (111) crystallographic direction, while the peak at $2\theta = 39.36^o$ corresponds to the (220) direction. The reflections ((111), (220), (311), (400)) corresponded to a random crystal structure with no preferred orientation. Another peak is observed at $\approx 33.71^\circ$, probably due to a thick oxide layer around the NWs. The presence of this oxide layer is also confirmed by TEM. The lattice constant along different lattice planes was calculated and the average value was estimated to be 0.658 nm, with an average mismatch of about 1.55 %.

In order to probe the microstructures of the as-grown InSb NWs and obtain information about its crystallographic orientation, structure and surface, results from transmission electron microscopy as well as high-angle annular dark-field (HAADF) scanning transmission electron microscopy (STEM) measurements were analyzed. These studies revealed that two

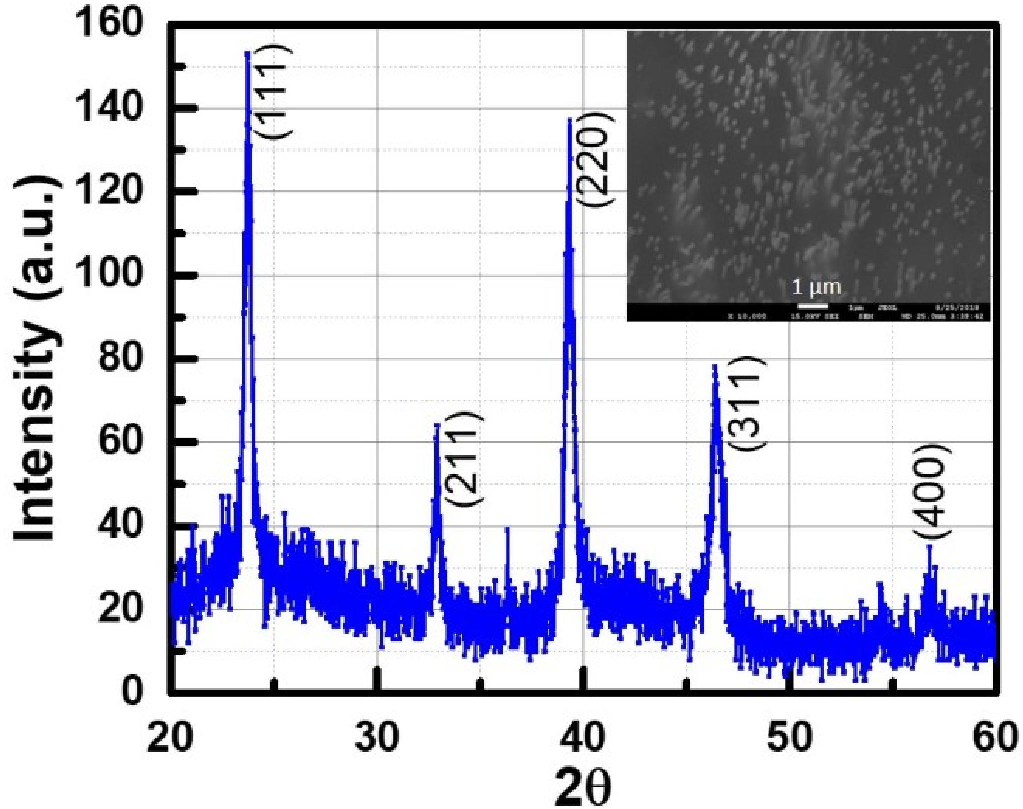

FIGURE 4.6. XRD spectrum of as grown InSb NW in polycarbonate template.

types of NWs were grown in the template pores: one type was composed of polycrystalline NWs that under low magnification appeared to have a smooth surface. The second type of NW was found to have a rough surface. (Fig. 4.7(a)) shows an HAADF image of a smooth wire, in which the grain size is on the order of 50 nm (estimation based on what seems to be about 3-5 different grains as seen in the Fast Fourier Transform (FFT) of the image); the inset depicts a FFT of the image confirming its polycrystalline nature. An individual grain oriented to be viewed along its [111] zone axis is observed in the atomic resolution HAADF image in(Fig. 4.7(b), where the measured distance between atomic columns is 0.28 nm .

The presence of a complex microstructure with randomly oriented nanocrystals in these NWs was also revealed in the indexed rings in the SAED pattern of Fig. 4.7(c) that shows diffraction patterns corresponding to the lattice indices of face-centered cubic (fcc)

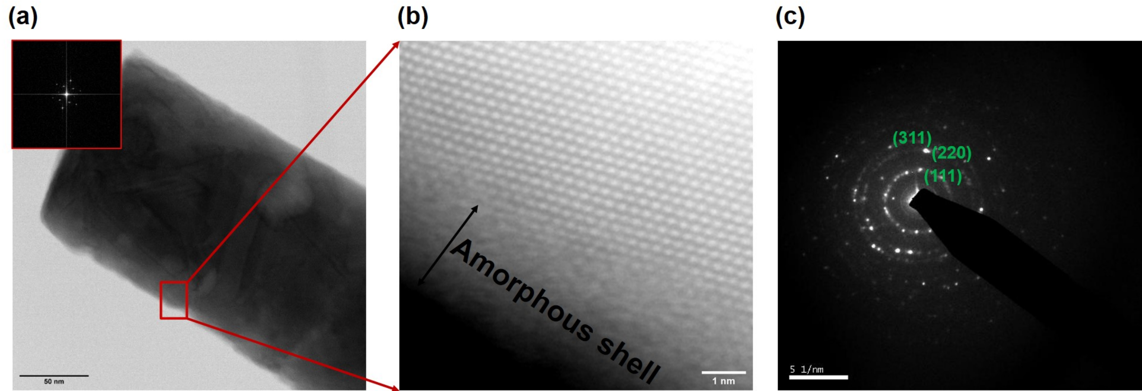

FIGURE 4.7. STEM images taken along a single InSb NW clearly showing the presence of an amorphous oxide shell: (a) ABF-STEM image of a relatively smooth NW that shows several crystal grains; inset shows FFT of the image indicating multiple crystallographic orientations; (b) magnified HAADF-STEM image of outlined region in (a), looking down the (111) direction of one of the larger grains, with a measured distance of 0.25 nm; (c) selected area diffraction pattern (SAED) shows indexed rings with discrete spots confirming polycrystalline nature of the NW.

InSb.

An example of a NW with a rougher surface can be seen in the HAADF images of Fig. 4.8(a) – (c) respectively, where the parallel stripes observed in (b) and (c) indicate the presence of stacking-faults and twinning defects.

A magnified section of the wire from Fig. 4.8(a) shows a high density of twin defects and stacking faults, the most likely cause for the rough-surface morphology in the as-grown NWs.The rough NWs are therefore not a perfect single crystal, but rather one with a dense distribution of stacking faults. Such crystal defects are common in metal NWs grown in template pores, and has been explained based on low-dimensional growth in spatially confined pores of the template [110]. In both types of NWs, an amorphous layer was clearly visible on the NW surface and its composition as determined by EDX was of In_2O_3. The presence of an oxide was also seen in the XRD spectum of Fig.4.6. A model of the zinc blende InSb along the (111) and (220) directions [111] reveals that along the (111) direction,

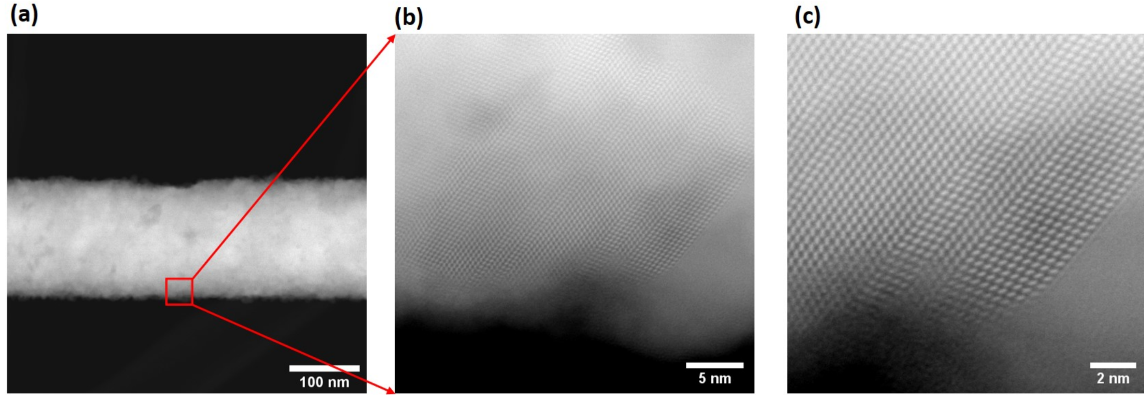

Figure 4.8. (a) HAADF-STEM image taken from a significantly rougher NW; (b) HAADF image of outlined region in (a) showing presence of crystal defects which accounts for the observed roughness in the NW; (c) magnified HAADF image of (b) showing twin planes and stacking faults.

one can only see the Sb atoms with an atomic separation of around 0.37 nm, validating our observation of similar spacing measured in the HAADF-STEM images of Fig. 4.7. Similarly, it has been reported that along the (220) direction, the separation between In and Sb atoms is about 0.23 nm, which explains the measured spacing of about 0.25 nm measured in the FFT analysis. The two major lattice spacing measured in the HAADF image (Fig. 4.8(c)) was determined to be about 0.37 nm and 0.23 nm corresponding to the (111) and (220) direction respectively of zinc blende InSb.

Based on our experimental findings of two distinct NW morphologies observed in a single growth cycle, we conclude that different growth modes are at play in their formation. From the growth curves of Fig.4.2, the layer + island growth mode that is characteristic of the S-K growth mode was implicated, which accounts for the observed polcrsytallinity in the as-grown NWs.

Another competing mechanism that controls NW morphology is the Frank–van der Merwe growth mode, where a 2-D nucleus forms and NW growth occurs layer by layer. However in this growth mode, compressive strain in the growing layer imposed by the confined pore environment as well as lattice mismatch between the metal electrode and the growing layer results in crystal growth with lot of defects. There are several works explaining

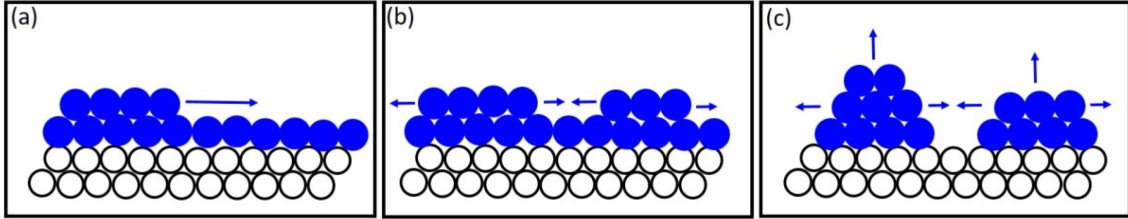

FIGURE 4.9. A schematic of the 'nucleation-coalescence' growth mechanism, where: (a) a few monolayers of InSb grow on the Au electrode; (b) islands from over the monloayer; (c) coalescence of the islands to form individual crystals/grains.

polycrystallinity in Au [112], Ni [113] NWs. In these works, it has been proposed that polycrystalline NW growth most likely follows the 3D 'nucleation-coalescence' mechanism. A schematic of this growth mechanism is shown in Fig.4.9. The first stage of growth involves the formation of a few angstroms of InSb on top of the metal seed (Au) that exists at the bottom of the template pores (Fig. 4.9(a)). As growth proceeds, isolated islands form over this crystalline layer and coalesce to form a linked network (Fig. 4.9(b, c)). The growth mechanism is sensitive to the growth environment which includes the condition of the template pore interior, the nature of the electrodes at which nucleation begins, the electrolyte and the deposition potential. It has been reported [113] that in electrochemical deposition, there exists a critical dimension d_c, beyond which new crystals form. For single crystal growth, the value of d_c should be large and the most appropriate way to achieve this is to maintain a low deposition potential. It is worth noting that electrochemical growth of NWs in template pores is a complicated process and the NW quality is affected by the movement of ions in the pores, process of diffusion, reaction and adsorption to the metal seed at bottom of pore. All of these factors are related to deposition conditions and influence the growth modes, which in turn are influenced by surface energy of the growing layers. For a 2D-nucleus growth, the critical size of a 2-D nucleus d_c is inversely proportional to the square of the overpotential [114], whereas for a 3D-like nucleus d_c is inversely proportional to the cube of the overpotential. At the higher deposition potential of -1.5 V, the surface diffusion of In

and Sb atoms favors their aggregation resulting in nucleation and growth of several small 3-D crystals that grow simultaneously and independently of each other during the first few minutes of growth. The polycrystalline NWs showed relatively large grain sizes (about 50 nm), which implies that single crystal growth of semiconductors like InSb in template pores is affected by several factors unlike what has been observed in growth of metallic NWs.

On the other hand, if the growth environment in the membrane pores is such that it inhibits the formation of several 3-D nuclei, and instead a 2-D nucleus forms, then it favors single crystal growth. NW growth in this case follows the two-dimensional (2D) nucleation/growth mechanism. Since growth occurs in a confined pore, lateral stresses develop in the growing crystal as a result of the confined growth process. This results in the growth of InSb NWs with high defect density. The process effectively forces the NWs to crystallize in the cylindrical geometry of the membrane pores, resulting in formation of stacking faults as the crystal growth rate in different directions were disturbed. This results in formation of 111 stacking faults and twin defects of the NW crystal lattice. The high density of defects is responsible for the rough morphology of some of the InSb NWs.

To assess the electronic quality of the NWs, current-voltage measurements were made on a single InSb NW that was contacted by Ni electrodes is shown in Fig.4.10.

Fig. 4.11 shows the experimental I-V curves on a linear and a double-logarithmic scale. As seen in this plot, the fairly symmetric non-linear I-V plot shows two distinct regions: (i) at small bias I $\propto$ V, (ii) At larger bias, I $\propto V^2$. This behavior is characteristic of space charge limited current (SCLC) that is typically observed in very resistive materials with ohmic contacts[115]. The contacted cylindrical NWs have a contacted length of 3.0 μm which is much greater than the NW radius of 100 nm (L >>R).

This results in reduced electrostatic screening effects which implies that charge injection effects by the contacts will be much higher on these devices as compared to a bulk structure. Since the electrical contacts to the two ends of the NW are symmetric, it leads to fairly symmetric I-V plots for positive and negative bias. Since we do not observe any exponential trend in the lot, we do not consider Schottky barriers at the contacts. We therefore

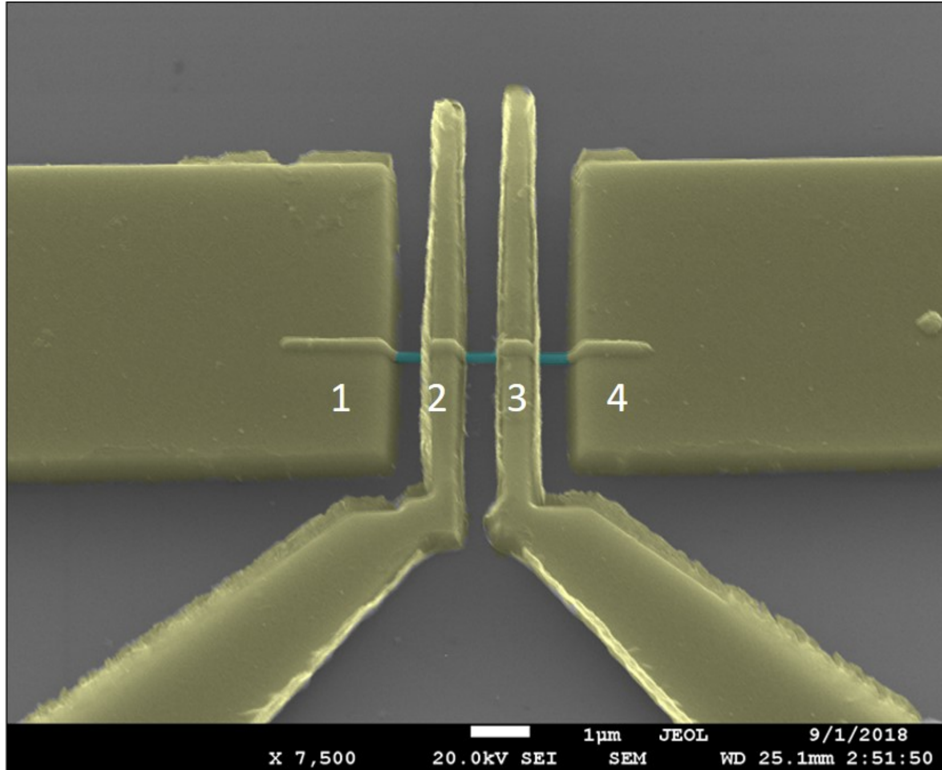

FIGURE 4.10. SEM image of single InSb NW contacted by four Ni electrodes. The NW was placed on a 200 nm thick silicon dioxide (SiO_2) grown over a highly dopedp^+ Si substrate. The channel length between each electrode is about 1.5 μm. The metal electrodes are Cr (5 nm)/Ni (200 nm). Cr enables better adhesion of Ni film on the SiO_2 layer.

believe that the current changes from ohmic at low bias to SCLC at high bias. Using a four-terminal device configuration, it was also verified that the contact resistance was much lower than the wire resistance. In the low bias regime, the as-grown NW has a resistance of the order of 10^9 Ω, while the contact resistance is of the order of kΩ. The high NW resistance is to be expected at low bias, since in this bias regime the injected electron concentration is low compared to the equilibrium electron concentration and the magnitude of the current follows Ohm's law where I $\propto$ V. The cross-over point in the I-V characteristics occurs at about 0.14 V, which is most likely the point at which the injected electron concentration exceeds the equilibrium electron concentration. Since the contact dimensions are much larger than that of the NW, the behavior of the current variation with bias in this regime is expressed by

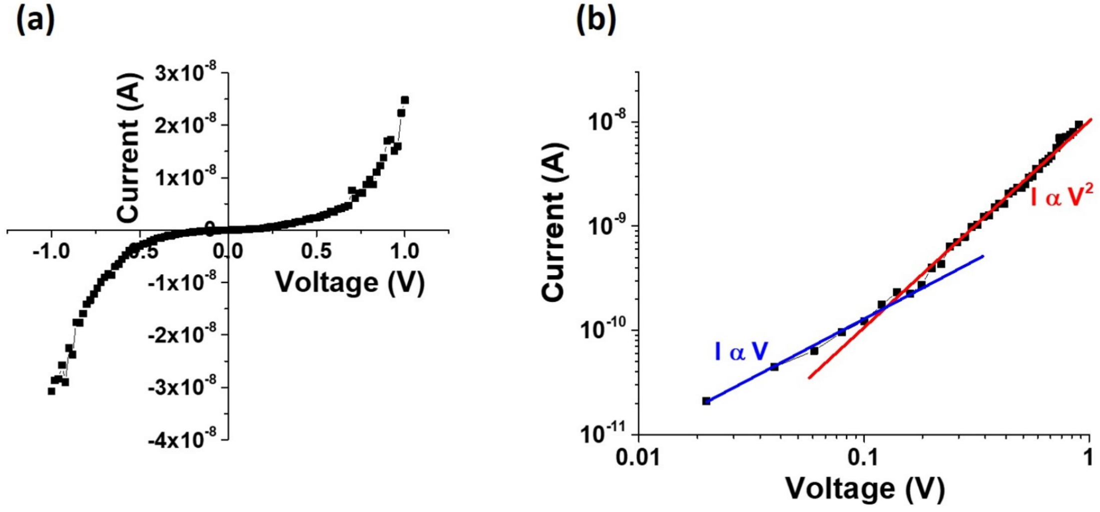

FIGURE 4.11. Current-voltage measurements on a single as-grown Insb NW. the NW diameter and electrode spacing are 190 nm and 1.5 μm respectively. (a) Symmetric non-linear I-V curve on linear scale. The curves are linear (ohmic) at small bias and transforms at high bias; (b) I-V curves plotted on a logarithmic scale, showing a crossover to SCLC at $V_x = 0.14$ V.

Mott-Gurney law in which I $\propto V^2$. From the I-V curve of Fig. 4.11, the cross-over voltage of $V_x = 0.14$ V is used to make a rough estimate of the free carrier concentration in the NW, using the equation [115]

$$n = \frac{\epsilon_0 V_x}{(e\pi R^2 ln(L/R)} \tag{24}$$

where ϵ_0 is the permittivity of free space and L and R represent the NW dimensions. Using this model, the free carrier concentration is estimated to be of the order of $10^{14}\ cm^{-3}$. This value is about an order of magnitude lower than that reported for undoped bulk c-InSb. This discrepancy could be attributed to the fact that in using equation 24, we have assumed that the symmetry in I-V characteristics is indicative of a symmetric electric filed created by the contacts around the NW. However, with the polycrystalline NWs, the conduction will be non-uniform and the presence of defects like stacking faults could further impact the conduction mechanisms. SCLC is typically observed in undoped NWs with low free carrier

concentration where the ohmic current is controlled by charges from bulk contacts diffusing through the NW, rather than from impurities or dopants. The effect of polycrystallinity on the conduction mechanism and hence on the SCLC is a topic for further study.

4.4. Conclusion

Polycrystalline and crystalline InSb NWs with high defect density were synthesized at room temperature using a DC electrodeposition process in porous polycarbonate membrane. The structural quality of the NWs was assessed by high resolution transmission electron microscopy, Raman spectroscopy and x-ray diffraction studies. An important parameter that determines the structural quality of the NWs is the critical grain size whose value changes with deposition potential. The Stranski-Krastanov growth mode best explains the growth of polycrystalline InSb NWs by a 3-D 'nucleation-coalescence' mechanism. On the other hand, the growth of crystalline NWs follows the Frank–van der Merwe growth mechanism that follows a 2-D nucleation epitaxial growth. On account of reduced carrier screening in the NW geometry, the phenomenon of space charge limited current was observed due to increased charge injection at high bias fields. At low bias, current follows the traditional ohmic behavior. The cross-over voltage was used to determine an equilibrium carrier concentration of 10^{14} cm^{-3}.

CHAPTER 5

FABRICATION OF NANOPOROUS ANODIC ALUMINUM OXIDE TEMPLATEBASED ON BARRIER LAYER THINNING AND SYNTHESIS OF COBAL TNANOWIRES IN THE TEMPLATE PORES[1]

5.1. Introduction

Anodic films on aluminum have received considerable attention due to their extensive application as templates for synthesizing various nanostructures in the forms of NWs and nanotubes. The previous two chapters were based on growth of InSb NWs in pores of commercially purchased templates: AAO and polycarbonate membranes. The challenge is using these membranes were:

1. The AAO membranes have fixed thickness of 50 μm. For electrochemical growth of NWs, it is important that the back-side of these templates be coated with a metal like Au to function as the working electrode. To enable this, a thin layer of metal is typically deposited by thermal evaporation onto the back-side of the AAO membrane. However, this task is extremely difficult since in most cases, the metal coats the edges of the pores and does not extend over the pore surface. Even after evaporating almost 700 mg of Au, it was found that the Au did not cover the pores. An SEM image of this challenge with different thickness of Au evaporated on the pore surface is shown in Figure 5.1 As seen in Fig (a), (b) the top and bottom surfaces of the template have different appearance. The correct surface is first identified by SEM and this is followed by metal evaporation on the back surface. The bottom surface has relatively thick walls and the pores appear embedded within these walls. This is the reason why coating the back surface with metal is a challenge. Upon evaporation, the metal typically deposits on the pore walls. As evaporation progresses, the pore walls get thicker which implies that the pores are deeply embedded within these walls. As seen in Fig. (c) and (d) the pore walls have gotten thicker but the pores are still visible.

[1]This chapter has been reproduced partially from the publication "Understanding the Mechanisms that Affect the Quality of Electrochemically Grown Semiconducting NWs", from the book "Semiconductors - Growth and Characterization" Chapter 2, http://dx.doi.org/10.5772/intechopen.71631.

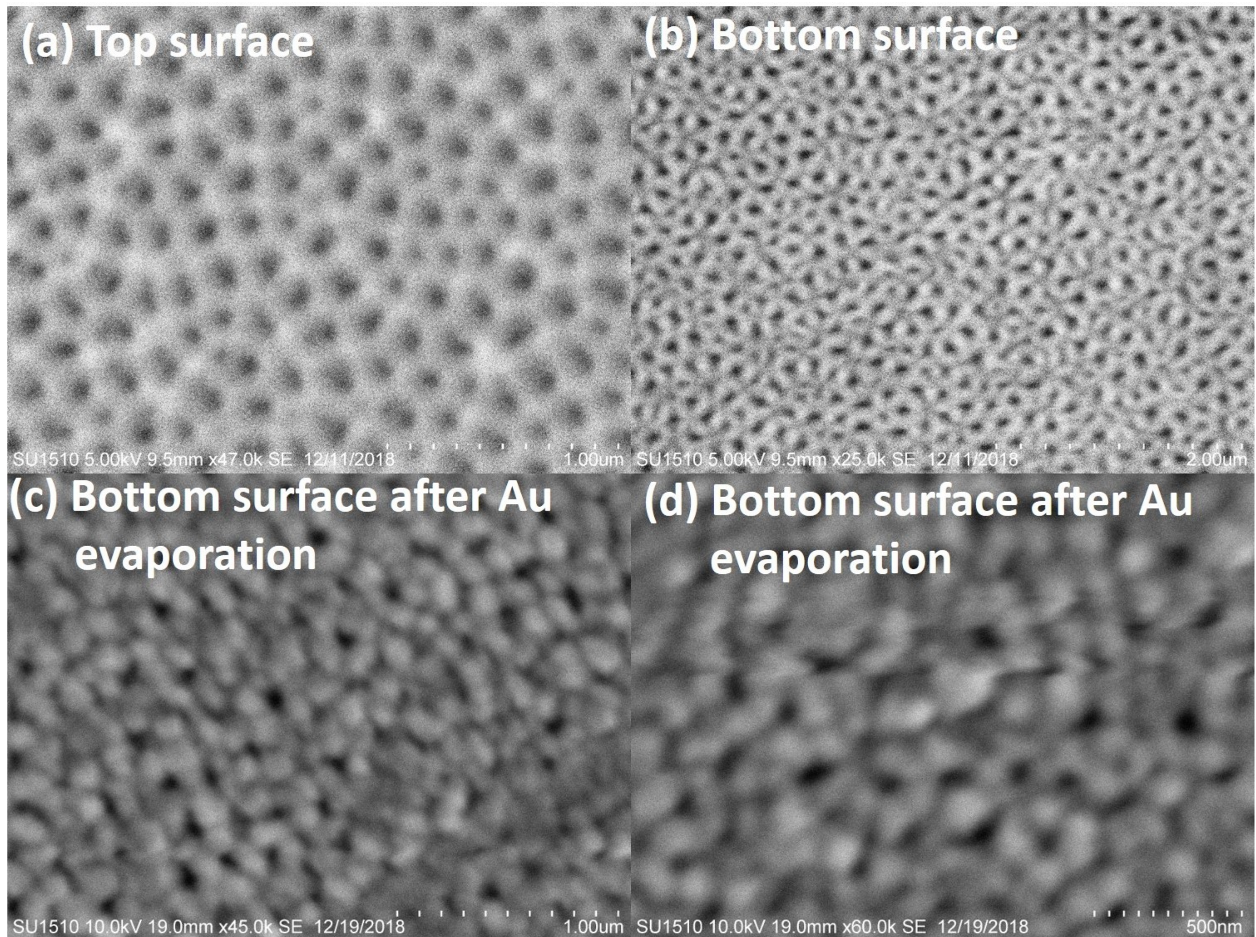

FIGURE 5.1. SEM images of top and bottom surfaces of AAO template (a) top surface at scale bar of 1 μm and (b)bottom surface with scale bar 2 μm, and after 800 mg of Au thermal evaporation (c) bottom surface at scale bar of 1 μm (d) bottom surface at scale bar of 500 nm. Open pores in (c), and (d) even after 800 mg of Au evaporation, is not ideal for electrochemical growth of NWs

If the metal does not extend over the pore surface, the NWs cannot grow since the solution contained within the template pore will see an empty pore. To overcome this challenge and enable NW growth (as described in Chapter 3), after Au evaporation, the template had to be glued onto a conducting copper tape. This tape helped close the pores with a metal. This was a major challenge, since in some cases, the electrolyte solution reacted with the glue and the solution leaked onto the copper tape resulting in clustered growth on the

tape. This challenge resulted in experimental results that were not reproducible. On the off-chance that thermal evaporation was too aggressive for coating metal on AAO membranes, attempts were made to commercially plate the AAO templates by e-beam evaporation where ($\sim 500\ nm$) was e-beam evaporated onto the back surface of the AAO membrane. However, the results were the same and the metal did not close the pores as shown in Figure 5.2.

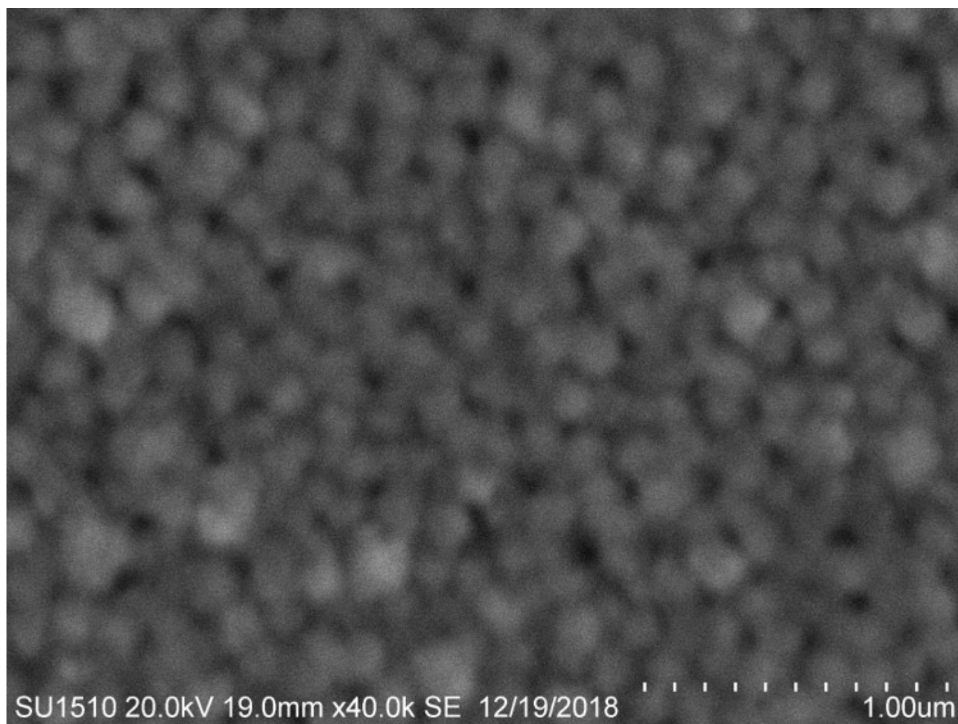

FIGURE 5.2. SEM images of bottom surfaces of AAO template after ($\sim 500\ nm$) e-beam evaporated Au thin film. We can clearly see that pores are not completely filled.

Another important challenge with AAO templates is that the pore interiors are not smooth. This results in the grown NWs having rough surfaces as shown in Figure 5.3.

2. In the case of polycarbonate membranes, the pore sizes are not uniform ($\sim$150 - 200 nm range) and the pore density is rather low, as shown in Figure 5.4

Moreover, the flexibility of the PC membranes results in NWs that are either polycrystalline or with high density of structural defects, as discussed in Chapter 4. It is also important to control the temperature (lower the temperature) during metal evaporation, since at high temperatures, the flexible membrane melts and crumples up.

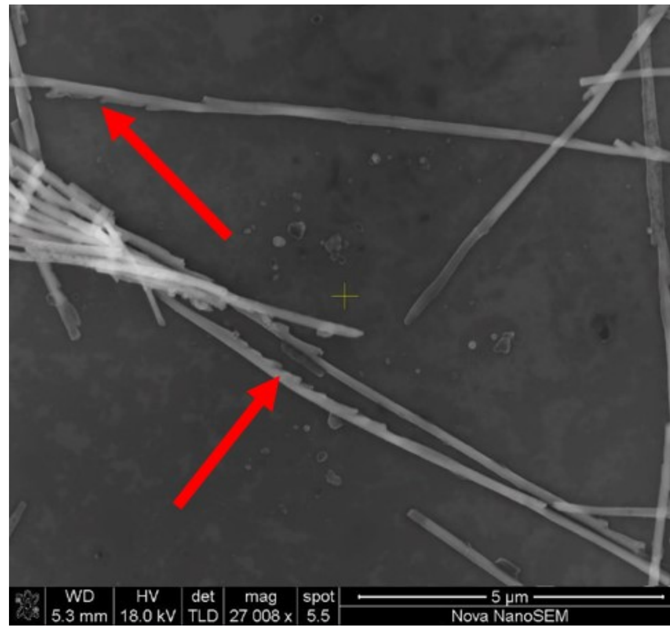

FIGURE 5.3. SEM images of InSb NW grown in AAO template. Rough notched on the surface of NWs are shown by red arrows comes from the morphology of interior of AAO template

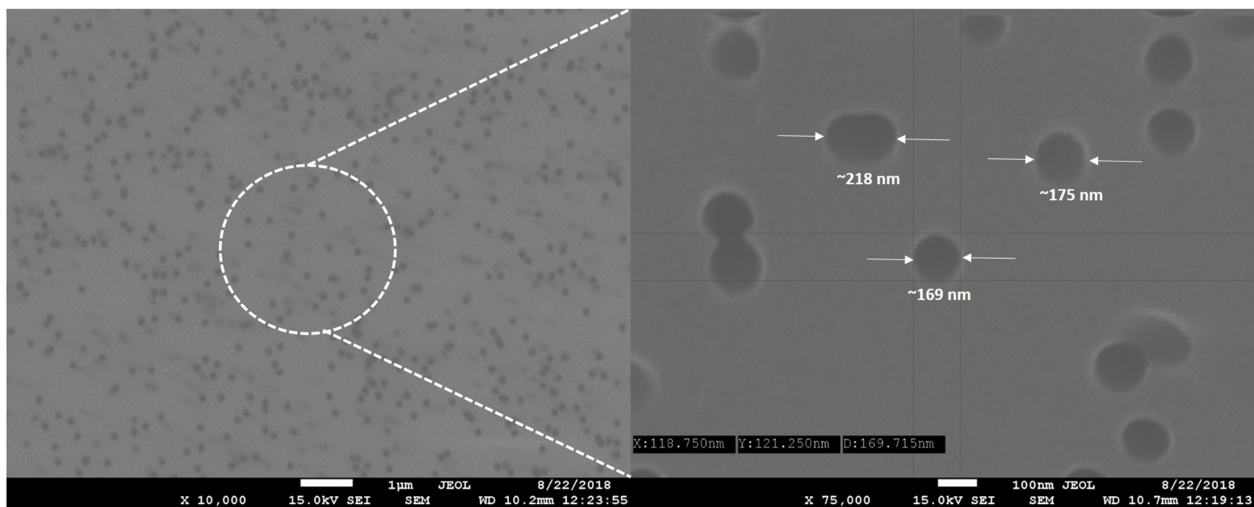

FIGURE 5.4. SEM image of polycorbonate (PC) template, zoomed in image shows the non-unoform pores of PC temnplate where pore are ranging from $\sim$ 150 to 200 nm in diameter.

NW growth in the commercially available templates helped establish the NW growth recipe and provided interesting results on structure, composition and dependence of stoichiometry on growth parameters. On account of the challenges discussed above, this chapter

presents work on home-made AAO templates. The advantage of this home-grown template technique is the fact that the bottom electrode is the Al foil that is used for template fabrication. This eliminates the need to evaporate a metal over the back-surface to function as the working electrode. Moreover, by growing the template in the lab, it became possible to tune the pore diameter and length [116, 117].

5.2. Fabrication Method

To obtain a higher control of the NW dimensions and surface quality, an electrochemical self-assembly technique was used to fabricate a hexagonally ordered array of cylindrical nanopores on an aluminum substrate. Starting with high purity, unpolished and annealed aluminum (99.997 %, AlfaAsar) foil with thickness of $\sim 250\ \mu$m, the unpolished samples were first chemically polished [118] using 15 parts of 68% nitric acid and 85 parts of 85% phosphoric acid for 5 min at 85^0 C as shown in Figure 5.5(a) just after chemical polishing. Figure 5.5 shows the different stages of fabrication of AAO template.

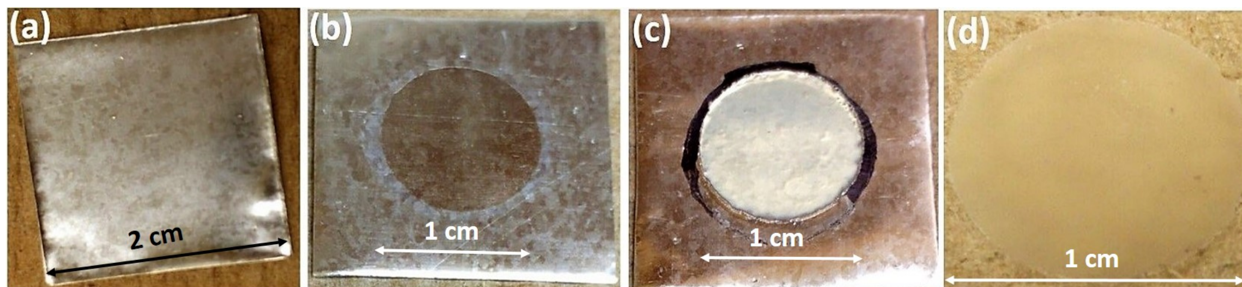

FIGURE 5.5. Optical images of 2×2 cm^2 aluminum coupon at different stages of fabrication process of home-made AAO template (a) just after chemical polishing for smother surface of aluminum foil, (b) aluminum foil after the first step anodization, (c) aluminum foil after the second step anodization, and (d) circular AAO template separated from the aluminum foil after etching of aluminum using 1M $HgCl_2$ solution.

The samples were then neutralized in 1 M sodium hydroxide (NaOH) for 20 min. This was followed by a multi-step anodization process using 3% oxalic acid and 40 V DC at room temperature. Final step of anodization is carried out for 5 min, which produces

pore length of ∼1 μm [119]. Figure 5.6 shows SEM images of top surface of AAO template after second anodization, Figure 5.6(a) is the SEM images of top surface at a scale bar of 2 μm and Figure 5.6(b) is the top surface with a scale bar with 500 nm which shows the pore diameter of AAO template is ∼ 50 nm.

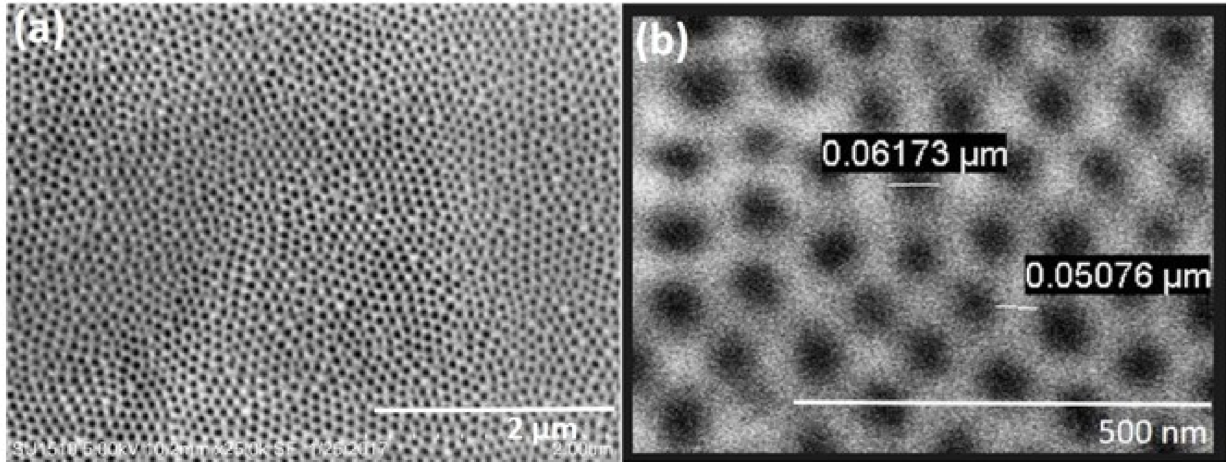

FIGURE 5.6. SEM images of top surfaces of AAO template (a) at scale bar of 2 μm and (b) with scale bar 500 nm in pore diameter which shows that diameter of pore is ∼ 50 nm [3].

After second step anodization, aluminum is dissolved in 1 M mercury chloride ($HgCl_2$) saturated solution. We have achieved ∼ 50 μm pore length in about 4 h 16 min with pore diameter of 50 nm. One advantage for the home-grown route of synthesizing templates is the possibility of obtaining smaller pore diameters. In this chapter, results of pore widths of 50-70 nm are presented, in contrast to the larger diameter 100 nm obtained from the commercial templates. NWs of different diameters will enable a study of its dependence on the electrical, magnetic, and thermoelectric properties of NWs. A noteworthy challenge in homemade AAO templates is the presence of a thin barrier layer comprising aluminum oxide at the bottom of the pore. Following fabrication of the alumina layer and removal of the underlying metallic aluminum, the bottom layer of the template was found to exhibit bulges or protrusions.

Figure 5.7(a) shows an SEM image showing the capped protrusions (hemispherical

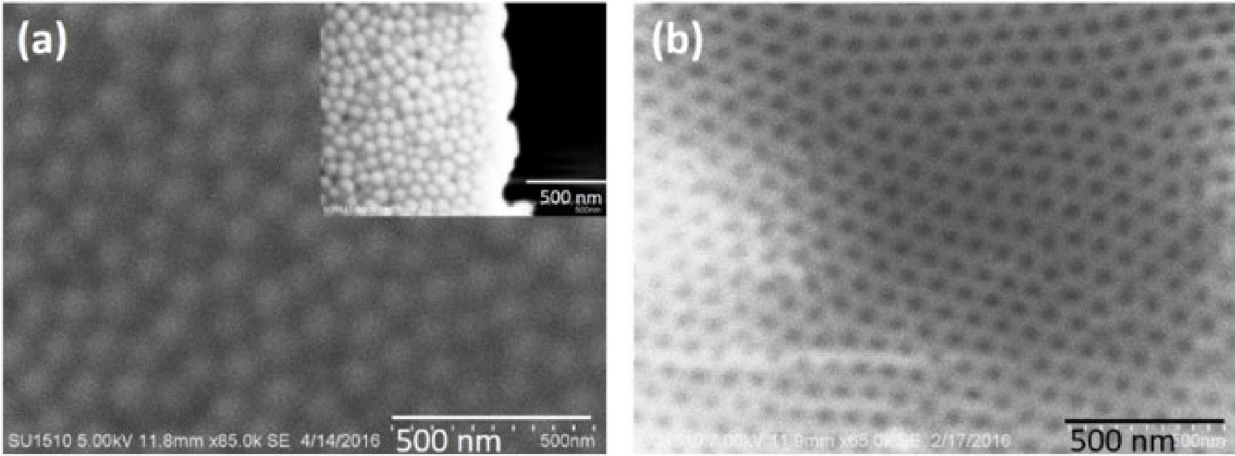

Figure 5.7. SEM images of bottom side of AAO template: (a) hemispherical cap of barrier layer formed during anodization and (b) complete barrier lay er etching in 5% phosphoric acid at 30^0 C for 30 min. [3].

caps) of the barrier later at the bottom of the pore. Inset shows an enlarged image of the barrier caps. Figure 5.7(b) shows the completely opened barrier later after etching in 5% phosphoric acid at 30^0C for 30 min. It has also been observed that if etching time in 5% phosphoric acid is increased from 30 min to 35 min, the thin membrane tears in sections from the top surface and the pores merge together as their walls collapse. Such membranes cannot be used for NW growth via electrodeposition, since the collapsed walls will result in direct contact with the underlying metal layer.

Figure 5.8 shows SEM images of bottom and top surfaces after etching in 5% phosphoric acid (H_3PO_4) for 35 min at 30^0C. Figure 5.8(a) shows the SEM image of bottom surface, which shows all the barrier layers are etched and pores are uniformly open and Figure 5.8(b) shows the SEM image of the same sample as shown in Figure 5.8, which shows over etching of top surface which looks like pores are bundled together.

To check the anodization rate, cross-sectional image of AAO template has been taken at two different times of second anodization, 5 and 250 min, respectively. Figure 15 shows SEM images of cross-section of homemade templates. Figure 15(a) shows 50-µm long pore which was obtained after 250 min of second anodization, and inset shows smooth and straight

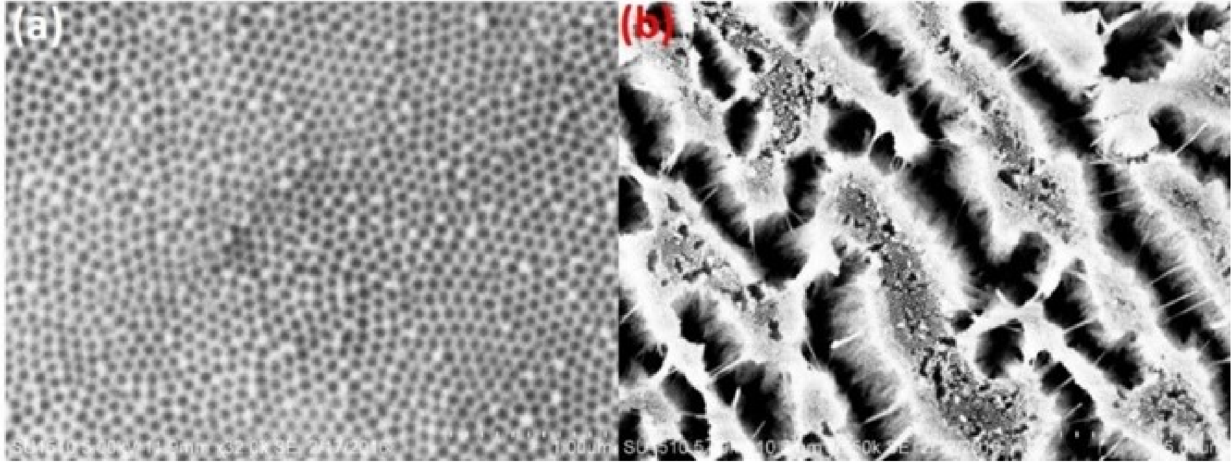

FIGURE 5.8. SEM images of bottom and top surfaces after etching in 5% phosphoric acid (H_3PO_4) for 35 min at 30°C. (a) SEM image of bottom surface, which shows all the barrier layers are etched and pores are uniformly open and (b)SEM image of the same sample as in (a), which shows over etching of top surface which looks like pores are bundled together [3].

pore and; Figure 15(b) shows 5-µm long pore which was obtained after 15 min of second anodization. Based on Figure 15, anodization rate in the above mentioned condition for the growth of homemade AAO template is 1-µm long in 5 min, which is a faster rate than any other anodization conditions reported before [117] .

As mentioned earlier, removal of the barrier layer from the bottom of the AAO membrane is very challenging; if the etching time is not well controlled in most cases, it results in collapse of the tubular walls and destruction of the pores from the top surface of the template.

Results of barrier removal using 1 M H_3PO_4 at 30^0C at different times are presented for comparison. Figure 5.10 shows the SEM images of AAO top surface (a) as-grown and without etching, (b) after 17 min etching in 1 M phosphoric acid at 30°C and (c) after 20 min etching. It is clear from SEM image in Figure 5.10(b) that after 17 min of etching in 1 M phosphoric acid, the AAO template top pores are widened to its maximum capacity, and any increase in etching time will result in merging of the pores. Figure 5.10(c) shows

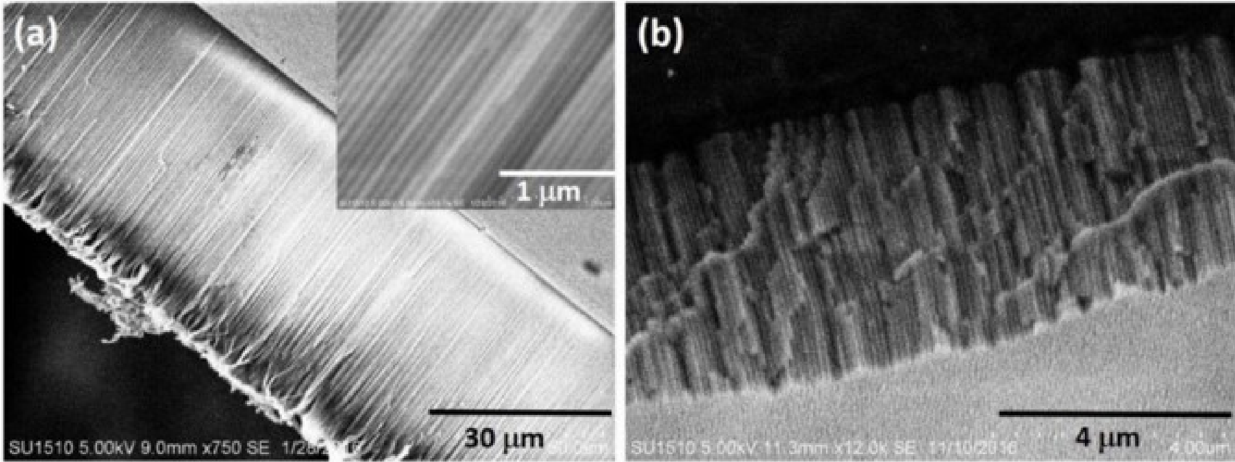

FIGURE 5.9. SEM images of cross-section of home-made AAO template: (a) shows ∼50 μm long pore which was obtained after 250 min of second anodization, and inset shows smooth and straight pore and (b) shows 5-µm long pore which was obtained after 25 min of second anodization [3].

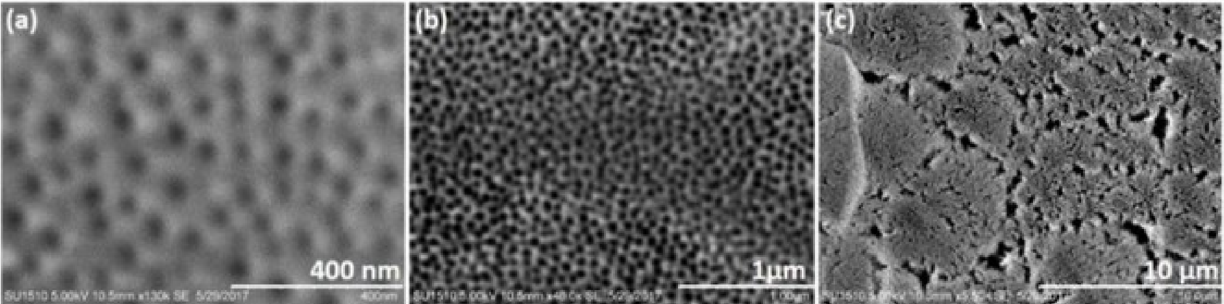

FIGURE 5.10. SEM images of top surface of AAO template: (a) shows non-porous hexagonal AAO pores without any etching, (b) after 17 min etching in 1 M phosphoric acid at 30^0C and, (c) after 20 min etching in 1 M phosphoric acid at 30^0C [3].

that 20 min of etching is over etching and the pores are merged. After appropriate time etching, barrier layer is thinned and pore diameter is widened. Now, pores can be filled with metal (for example cobalt NW) by AC electrochemical deposition using a 5% $CoSO_4.7H_2O$ solution stabilized with 2% H_3BO_3 at 20 V AC and 250 Hz [120].

Barrier layer thinning (BLT) [121] is an alternative technique to remove the barrier layer formed at the end of second anodization process. After thinning of barrier layer,

individual pores terminate in the metallic aluminum layer at the bottom of the template. Such membranes grown directly on aluminum foil are suitable for electrodeposition since the bottom aluminum layer works as one electrode.

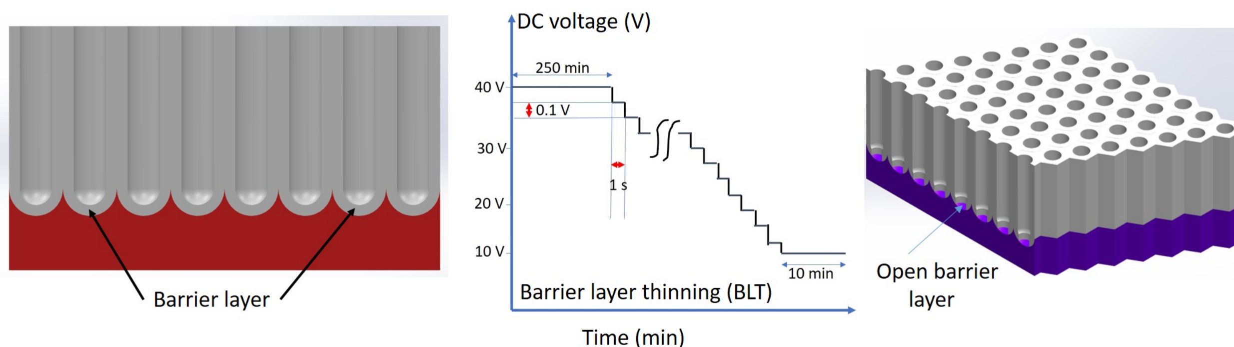

FIGURE 5.11. Schematic plot of voltage reduction steps vs time for thinning/rupturing the barrier layer at the bottom of the AAO pore. First, aluminum (99.999% was anodized (second anodization) for 250 min to grow 50 μm long pore at the rate of 1 μm/5 min at 40 V in 0.3 M oxalic acid ($C_2H_2O_4$) with platinum mesh as a counter electrode at room temperature. afterword, voltage was stepped down from 40 to 10 V in decrements of 0.1 V/ sec.

During the voltage reduction process it is very important to note that if there is fluctuation in voltage (like from 40 to 39.9, 39.8, 39.5 (instead 39.7) etc per sec) then barrier layer thinning will not uniform and it shown in Figure 5.12. Figure 5.12(a) shows partially dark area, which is indicative of onlt that area of barrier layer is open and NWs are grown. Figure 5.12(c) shows the closed pores area. So opening of barrier layer is not uniform.

Non uniform opening of barrier layer as shown in Figure 5.12 was fixed by modifying our home-made power supply which gives nearly 0.1 V/sec. After using this step reduction method and wet etching in 1 M phosphoric acid , which helps to remove the residue at bottom as well as widen the pore size from 50 to 60 nm as shown in Figure 5.13

After that, we remove the aluminum layer and, we were able to see open the barrier layer uniformly in SEM as shown in Figure 5.14. SEM images were taken everywhere on the back side of AAO template after aluminum removal to make sure that the entire back

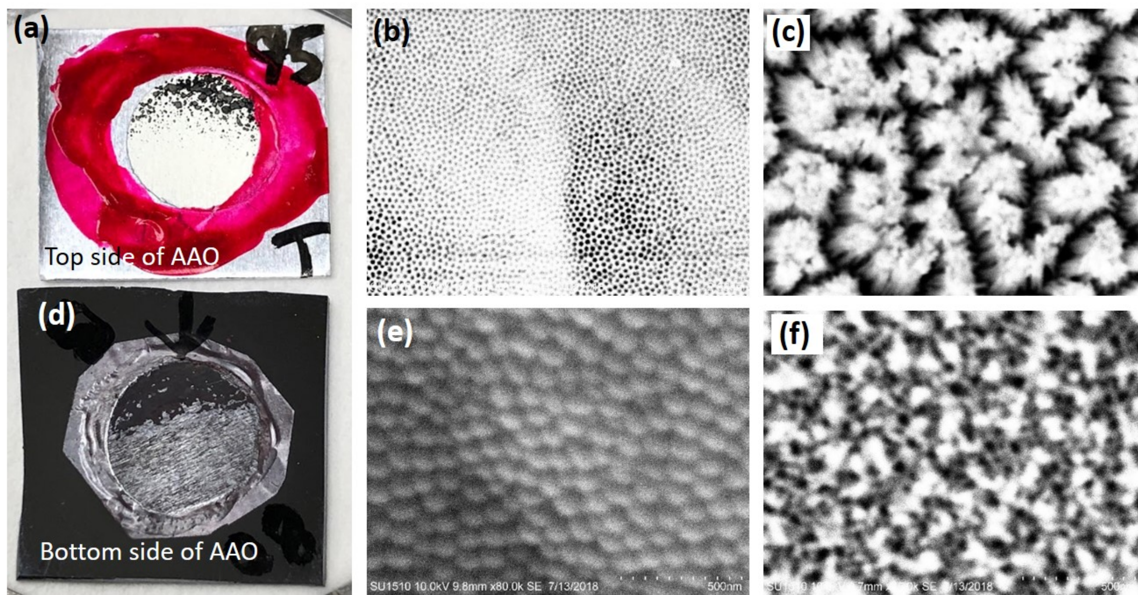

FIGURE 5.12. (a) Optical image of AAO grown on aluminum foil after barrier layer thinning and electrodeposition of InSb NWs, only top portion of AAO is filled with NWs. (b) SEM image of top of the AAO surface where there is no growth of NWs, (c) SEM image of top surface of AAO (black region in (a) after partial etching with phosphoric acid, where bundles of wires are clearly visible, (d) optical image of bottom of the AAO template after aluminum removal in 1 M mercury(II) chloride, white area in (d) is the area where barrier layers (pores) are not open, (e) SEM image of the NW area in (d) where hemispherical closed tips are shown, and (f) SEM image of dark area in (d) where barrier layers are open.

surface of the template is opened - ($\sim$ 1 cm diameter) circular area.

This BLT technique can applied for different kinds of NW growth. For example, it can be used for single NW growth of desired length (1 μm to 50 μm) , as well as heterostructure (like Ni-InS-Co). In this particular home-made template, we can grow the NW of diameter $\sim$ 60–70 nm.

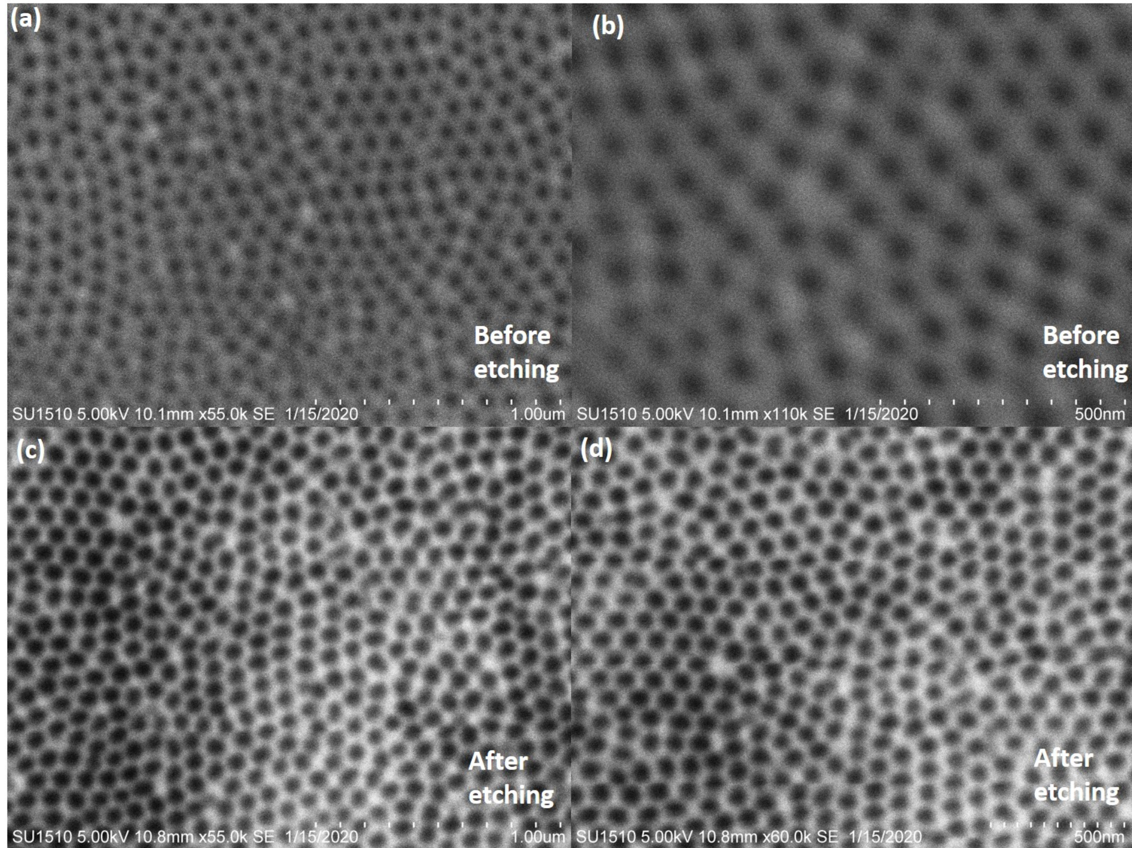

FIGURE 5.13. SEM images of top surface of AAO templates (a) before etching and after 2nd anodization and BLT at scale bar 1 μm, (b) before etching and after 2nd anodization and BLT at scale bar 500 nm, (c) after etching and BLT at scale bar 1 μm, and (d) after etching and BLT at scale bar 500 nm

5.3. Conclusion

Home-made AAO template fabrication process has been discussed in detail using 0,3 M oxalic acid at 40 V dc at room temperature. Before fist anodization, aluminum foil is chemically polished instead of electro-polished, which makes aluminum surface as smooth as RMS $\sim$ 3 nm. This $\sim$ 3 nm roughness is comparable with electro-polished aluminum surface. AAO pore diameter was found to be $\sim$ 50 nm and length can be tuned from $\sim$ 1 μm to 50 μm with the growth rate of $\sim$ 1 μm/5min. Since removal of aluminum layer after 2nd annotation was easy however opening the barrier layer was difficult task. So that, BLT techniques was used to remove the barrier layer. This BLT technique is very useful and

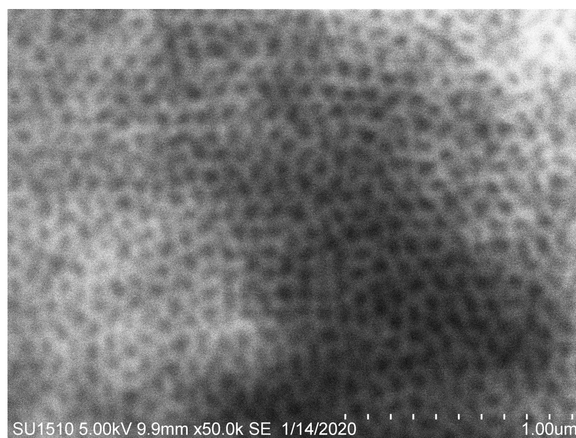

Figure 5.14. SEM image of bottom side of AAO template after aluminum removal in mercuric chloride. All the pores are open and suggesting this technique can be used to grow the NWs directly on anodized aluminum substrate.

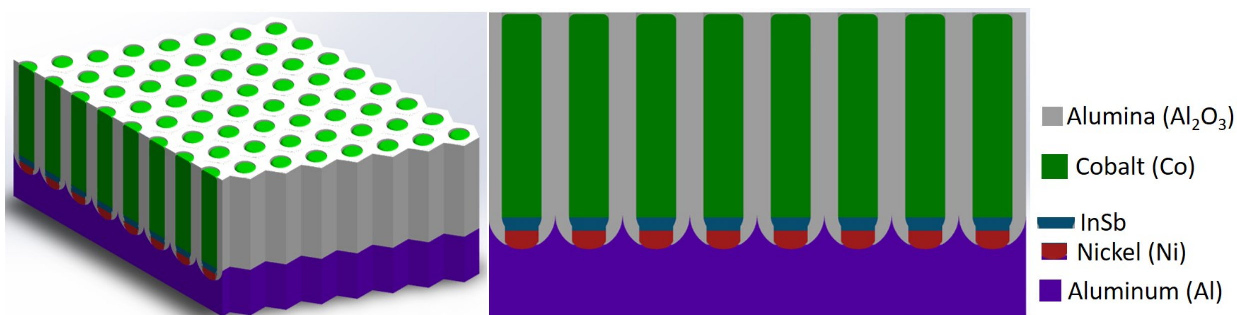

Figure 5.15. Schematics of AAO template (left) after BLT where barrier layers are removed, and cross-section of AAO template after heterostructure (Ni-InSb-Co) NW growth. Length of each NW can be controlled via electrodeposition time.

favorable to grow any metal (Co, Ni etc) or semiconductor (InSb) NWs without coating of conducting layer on free sanding AAO template.

CHAPTER 6

MAGNETIZATION STUDIES OF PURE NICKEL AND COBALT NANOWIRES AND A STUDY OF SPIN-VALVE EFFECT IN NI-INSB-CO HETEROSTRUCTURES

6.1. Introduction

Heterostructures typically comprise of different types of material systems from different groups in the periodic table grown epitaxially over each other. When heterostructures are grown as thin films, matching the lattice constant is very critical. High quality heterojunctions have lattice matched materials stacked on top of one another, failing which there will be stress and strain built up at the interface. This frequently results in stacking faults and other structural defects forming along the NW length. In some cases, lattice mismatching is used to obtain materials with new and interesting properties, where the tensile or compressive strain that is caused by lattice mismatch is exploited for novel applications as in thermoelectrics. In the synthesis of one-dimensional NWs, the constraint of lattice mismatch is relaxed.

This chapter is a study of magnetoresistance effects in arrays of heterostructured NWs. Magnetoresistance is a fundamental phenomena that describes the ability of a material to change its electrical resistance when it is acted on by an external magnetic field. The initial discovery of this phenomenon was by William Thomson, better known as Lord Kelvin, in 1856. However, at that time, the electrical resistance of any material system could not be lowered by more than 5 %. More than a century later, several systems have been developed where a magnetic field can change resistance by orders of magnitude. In 2007, Albert Fert and Peter Grünberg were jointly awarded the Nobel Prize for the discovery of Giant Magnetoresistance effect.

One material system where considerable effort has been invested in is the Co-InSb-Ni system [122, 123, 124, 125]. Such a system is commonly called a spin-valve device. The characteristic of this device is that a spacer layer that is paramagnetic is sandwiched between two ferromagnetic contacts with different coercivities. The spin-valve signal is defined by a

ratio given by the equation:

$$\frac{\Delta R}{R} = \frac{R_{AP} - R_P}{R_P} \tag{25}$$

In this equation R_{AP} and R_P is the device resistance when the two ferromagnets have anti-parallel and parallel spins respectively. If the majority spins in the first ferromagnet (Co) is the same as the majority spin in the second ferromagnet (Ni), then $R_{AP} > R_P$ and the effect is a normal spin-valve effect.

InSb is chosen for this system because it is a narrow band gap group III-V semiconductor and has two important characteristics: (i) strong Rashba spin-orbit coupling, and (ii) large gyromagnetic ratio (g-factor). It is known that in a semiconductor which has majority carriers, the magnetoresistance is proportional to $[1+(\mu B)^2]$, where µ is the carrier mobility and B is the magnetic field. At room temperature, assuming an electron mobility in InSb of ($\approx 4\ m^2/Vs$), it is expected that in a 0.25 T field, the increase in magnetoresistance would be about 100 %.

InSb is therefore considered to be a promising material in applications like the Datta-Das type spin field effect transistor (SPINFET) [126], where the drain-source current can be modulated by a gate potential that changes the Rashba spin-orbit interaction in the transistor channel. The downside of a strong spin-orbit interaction is the rapid spin relaxation. It is desired to have strong spin-orbit interaction but no spin relaxation. To do this, it is best to design the channel as a NW where all the carriers are confined to the lowest conduction sub-band. This allows for strong spin-orbit interaction but weak spin relaxation. The small effective mass of carriers in InSb, its large g-factor and strong Rashba interaction increases the energy separation between sub-bands in InSb and allows for single sub-band occupancy even in relatively large diameter InSb NWs at room temperature.

In this chapter, the synthesis of arrays of Co-InSb-Ni NWs is presented. The $\approx$ 175 nm thick NWs were synthesized by sequentially electrodepositing Ni , InSb and Co in the pores of a flexible polycarbonate template membrane. A schematic representation of the heterostructure is shown in Figure 6.1.

The length is each NW in the array is about 20 μm long corresponding to the thickness

of the PC membrane. It is estimated that the Co section of the NW is about 16 μm, InSb is about 1 μm and Ni is about 3 μm long. Each heterostructured NW is expected to act as a "spin-valve", where one of the ferromagnetic contact "Co" injects spin-polarized electrons into the semiconductor (InSb).

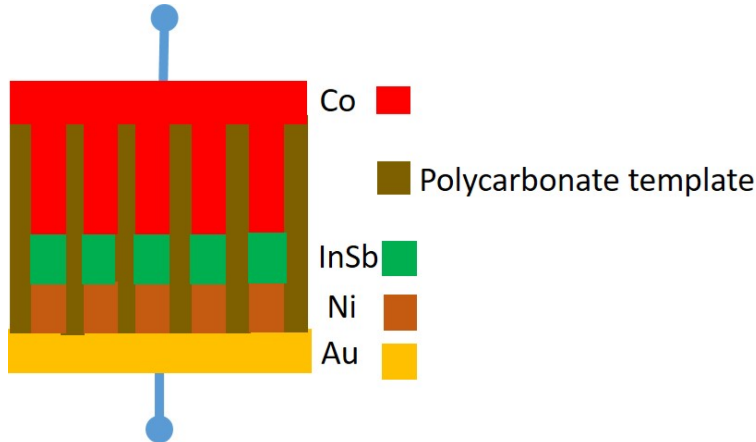

FIGURE 6.1. Schematic diagram of an InSb spin-valve device. Bottom layer is coated with gold thin layer before electrodeposition of the NWs. Top and bottom contact were using metal wire to connect external circuit.

This injection possibly occurs by tunneling of the electrons through the Schottky barrier formed at the Co-InSb interface. If the length of the semiconductor is kept small enough, the second ferromagnetic contact (Ni) transmits the electrons to varying degrees depending on their spin. The first contact is the injecting contact which acts as a spin polarizer while the second contact is the detecting contact that acts as a spin analyzer. Considering that the PC membranes do not have a homogeneous, high-density pore distribution, it is estimated that $\approx 10^6$ NWs are electrically contacted from top to bottom, thereby defining an assembly of 10^6 resistors in parallel. Each heterostructure represents a single NW spin-valve where the total spin-valve resistance comprises of three resistances in series: resistance of the injecting ferromagnetic contact, the InSb NW spacer and the resistance of the detecting ferromagnetic contact. Considering the metallic nature of the ferromagnets, it is obvious that the InSb NW resistance dominates the total resistance.

6.2. Analysis of The Magnetic Properties of Ni and Co NWs

The Au coated PC membrane was used to first grow about 3 μm of Ni NW. The Ni NWs were electrodeposited using an electrolyte containing 0.457 M M $NiSO_4 7H_2O$, and 0.728 M M H_3BO_3 [127, 128, 129, 130, 131, 132] under -1.0 V dc in three electrode configuration in potentiostatic mode. The pH value of electrolyte was adjusted to about 2.2 for Ni NW growth. An Ag/AgCl reference electrode was combined into a three-electrode system, in which a platinum mesh electrode served as a counter electrode for DC electrodeposition. A separate Au coated PC membrane was used for growth of Co NWs following the same procedure at -1.0 V. The electrolyte for Co NW growth was lectrolyte containing 0.18 M $CoSO_4 7H_2O$, and 0.5 M H_3BO_3 [30, 127, 133, 134, 135, 136, 137, 138] .

6.2.1. Magnetic Measurements of Ni NWs

A schematic of the Ni NW array grown in PC membrane is shown in Figure 6.2.

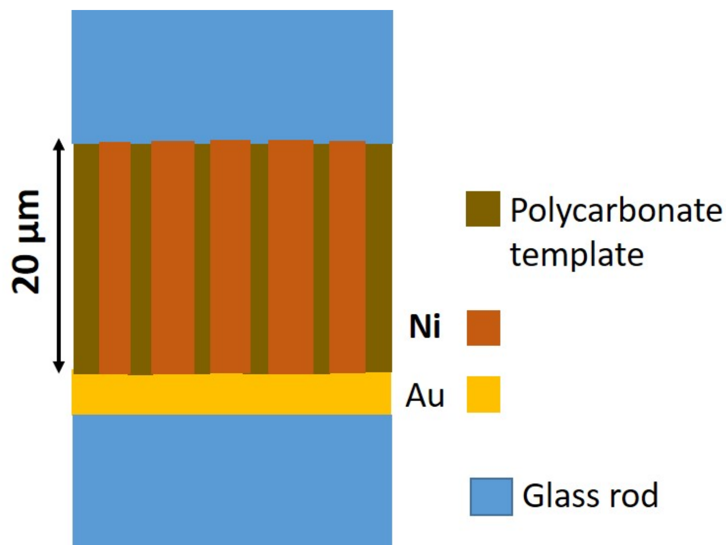

FIGURE 6.2. Schematic of pure Ni NWs, electrochemically grown in $\sim$ 20 μm long pore length of PC template with diameter ranging from $\sim$ 150 nm to 200 nm.

The length of the NWs in this array is 20 μm and they have an average diameter of about 175 nm. An SEM image of the Ni NW array with corresponding EDX measurements is shown in Figure 6.3

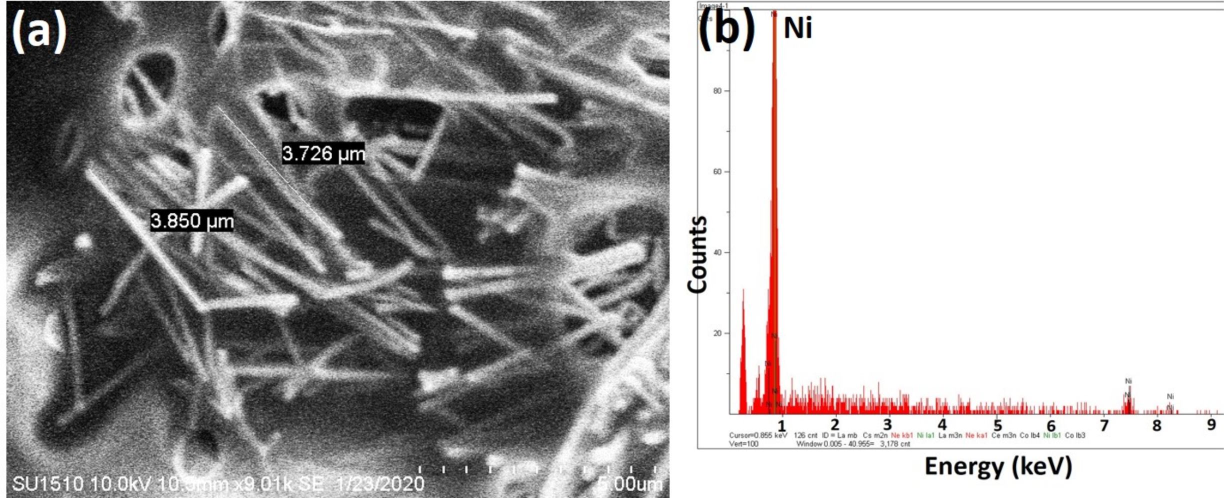

FIGURE 6.3. (a) SEM image of pure Ni NWs electrochemically grown in PC template. (b) EDX spectrum shows only Ni peak.

The array of Ni NWs were characterized for magnetic measurements using the Physical Property Measurement System (PPMS). This instrument incorporates a precision current source and a precision voltmeter allowing for electrical transport measurements at different temperatures (ranging from 4K to 400 K) and different magnetic fields (ranging from -1 Tesla to +1 Tesla). It is known that the magnetic properties of the NW array are directly related to their physical properties. Thin NWs typically show more hysteresis effect. It is also known that coercivity is inversely proportional to NW diameter and directly proportional to its length. So, a thin and long NW will have increased coercivity. For a given NW diameter, the coercivity saturates at a critical value of length. Another factor that affects coercivity is the crystal quality. The magnetization hysteresis loop shown in Figure 6.4 was measured for the Ni NW array embedded in a PC membrane with the magnetic field direction parallel to the axis of the NWs.

As seen in the plot, the coercivity (H_c) and remanent magnetization (M_r) are temperature dependent. At the low temperature of 4K, the ratio M_r/M_s which represents the squareness of the hysteresis of the Ni NWs is about 85 %. This ratio decreases to about 4 % at 300 K. These values are less than those reported [139] for room temperature measurements. This is most likely because our NWs had a larger diameter and at this stage of the

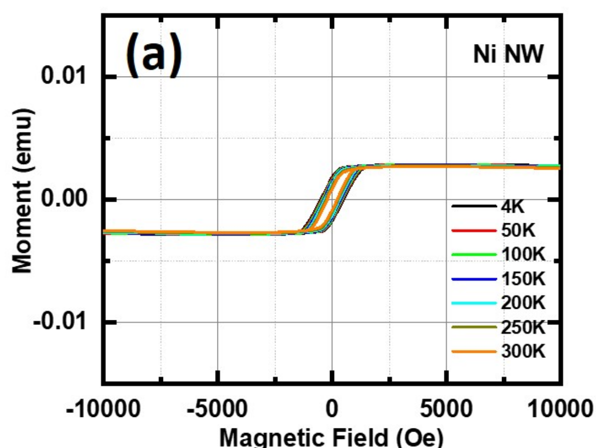

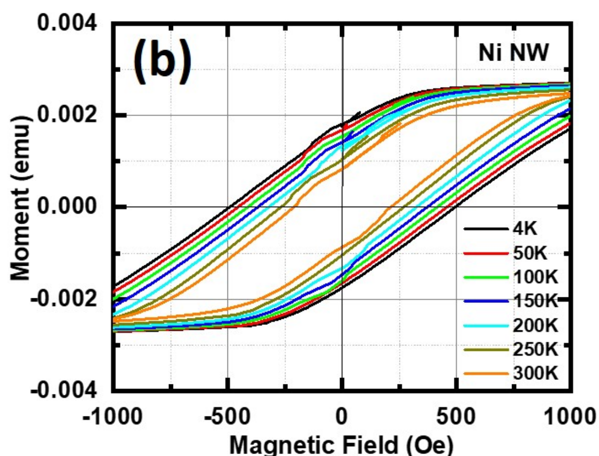

FIGURE 6.4. Magnetization hysteresis curve of Ni NWs array with applied field parallel to the wire axis.Magnetic hysteresis loop of Ni NWs at different temperatures (4, 50, 100, 150, 200, 250, and 300K) (a) magnetic field applied from -10000 Oe to +10000 Oe, (b) Zoomed in data of magnetic field applied from -1000 Oe to +1000 Oe. We can see the coercivity of Ni NWs array is decreasing with increasing temperature.

work, we do not have sufficient information about its crystal structure.This is also refelcted in the fact that the measured coercivity of 500 Oe at 4K and 228 Oe at 300 K is much below the theoreticaly expected value of about 1000 Oe [139].

TABLE 6.1. Coercivity H_c of Ni NW at different temperatures

T(K)	H_c (Oe) (‖)	M_r	M_s	M_r/M_s (‖)
4	500	0.00179	0.0021	0.85238
50	460	0.00166	0.0025	0.664
100	440	0.00153	0.0026	0.58846
150	378	0.00142	0.0026	0.54615
200	246	0.00127	0.0027	0.47037
250	282	0.00103	0.0027	0.38148
300	228	0.000115	0.0028	0.04107

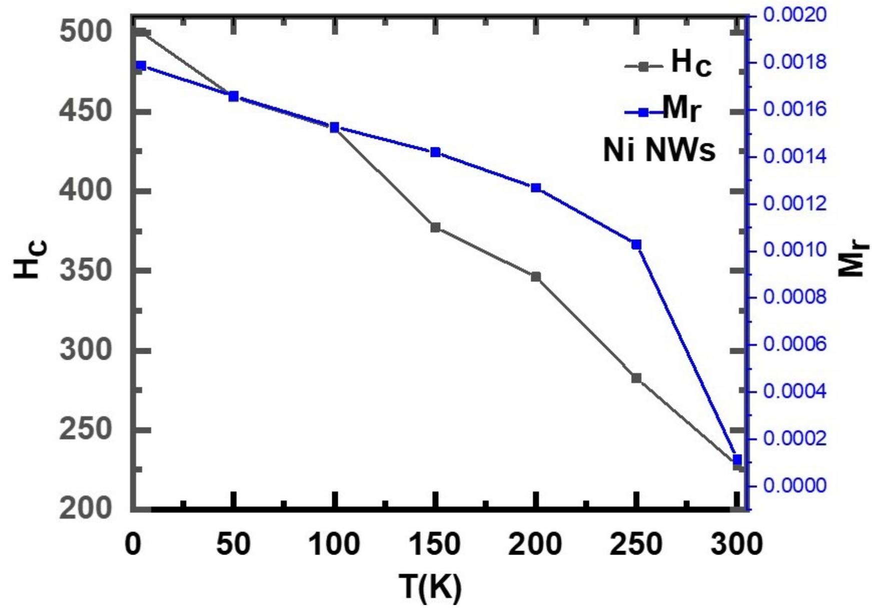

FIGURE 6.5. Magnetization hysteresis curve of Ni NWs array with applied field parallel to the wire axis.

6.2.2. Magnetic Measurements of Co NWs

A schematic of the Co NW array grown in PC membrane is shown in Figure 6.6. The length of the NWs in this array is 20 μm and they have an average diameter of about 175 nm. An SEM image of the Co NW array with corresponding EDX measurements is shown in Figure 6.7

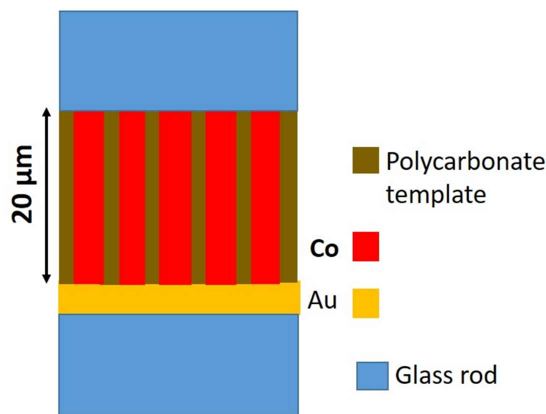

FIGURE 6.6. Schematic of pure Co NWs, electrochemically grown in ~ 20 μm long pore length of polycarbonate (PC) template with diameter ranging from ~ 150 nm to 200 nm.

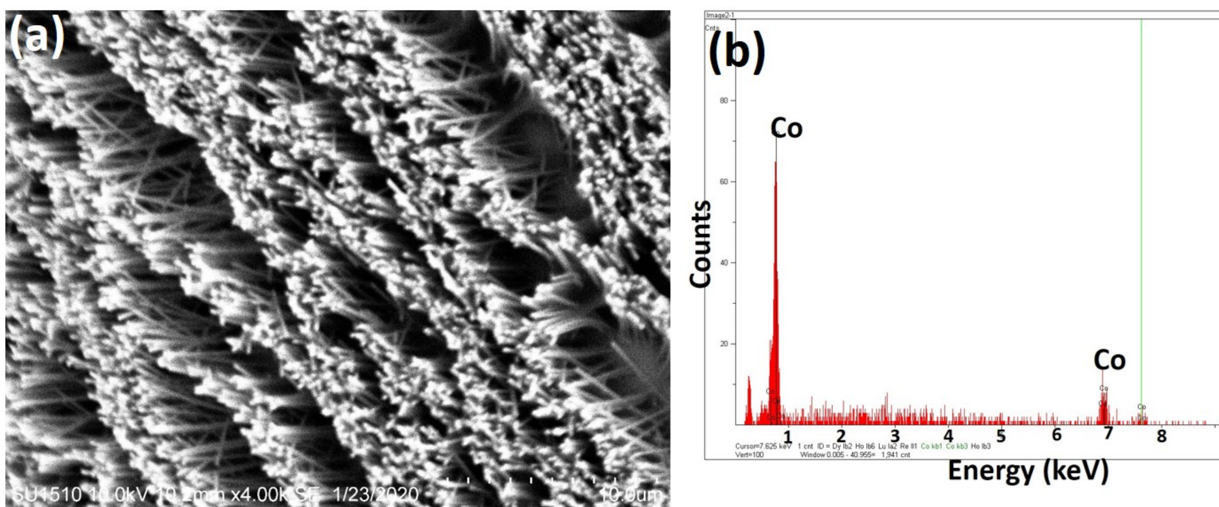

FIGURE 6.7. (a) SEM image of pure Ni NWs electrochemically grown in PC template. (b) EDX spectrum shows only Ni peak.

The array of Co NWs were characterized for magnetic measurements using the Phys-

ical Property Measurement System (PPMS) in similar conditions as Ni NWs. The magnetization hysteresis loop shown in Figure 6.8 was measured for the Co NW array embedded in a PC membrane with the magnetic field direction parallel to the axis of the NWs.

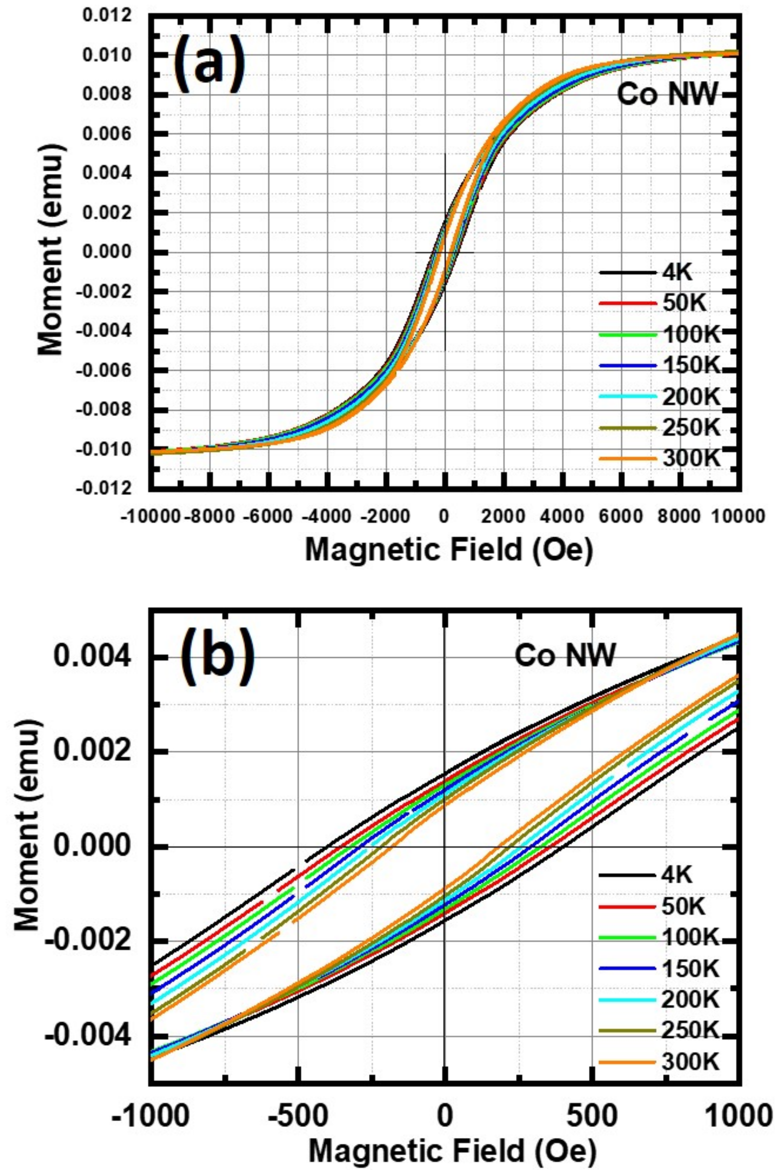

FIGURE 6.8. Magnetization hysteresis curve of Co NWs array with applied field parallel to the wire axis. Magnetic field is applied parallel to the NW axis. (a) Hysteresis curve from -1 T to +1 T, (b) zoomed in version of data between -0.5 T to +0.5 T.

Table 6.2. Coercivity H_c of Co NW at different temperature

T(K)	$H_c(Oe)(\|\|)$	M_r	M_s	M_r/M_s
4	398.99	0.00156	0.00956	0.16318
50	352.02	0.00142	0.00956	0.14854
100	318.28	0.00131	0.00956	0.13703
150	287.27	0.00121	0.00956	0.12657
200	255.81	0.00109	0.00956	0.11402
250	219.33	0.001	0.00956	0.1046
300	180.11	0.000871	0.00956	0.09111

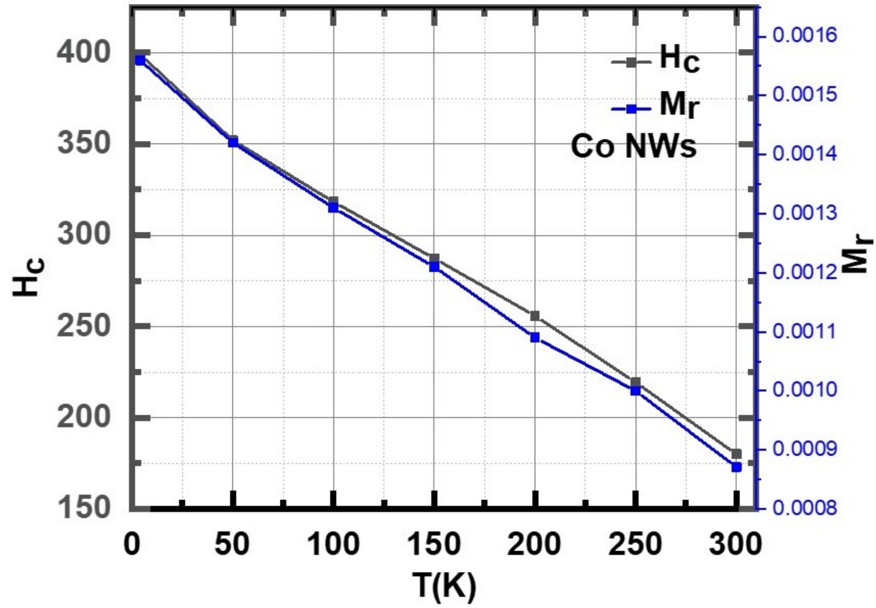

Figure 6.9. Temperature dependence of remnant magnetization(M_r) coercive field (H_C) of Co NWs array.

Similar to the discussion about Ni NWs, the array of Co NWs also showed less than expected values for M_r/M_s (squareness of the hysteresis plot) [139]. The coercivity of the Co NW array (400 Oe at 4K and 180 Oe at 300 K) is also significantly lower than those reported based on theoretical estimates [139]. It has been reported before that increasing

the diameter of the NW, coercivity decreases [140, 141]. Since, our NWs average diameter is about 175 nm compared to the reported values where diameter ranges from 20 to 78 nm. So less coercive field is expected in our NWs.

6.3. Fabrication Method of Spin-Valve Device (Ni-InSb-Co)

As discussed in section 4.2, InSb NWs were grown in PC template. Fow spin valve device, it is essential to have a heterostructure where the semiconductor is sandwiched between two ferromagnetic materials. This is why a tri-layer comprising of Ni-InSb-Co is considered for studying the spin-valve behavior. So first Ni NWs were grown at the bottom of pores of PC template that is coated with thin Au film. This growth is followed by growth of InSb NWs and terminated with the growth of Co over the InSb NWs.

6.4. Extraction of the Spin Diffusion Length in Co-InSb-Ni NWs

In Figure 6.1, a Schottky barrier exists at the Co-InSb and the InSb-Ni interface. When an electrical bias is applied to the device, carriers are injected from Co into InSb by tunneling. Let the spins have a polarization P_1. It is expected that the width of the Schottky barrier is narrow enough to preserve the spin signature of the injecting ferromagnet (Co). After spin injection, the carriers drift and diffuse through the InSb (spacer) with an exponentially decaying spin polarization expressed as $P_1\ exp[-L/L_s]$ where L and L_s represent the length of the InSb region (spacer length) and the average spin relaxation length respectively. Following this, the carriers have to cross a second interface where the Ni contact has polarization P_2. An equation called the Julliere formula is used for determination of spin relaxation length (L_s).

$$\frac{\Delta R}{R} = \frac{2P_1P_2exp(-L/L_s)}{1 - P_1P_2exp(-L/L_s)} \tag{26}$$

In this model the loss of any spins across the two interfaces are ignored.

In equation 25, if $R_{AP} < R_P$, it produces a negative spin-valve peak (-ΔR). This so-called 'trough' is a manifestation of 'inverse spin-valve' effect.

6.5. Working of The Spin-Valve Device

Spin-valve device set-up is shown in Figure 6.1 , where PC template embedded with tri-layer (Ni-InSb-Co) was attached to resistivity puck. Before connecting the resistivity puck to Quantum Design PPMS DynaCool, I-V was taken using semiconducting device parameter analyzer (Agilent B1500A) while resistivity puck is attached to sample wiring test station in voltage source configuration. Room temperature device resistance was measured as $\sim 17\ \Omega$.

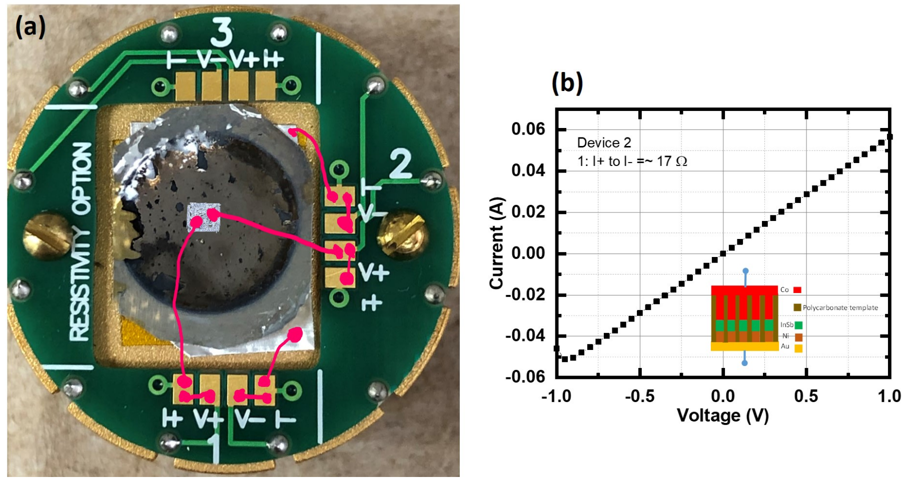

FIGURE 6.10. (a) shows the sample holder and electrical connections and (b) shows the I-V curve at the room teplerature.

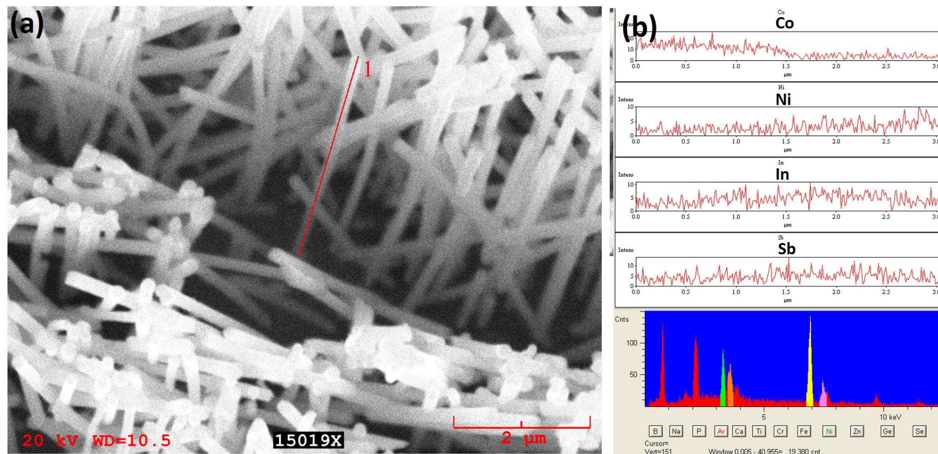

FIGURE 6.11. Inverse spin valve effect at 4K. This data was collected at a bias current of 10 μA

Initially, the device (Co-InSb-Ni) is placed in a high magnetic field. It should be noted

that Co and Ni have different coercivities. At high fields, both Co and Ni are magnetized in the direction of the field. This means their spins are parallel and the device exhibits low resistance. As the magnetic field is reduced and reversed, the ferromagnet with the lower coercivity (nickel) reverses its magnetization. This causes an anti-parallel configuration between the two ferromagnets, thereby increasing the device resistance. Further increase in the magnetic field in the reverse direction causes the second ferromagnet (Co) to reverses its spin as the coercive field is exceeded. This again results in parallel spins and low device resistance. The change in device resistance from low - high - low results in a peak in the magnetoresistance which occurs between the coercive fields of the two ferromagnets. The height of this spin-valve peak above the background resistance is defined by the quantity ΔR.

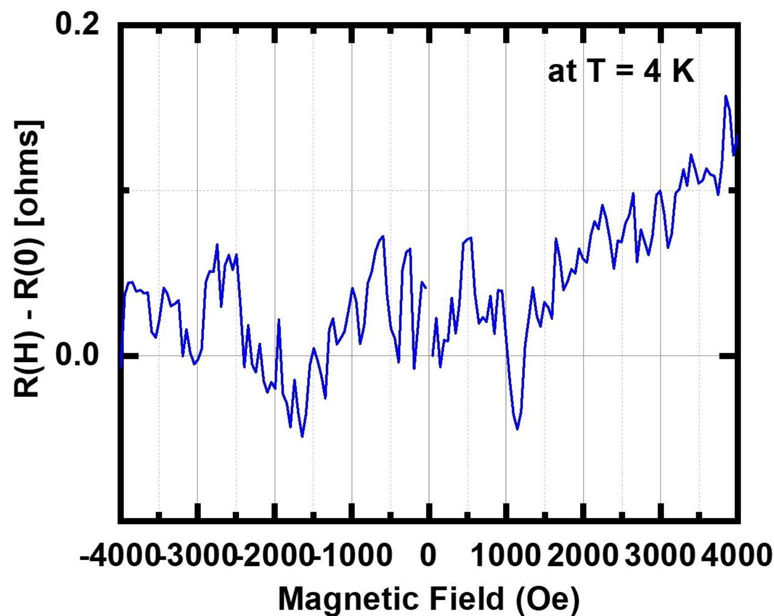

FIGURE 6.12. Inverse spin valve effect at 4K. This data was collected at a bias current of 10 μA

6.5.1. Device Characterization: Magnetoresistance (Spin-Valve) of Ni-InSb-Co NWs

As shown in Figure 6.12, at the low temperature of 4K, there is some evidence of an inverse spin-valve effect. This effect is not observed at room temperature. At this stage of the work, it is not possible to make a firm assertion about our experimental results. This

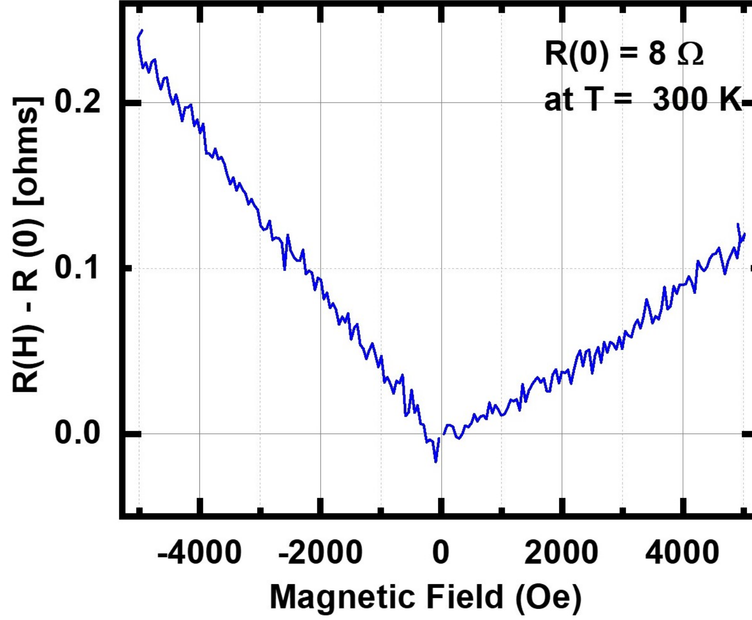

Figure 6.13. Inverse spin valve effect at room temperature (300K). This data was collected at a bias current of 10 μA

is most likely due to: (i) the InSb spacer length and diameter is much greater than those previously reported. In these reports, the InSb length and diameter are 50 nm and 60 nm respectively. In contrast, in our experiment, the InSb length is about 1 μm and diameter is about 175 nm. Since the growth recipe is now established, future work entails growth of this heterostructure in the home-made template where the length of the NWs will be kept about 1 μm and the InSb will be grown for 30 s to ensure a length of a few nms.

Based on the experimental results, an attempt was made to determine the magnetoresistance from equation 26 Using P_1 and P_2 of 0.33 and 0.42 respectively, for the InSb lenght of 1 μm, the spin relaxation length is also of the same order of magnitude ($L_s \approx 1.1$ μm.) This value is orders of magnitude higher than the expected spin relaxation length of tens of nm.The most likely reason for the over estimated lenght is the actual spacer length which means that more than one sub-band is populated with carriers and the magnetic signature is far more complex.

CHAPTER 7

CONCLUSION

7.1. Contributions

The objective of this thesis was to demonstrate the efficacy of electrodeposition as the growth technique for the mass production of NWs, specially those made of compound semiconductors of the III-V group. This growth technique is justified because NW growth occurs at room temperature and the experimental variables that could affect crystal growth and stoichiometry are controllable parameters. The major contributions of this work are listed below:

7.2. First Focus: InSb NW Growth in AAO Template, Highlighting Growth Mechanism and Influence of Electrolyte on NW Stoichiometry and Morphology

The first part of this dissertation work is demonstrating growth of InSb NWs in a commercial nano-channel anodic aluminum oxide template (AAO) template. This part involved a detailed study of the various mechanisms of mass transport during successive stages of the NW growth process. InSb NW growth was governed mainly by the process of diffusion. The diameter of the NWs were determined by the diameter of the pores in the AAO template. An interesting contribution of this work was the fact that experiments showed the dependence of NW stoichiometry on the pH of the electrolyte. As a result, the 100 nm thick InSb NWs that were grown using an electrolyte of pH 1.7 were found to be rich in antimony (Sb). The most likely reason for this is the possibility that a lower-pH (1.7) of the electrolyte favors adsorption of Sb anions on the growing crystal. In an attempt to verify if the excess Sb in the InSb NW acted as active defect centers, a single InSb NW was investigated by connecting the NW in a field-effect-transistor type configuration.The as-grown Sb rich InSb NW showed p-type conduction with a hole concentration of $\sim 1.9{\times}10^{16}$ cm^{-3} and field effect hole mobility of $\sim$ 507 cm$^{2}V^{-1}s^{-1}$. The device had a high on-off current ratio of the order of 10^3. This result is very promising since it demonstrates an ability to obtain high density of p-type InSb NWs without addition of any dopants during crystal formation. This opens

up new opportunities for using these NWs in fabrication of electronic devices. Normally p-type doping in InSb is achieved by using dopants like Carbon. But, these intentionally added dopants act as scattering centers that reduce carrier mobility. It is therefore possible that when NW growth occurs in a low pH electrolyte, the concentration of Sb in the NW increases, and it introduces Sb antisite and In interstitial defects in the growing crystal. This could account for the NW exhibiting p-type FET behavior. The presence of defects were also verified by Raman spectroscopy which showed defect related peak at 145 cm^{-1} along with crystalline peaks at 179 cm^{-1} and 188 cm^{-1}.

The as-grown NWs were also analyzed by temperature-dependent transport measurements which showed thermally activated Arrhenius conduction in the temperature range from 200–325 K, yielding an activation energy of 0.1 eV. This corresponds to activation energy from levels close to the middle of the energy band gap. Another important conclusion drawn from this part of the work is the NW morphology. The NWs were found to have a rough surface which corresponded to roughness of the template pore interior. Such rough surfaces of NWs could prove beneficial in applications where phonon transport needs to be interrupted without affecting electron transport - an important feature of thermoelectrics.

7.3. Second Focus: InSb NW Growth in Polycarbonate Template, With Detailed Study of Effect of Membrane Flexibility on NW Crystallinity

The second contribution of this dissertation work is demonstrating growth of InSb NWs in ion track etched PC template. Following the geometry of the PC membranes, the as-grown NWs were about 10 μm long and about 150 nm thick. Raman spectroscopy on these NWs showed that they were not crystalline and showed strong defect related Raman peak. Further studies were done by high resolution electron microscopy and it showed that there are various mechanisms affecting NW crystallinity. The two different NW structures were (i) NWs that were polycrystalline and (ii) crystalline NWs with high density of stacking faults. The polycrystallinity of the NWs is explained using the 3D 'nucleation-coalescence' mechanism. On the other hand, single crystal NWs with high density of twin defects and stacking faults grow epitaxially by a two-dimensional (2D) nucleation/growth mechanism.

Electrical contacts were established to a single InSb NW, which showed that at low bias, the ohmic current is controlled by charge diffusion from the bulk contacts. At high bias, the current-voltage behavior of the device exhibited the phenomenon of space charge limited current (SCLC). This is attributed to transport through structures with reduced electrostatic screening. A cross-over from ohmic to SCLC occurs at about 0.14 V, yielding a free carrier concentration of the order of 10^{14} cm^{-3}.

7.4. Third Focus: Fabrication of AAO Template with Desired Pore Size and Length Followed by Growth of InSb NWs

Considering the challenges faced in accomplishing NW growth in commercial template pores, this dissertation focused on fabrication of AAO templates staring with an Al foil. Following chemical polishing, the Al foils were anodized in two different stages to obtain a high density of uniform pores with smooth pore interiors. These templates are still attached to the base Al foil through a barrier which obstructs the pore reaching the metal electrode. Following previously reported strategies of pore opening using a voltage step reduction, the oxide barrier was initially punctured and eventually the barrier was completed removed by an acid etch. The advantage of the home-made templates is that it removed the requirement of metal evaporation for functioning as the working electrode. Instead, the Al foil itself served as the electrode. Following template fabrication, the home-made AAO templates were used to grow not such semiconducting InSb NWs, but also metallic magnetic NWs of Co and Ni.

7.5. Fourth Focus: Synthesis of a NW Heterostructure of Ni/InSb/Co for Potential Use as Magnetoresistive (Particularly spin-valve) Devices

In this part of the dissertation work, a recipe to grow heterostructured NWs in home-made and commercial templates was established. Initially, ferromagnetic NWs of Co and Ni were synthesized and their magnetic properties studied for determination of ..... Finally, the spin-valve device comprising of an InSb layer sandwiched between two ferromagnetic layers of Co and Ni were studied for determination of their spin-valve behavior. These results were not conclusive and though there is a weak evidence of inverse spin valve effect at 4K, it is

difficult to assert this with absolute certainty. This is because the InSb NWs in the contacted array were rather long (about 3 μm) and this is much larger than the spin relaxation length reported for InSb, which is about....

7.6. Future Directions

The growth of crystalline InSb NWs using MBE and MOVPE are common with expensive equipment and low yield. In comparison, electrochemical deposition of InSb NWs in templates (AAO and PC) provides high yield, and good quality with easily controllable experimental parameters. This is promising for using this material for sensing and optoelectronic applications in addition to spintronics.

Future work should focus on fabrication of the spin-valve device. The InSb length should be controlled for a more detailed study of the magnetoresistance behavior. It is specially promising to consider experiments in which the magnetic signature of the spin-valve devices can be measured for different InSb lengths and to ascertain at what length the effect is measurable. This would allow for an estimate of the spin relaxation length in InSb. Another focus of future work would be to determine the effect of NW crystallinity on spin-signature.

7.7. Publications and conferences attended during this dissertation work

7.7.1. Refereed publications

A. Singh and U. Philipose, “Understanding the Mechanisms that Affect the Quality of Electrochemically Grown Semiconducting Nanowires,” in Semiconductors - Growth and Characterization, R. Inguanta and C. Sunseri, Eds. Rijeka: InTech, 2018.

A. P. Singh, K. Roccapriore, Z. Algarni, R. Salloom, T. D. Golden, and U. Philipose, “Structure and Electronic Properties of InSb Nanowires Grown in Flexible Polycarbonate Membranes,” Nanomaterials, vol. 9, no. 9, p. 1260, Sep. 2019.

Murthada Adewole, Jingbiao Cui, David Lowell, Safaa Hassan, Yan Jiang, **Abhay Singh**, Jun Ding, Hualiang Zhang, Usha Philipose, and Yuankun Lin , “Electrically tunable, sustainable, and erasable broadband light absorption in graphene sandwiched in Al2O3

oxides," Opt. Mater. Express, vol. 9, no. 3, pp. 1095–1104, Mar. 2019.

Z. Algarni, **A. Singh**, U. Philipose, Z. Algarni, A. Singh, and U. Philipose, "Synthesis of Amorphous InSb Nanowires and a Study of the Effects of Laser Radiation and Thermal Annealing on Nanowire Crystallinity," Nanomaterials, vol. 8, no. 8, p. 607, Aug. 2018.

Z. Algarni, **A. Singh**, and U. Philipose, "Role of chemical potential and limitations of growth kinematics on stoichiometry of indium antimonide nanowires," Mater. Chem. Phys., vol. 219, pp. 196–203, Nov. 2018.

A. Singh, Z. Algarni, and U. Philipose, "Template-Assisted Electrochemical Synthesis of p-Type InSb Nanowires," ECS J. Solid State Sci. Technol., vol. 6, no. 5, pp. N39–N43, Jan. 2017.

Z. Algarni, D. George, **A. Singh**, Y. Lin, and U. Philipose, "Hole-dominated transport in InSb nanowires grown on high-quality InSb films," J. Nanoparticle Res., vol. 18, no. 12, p. 361, Dec. 2016.

B. Mallampati, **A. Singh**, A. Shik, H. E. Ruda, and U. Philipose, "Electro-physical characterization of individual and arrays of ZnO nanowires," J. Appl. Phys., vol. 118, no. 3, p. 034302, Jul. 2015.

7.7.2. Conference: Contributed Oral Presentations

Abhay Singh, Usha Philipose, "Understanding Electrical Conduction Mechanisms in Polycrystalline Indium Antimonide Nanowires Grown in Flexible Polycarbonate Membrane Pores" 2019 MRS Fall Meeting, December 1-6, 2019 in Boston, MA. **A. Singh**, Usha Philipose, "Intrinsic quality of InSb NWs grown in template pores," presented at the APS March Meeting 2019, Boston, Massachusetts , March 4-4, 2019

A. Singh, Usha Philipose, "Electrical transport in semiconducting InSb nanowire grown via electrochemical deposition in anodic alumina oxide template" AVS Texas Chapter conference, Aug 1st–3rd 2018, Texas Christian University.

A. Singh, Usha Philipose, "Challenges in barrier thinning of home-grown anodic aluminum oxide template on aluminum foil," presented at the APS March Meeting 2018, Los Angeles, California, March 5–9, 2018

A. Singh, Usha Philipose, “Role of electrodeposition parameters on stoichiometry of InSb nanowires,” presented at the APS March Meeting 2017, New Orleans, Louisiana, March 13–17, 2017 **A. Singh**, Usha Philipose, “Electrochemically grown InSb nanowires: challenges and growth determined properties,” presented at the APS March Meeting 2015, San Antonio, Texas, March 2–6, 2015

7.7.3. Poster

Abhay Singh, Bhargav Mallampati, Bryan McLaren, Vincent Lopes, Chris Littler, A.J. Syllaios, U. Philipose, ”Temperature dependent resistivity and 1/f noise measurements in ZnO nanowires”, 32nd International conference on the Physics of semiconductors (ICPS), August 10–15,2014, Austin, TX.

7.7.4. Summer School

7th NCN-NEEDS Summer School, Spintronics: Science, Circuits, and Systems, July 23-25, 2014, Purdue University

REFERENCES

[1] news.samsung.com/global, "Samsung electronics' leadership in advanced foundry technology showcased with latest silicon innovations and ecosystem platform – samsung global newsroom," *news.samsung.com/global*, 2020.

[2] J.-P. Colinge and J. C. Greer, "Nanowire Transistors: Physics of Devices and Materials in One Dimension," Apr. 2016.

[3] A. Singh and U. Philipose, "Understanding the Mechanisms that Affect the Quality of Electrochemically Grown Semiconducting Nanowires," *Semiconductors - Growth and Characterization*, Dec. 2017.

[4] R. F. Pierret, "Semiconductor Device Fundamentals," 1996.

[5] A. C. Diebold, D. Venables, Y. Chabal, D. Muller, M. Weldon, and E. Garfunkel, "Characterization and production metrology of thin transistor gate oxide films," *Materials Science in Semiconductor Processing*, vol. 2, pp. 103–147, July 1999.

[6] E. Nicollian and J. Brews, "Metal Oxide Silicon Capacitor at Intermediate and High Frequencies," *MOS (Metal Oxide Semiconductor) Physics and Technology*, pp. 99–175, 1982.

[7] J.-P. Colinge and C. A. Colinge, *Physics of Semiconductor Devices*. Springer US, 2002.

[8] G. Armstrong, J. Davis, and A. Doyle, "Characterization of bipolar snapback and breakdown voltage in thin-film SOI transistors by two-dimensional simulation," *IEEE Transactions on Electron Devices*, vol. 38, no. 2, pp. 328–336, 1991.

[9] K. E. Moselund, D. Bouvet, V. Pott, C. Meinen, M. Kayal, and A. M. Ionescu, "Punch-through impact ionization MOSFET (PIMOS): From device principle to applications," *Solid-State Electronics*, vol. 52, no. 9, pp. 1336–1344, 2008.

[10] Q. Zhang, W. Zhao, and A. Seabaugh, "Low-subthreshold-swing tunnel transistors," *IEEE Electron Device Letters*, vol. 27, no. 4, pp. 297–300, 2006.

[11] H. Lu and A. Seabaugh, "Tunnel Field-Effect Transistors: State-of-the-Art," *IEEE Journal of the Electron Devices Society*, vol. 2, no. 4, pp. 44–49, 2014.

[12] A. Afzalian, J.-P. Colinge, and D. Flandre, "Physics of Gate Modulated Resonant

Tunneling (RT)-FETs: Multi-barrier MOSFET for steep slope and high on-current," *Solid-State Electronics*, vol. 59, May 2011.

[13] S. Salahuddin and S. Datta, "Use of Negative Capacitance to Provide Voltage Amplification for Low Power Nanoscale Devices," *Nano Letters*, vol. 8, no. 2, pp. 405–410, 2008.

[14] V. V. Zhirnov and R. K. Cavin, "Negative capacitance to the rescue?," *Nature Nanotechnology*, vol. 3, pp. 77–78, Feb. 2008.

[15] S. Salahuddin and S. Datta, "Can the subthreshold swing in a classical FET be lowered below 60 mV/decade?," in *2008 IEEE International Electron Devices Meeting*, pp. 1–4, Dec. 2008. ISSN: 2156-017X.

[16] R. Dennard, F. Gaensslen, V. Rideout, E. Bassous, and A. LeBlanc, "Design of ion-implanted MOSFET's with very small physical dimensions," *IEEE Journal of Solid-State Circuits*, vol. 9, no. 5, pp. 256–268, 1974.

[17] S. A. Dayeh, D. P. R. Aplin, X. Zhou, P. K. L. Yu, E. T. Yu, and D. Wang, "High Electron Mobility InAs Nanowire Field-Effect Transistors," *Small*, vol. 3, no. 2, pp. 326–332, 2007.

[18] I. Žutić, J. Fabian, and S. Das Sarma, "Spintronics: Fundamentals and applications," *Reviews of Modern Physics*, vol. 76, no. 2, pp. 323–410, 2004.

[19] D. D. Awschalom and M. E. Flatté, "Challenges for semiconductor spintronics," *Nature Physics*, vol. 3, no. 3, pp. 153–159, 2007.

[20] K.-I. Chen, B.-R. Li, and Y.-T. Chen, "Silicon nanowire field-effect transistor-based biosensors for biomedical diagnosis and cellular recording investigation," *Nano Today*, vol. 6, p. 131, 2011.

[21] R. S. Wagner and W. C. Ellis, "Vapor-liquid-solid mechanism of single crystal growth," *Vapor-liquid-solid mechanism of single crystal growth*, vol. 4, p. 89, 1964.

[22] K. A. Bertness, A. Roshko, N. A. Sanford, J. M. Barker, and A. V. Davydov, "Spontaneously grown GaN and AlGaN nanowires," *Journal of Crystal Growth*, vol. 287, pp. 522–527, Jan. 2006.

[23] K. A. Bertness, A. Roshko, L. M. Mansfield, T. E. Harvey, and N. A. Sanford, "Mechanism for spontaneous growth of GaN nanowires with molecular beam epitaxy," *Journal of Crystal Growth*, vol. 310, pp. 3154–3158, June 2008.

[24] T. Rieger, S. Heiderich, S. Lenk, M. I. Lepsa, and D. Grützmacher, "Ga-assisted MBE growth of GaAs nanowires using thin HSQ layer," *Journal of Crystal Growth*, vol. 353, pp. 39–46, Aug. 2012.

[25] U. Philipose, G. Sapkota, J. Salfi, and H. E. Ruda, "Influence of growth temperature on the stoichiometry of InSb nanowires grown by vapor phase transport," *Semiconductor Science and Technology*, vol. 25, p. 075004, June 2010.

[26] Z. Algarni, A. Singh, and U. Philipose, "Role of chemical potential and limitations of growth kinematics on stoichiometry of indium antimonide nanowires," *Materials Chemistry and Physics*, vol. 219, pp. 196–203, Nov. 2018.

[27] Z. Algarni, A. Singh, and U. Philipose, "Synthesis of Amorphous InSb Nanowires and a Study of the Effects of Laser Radiation and Thermal Annealing on Nanowire Crystallinity," *Nanomaterials*, vol. 8, p. 607, Aug. 2018.

[28] Z. Algarni, D. George, A. Singh, Y. Lin, and U. Philipose, "Hole-dominated transport in InSb nanowires grown on high-quality InSb films," *Journal of Nanoparticle Research*, vol. 18, p. 361, Dec. 2016.

[29] R. M. Penner and C. R. Martin, "Controlling the morphology of electronically conductive polymers," *Journal of The Electrochemical Society*, vol. 133, no. 10, pp. 2206–2207, 1986.

[30] S. Valizadeh, J. M. George, P. Leisner, and L. Hultman, "Electrochemical deposition of co nanowire arrays; quantitative consideration of concentration profiles," *Electrochimica Acta*, vol. 47, no. 6, pp. 865–874, 2001.

[31] C. P. Oliveira, R. G. Freitas, L. H. C. Mattoso, and E. C. Pereira, *Nanostructured Materials Synthesized Using Electrochemical Techniques*, ch. 2, pp. 117–186. John Wiley & Sons, Ltd, 2008.

[32] A. Ghahremaninezhad and A. Dolati, "Diffusion-Controlled Growth Model for Elec-

trodeposited Cobalt Nanowires in Highly Ordered Aluminum Oxide Membrane," *ECS Transactions*, vol. 28, pp. 13–25, Oct. 2010.

[33] S. Blanco, R. Vargas, J. Mostany, C. Borrás, and B. R. Scharifker, "Modeling the Growth of Nanowire Arrays in Porous Membrane Templates," *Journal of The Electrochemical Society*, vol. 161, pp. E3341–E3347, Jan. 2014.

[34] S. Shin, T. T. Al-Housseiny, B. S. Kim, H. H. Cho, and H. A. Stone, "The Race of Nanowires: Morphological Instabilities and a Control Strategy," *Nano Letters*, vol. 14, pp. 4395–4399, Aug. 2014.

[35] W.-C. Yoo and J.-K. Lee, "Field-Dependent Growth Patterns of Metals Electroplated in Nanoporous Alumina Membranes," *Advanced Materials*, vol. 16, no. 13, pp. 1097–1101, 2004.

[36] S. Shin and H. H. Cho, "Self-formed platform for in situ measurement of electrical transport of individual copper nanowires," *Electrochimica Acta*, vol. 117, pp. 120–126, Jan. 2014.

[37] A. M. Mebed, A. M. Abd-Elnaiem, and N. M. Al-Hosiny, "Electrochemical fabrication of 2D and 3D nickel nanowires using porous anodic alumina templates," *Applied Physics A*, vol. 122, p. 565, May 2016.

[38] Y. Feng, K.-D. Kim, C. A. Nemitz, P. Kim, T. Pfadler, M. Gerigk, S. Polarz, J. A. Dorman, J. Weickert, and L. Schmidt-Mende, "Uniform Large-Area Free-Standing Silver Nanowire Arrays on Transparent Conducting Substrates," *Journal of The Electrochemical Society*, vol. 163, pp. D447–D452, Jan. 2016.

[39] M. B. Khedim, L. Cagnon, C. Garagnon, V. Serradeil, and D. Bourgault, "Direct electrical transport measurement on a single thermoelectric nanowire embedded in an alumina template," *Physical Chemistry Chemical Physics*, vol. 18, pp. 12332–12337, Apr. 2016.

[40] C. V. Manzano, G. Bürki, L. Pethö, J. Michler, and L. Philippe, "Determining the diffusion mechanism for high aspect ratio ZnO nanowires electrodeposited into anodic aluminum oxide," *Journal of Materials Chemistry C*, vol. 5, pp. 1706–1713, Feb. 2017.

[41] Y. Konishi, M. Motoyama, H. Matsushima, Y. Fukunaka, R. Ishii, and Y. Ito, "Electrodeposition of Cu nanowire arrays with a template," *Journal of Electroanalytical Chemistry*, vol. 559, pp. 149–153, Nov. 2003.

[42] A. Singh, Z. Algarni, and U. Philipose, "Template-Assisted Electrochemical Synthesis of p-Type InSb Nanowires," *ECS Journal of Solid State Science and Technology*, vol. 6, pp. N39–N43, Jan. 2017.

[43] G. M. X. Zhang, Y. Hao and L. Zhang, "Fabrication of highly ordered insb nanowire arrays by electrodeposition in porous anodic alumina membranes," *J. Electrochem. Soc.*, vol. 152, p. C664, 2005.

[44] M. Heyns and W. Tsai, "Ultimate scaling of cmos logic devices with ge and iii–v materials," *MRS Bull*, vol. 34, p. 485, 2009.

[45] J. V. W. L. M. P. W. V. S. Alexander T. Vogel, Johannes de Boor, "Fabrication of high-quality insb nanowire arrays by chemical beam epitaxy," *Cryst. Growth Des.*, vol. 11, p. 1896, 2011.

[46] C. T. M. L. J. B. W. L.-E. W. L. S. H. Q. X. Henrik A. Nilsson, Philippe Caroff, "Giant, level-dependent g factors in insb nanowire quantum dots," *Nano Lett.*, vol. 9, p. 3151, 2009.

[47] J. M. I. Vurgaftman and L. Ram-Mohan, "Ram-mohan,band parameters for iii–v compound semiconductors and their alloys," *J. Appl. Phys.*, vol. 89, p. 5815, 2001.

[48] A. A. S. D. C. G. D. M. T. E. M. F. D. G. H. K. P. H. M. K. H. R. J. T. M. R. P. W. R. T. R. S. J. S. M. J. U. D. J. W. P. J. W. M. Radosavljevic, T. Ashley and R. Chau, "High-performance 40nm gate length insb p-channel compressively strained quantum well field effect transistors for low-power (vcc=0.5v) logic applications," *J. Appl. Phys.*, pp. 1–4, 2008.

[49] J. del Alamo, "Nanometre-scale electronics with iii–v compound semiconductors," *Nature*, vol. 479, p. 317, 2011.

[50] D. Z. Y. P. C. T. D. S. Suprem R. Das, Collin J. Delker and D. B. Janes, "Room temperature device performance of electrodeposited insb nanowire field effect transistors,"

Appl. Phys. Lett., vol. 98, p. 243504, 2011.

[51] C. D. Y. Z. D. J. J. A. Y. Zhao, D. Candebat and C. Yang, "Understanding the impact of schottky barriers on the performance of narrow bandgap nanowire field effect transistors," *Nano Lett.*, vol. 12, p. 5331, 2012.

[52] S. D. M. E. D. H. K. H. R. J. T. M. T. P. D. W. P. W. T. Ashley, L. Buckle and R. Chau, "Heterogeneous insb quantum well transistors on silicon for ultra-high speed, low power logic applications," *Electron. Lett.*, vol. 43, p. 14, 2007.

[53] K. L. M. M. H. Chen, X. Sun and N. Xi, "Infrared detection using an insb nanowire," *Mater. Devices Conf.*, vol. 09, p. 212, 2009.

[54] X. S. N. X. H. Chen, K.W.C. Lai and M. Meyyappan, *Nano Optoelectronic Sensors and Devices*, vol. pp. 209–224. Cambridge: William Andrew Publishing, Oxford, 2011.

[55] A. Rogalski, "Infrared detectors: status and trends," *Prog. Quantum Electron.*, vol. 27, p. 59, 2003.

[56] A. M. L. S. Q. Y. F. Zhou, J.H. Seol and R. Scheffler, "One-dimensional electron transport and thermopower in an individual insb nanowire," *J. Phys. Condens. Matter*, vol. 18, p. 9651, 2006.

[57] M. P. Y. L. J. S. Q. Y. L. R. F. Zhou, A.L. Moore and L. Shi, "Effect of growth base pressure on the thermoelectric properties of indium antimonide nanowires," *J. Phys. D: Appl. Phys.*, vol. 43, p. 025406, 2010.

[58] L. Y. L. C. Z.-G. Chen, G. Han and J. Zou, "Nanostructured thermoelectric materials: Current research and future challenge," *Prog. Nat. Sci. Mater. Int.*, vol. 22, p. 535, 2012.

[59] A. Weathers and L. Shi, "Thermal transport measurement techniques for nanowires and nanotubes," *Annu. Rev. Heat Transf.*, vol. 16, p. 101, 2013.

[60] N. Mingo, "Thermoelectric figure of merit and maximum power factor in iii–v semiconductor nanowires," *Appl. Phys. Lett.*, vol. 84, p. 2652, 2004.

[61] D. H. S.A. Solin, T. Thio and J. Heremans, "Enhanced room-temperature geometric magnetoresistance in inhomogeneous narrow-gap semiconductors," *Science*, vol. 289,

p. 1530, 2000.

[62] Y. Wu and P. Yang, "Direct observation of vapor-liquid-solid nanowire growth," *J. Am. Chem. Soc.*, vol. 123, p. 3165, 2001.

[63] D. F. L. W. Y. H. P. C. S. Li, N. Kang and H. Xu, "Coherent charge transport in ballistic insb nanowire josephson junctions," *Sci. Rep.*, vol. 6, p. 24822, 2016.

[64] G. Cao and D. Liu, "Template-based synthesis of nanorod, nanowire, and nanotube arrays," *Adv. Colloid Interface Sci.*, vol. 136, p. 45, 2008.

[65] M. Lai and D. Riley, "Templated electrosynthesis of nanomaterials and porous structures," *J. Colloid Interface Sci.*, vol. 323, p. 203, 2008.

[66] A. P. R. G. T. S. M. Martín-González, G.J. Snyder and A. Stacy, "Electrodeposition of highly dense 50 nm bi2te3-ysey nanowire arrays," *Nano Lett.*, vol. 3, p. 973, 2003.

[67] X. C. A. P. A. K. M. S. K. G. S. L. C. Liu, E.I. Gillette and G. Rubloff, "An all-in-one nanopore battery array," *Nature Nanotechnology*, vol. 9, p. 1031, 2014.

[68] G. V. F. O. M. C. L. Malferrari, A. Jagminiene and A. Jagminas, "Alumina template-dependant growth of cobalt nanowire arrays," *Journal of Nanotechnology*, vol. 209, p. 149691, 2009.

[69] J. M. K. Hnida and G. Sulka, "Template-assisted electrodeposition of indium–antimony nanowires – comparison of electrochemical methods," *Appl. Surf. Sci.*, vol. 287, p. 252, 2013.

[70] B. K. H. C. S. Shin, T.T. Al-Housseiny and H. Stone, "The race of nanowires: Morphological instabilities and a control strategy," *Nano Lett.*, vol. 14, p. 4395, 2014.

[71] R. D. W. L. E. G. M. N. A. M. A.I. Hochbaum, R. Chen and P. Yang, "Enhanced thermoelectric performance of rough silicon nanowires," *Nature*, vol. 451, p. 163, 2008.

[72] G. L. K. M. X. Z. R. H. C.K. Chan, H. Peng and Y. Cui, "High-performance lithium battery anodes using silicon nanowires," *Nat. Nanotechnol.*, vol. 3, p. 31, 2008.

[73] C. X. Y. W. R. Y. S. Xu, Y. Qin and Z. Wang, "Self-powered nanowire devices," *Nat. Nanotechnol.*, vol. 5, p. 366, 2010.

[74] Y. Cui and C. Lieber, "Functional nanoscale electronic devices assembled using silicon

nanowire building blocks," *Science*, vol. 291, p. 851, 2001.

[75] J. W. D. S. M.S. Gudiksen, L.J. Lauhon and C. Lieber, "Growth of nanowire superlattice structures for nanoscale photonics and electronics," *Nature*, vol. 415, p. 617, 2002.

[76] J. L. X. Duan, T.-M. Fu and C. Lieber, "Nanoelectronics-biology frontier: From nanoscopic probes for action potential recording in live cells to three-dimensional cyborg tissues," *Nano Today*, vol. 8, p. 351, 2013.

[77] F. W. H.-Y. C. X. S. S. Y. T. H. M. L. C.-Y. W. Z. Yang, N. Han and J. Ho, "Carbon doping of insb nanowires for high-performance p-channel field-effect-transistors," *Nanoscale*, vol. 5, p. 9671, 2013.

[78] J. M. C. B. S. Blanco, R. Vargas and B. Scharifker, "Modeling the growth of nanowire arrays in porous membrane templates," *J. Electrochem. Soc.*, vol. 161, p. E3341, 2014.

[79] V. V. D.A. Bograchev and A. Davydov, "Mass transfer during metal electrodeposition into the pores of anodic aluminum oxide from a binary electrolyte under the potentiostatic and galvanostatic conditions," *Electrochimica Acta*, vol. 207, p. 247, 2016.

[80] S. Shin and H. Cho, "Self-formed platform for in situ measurement of electrical transport of individual copper nanowire," *Electrochimica Acta*, vol. 117, p. 120, 2014.

[81] K. T. H. K. R. K. A. R. N. M. K. Y. M. W. E. H. Y.-L. Chueh, Z. Fan and A. Javey, "Black ge based on crystalline/amorphous core/shell nanoneedle arrays," *Nano Lett.*, vol. 10, p. 520, 2010.

[82] G. B. C.-M. H. S. C. Y. X. Q. W. M. M. S. F. J. Zhu, Z. Yu and Y. Cui, "Optical absorption enhancement in amorphous silicon nanowire and nanocone arrays," *Nano Lett.*, vol. 9, p. 279, 2009.

[83] P. L. X. Z. Y.-L. C. K. T. K. Y. A. J. A. R. D. R. M. W. Z. Fan, R. Kapadia and A. Javey, "Ordered arrays of dual-diameter nanopillars for maximized optical absorption," *Nano Lett.*, vol. 10, p. 3823, 2010.

[84] Y. C. T. S. A. Mohammad, S.R. Das and D. Janes, "Electrodeposition of indium antimonide nanowires in porous anodic alumina membranes," *MicroNano Symp. UGIM*

2010 18th Bienn. Univ., p. 1, 2010.

[85] K. B. M.I. Khan, X. Wang and C. Ozkan, "Templated fabrication of insb nanowires for nanoelectronics," *J. Nanomater.*, vol. 2008, p. 698759, 2008.

[86] H. M. Y. F. R. I. Y. Konishi, M. Motoyama and Y. Ito, "Electrodeposition of cu nanowire arrays with a template," *J. Electroanal. Chem.*, vol. 559, p. 149, 2003.

[87] N. E. D. Z. J. G. V. Wagner, D. Drews and W. Richter, "Raman monitoring of semiconductor growth," *J. Appl. Phys.*, vol. 75, p. 7730, 1994.

[88] K. B. D. G. T. S. Y. Wang, J. Chi and J. Lu, "Field effect transistor based on single crystalline insb nanowire," *J. Mater. Chem.*, vol. 21, p. 2459, 2011.

[89] A. Pinczuk and E. Burstein, "Raman scattering from insb surfaces at photon energies near the E_1 energy gap," *Phys. Rev. Lett.*, vol. 21, p. 1073, 1968.

[90] W. R. W. Kiefer and M. Cardona, "Second-order raman scattering in insb," *Phys. Rev. B*, vol. 12, p. 2346, 1975.

[91] A. M. M. K. K. M. R. D. K. I. Y. C. T. S. M. A. S.R. Das, C. Akatay and D. Janes, "Second-order raman scattering in insb," *J. Appl. Phys.*, vol. 116, p. 083506, 2014.

[92] H. T. N. Wada and S. Morohashi, "Aps march meeting 55, portland, oregon, march 15–19," *American Physical Society*, p. Abstract No.L9.013, 2010.

[93] W. G. Y. C. X. P. E.N. Dattoli, Q. Wan and W. Lu, "Fully transparent thin-film transistor devices based on sno2 nanowires," *Nano Lett.*, vol. 7, p. 2463, 2007.

[94] J. H. Y. Cui, X. Duan and C. Lieber, "Doping and electrical transport in silicon nanowires," *J. Phys. Chem. B*, vol. 104, p. 5213, 2000.

[95] O. Wunnicke, "Gate capacitance of back-gated nanowire field-effect transistors," *Appl. Phys. Lett.*, vol. 89, p. 83102, 2006.

[96] M. J. X. W. X. B. K. N. O. M. O. C. S. Khan, M. Ibrahim; Penchev, "Electrochemical growth of insb nanowires and report of a single nanowire field effect transistor," *Journal of Nanoelectronics and Optoelectronics*, vol. 3, p. 199, 2008.

[97] M. G. B. J. A. Höglund, C.W.M. Castleton and S. Mirbt, "Point defects on the (110) surfaces of inp, inas, and insb: A comparison with bulk," *Phys. Rev. B*, vol. 74,

p. 075332, 2006.

[98] M. McBride, "Environmental chemistry of soils," *Oxford University Press, New York*, 1994.

[99] I. K. V.N. Brudnyi, V.M. Boiko and N. Kolin, "Electrical properties and limiting position of the fermi level in insb irradiated with protons," *Semiconductors*, vol. 38, p. 769, 2004.

[100] X. H. M. Y. Y. W. Y.W. Yang, L. Li and G. Li, "Transport properties of insb nanowire arrays," *Appl. Phys. A*, vol. 84, p. 7, 2006.

[101] S. R. D. et al., "Electrodeposition of insb branched nanowires: Controlled growth with structurally tailored properties," *J. Appl. Phys.*, vol. 116, p. 083506, 2014.

[102] M. S. A. J. Bard and E. S. Licht, *Semiconductor Electrodes and Photoelectrochemistry, Encyclopedia of Electrochemistry*, vol. 139. Cambridge: Cambridge University Press, 2002.

[103] D. Lincot, "Electrodeposition of semiconductors," *Thin Solid Films*, vol. 487, p. 40, 2005.

[104] E. J. P. N. Zech and D. Landolt, "Anomalous codeposition of iron group metals: I. experimental results," *J. Electrochem. Soc.*, vol. 146, p. 2886, 1999.

[105] J. Ortega and J. Herrero, "Thin films by electrochemical methods," *J. Electrochem. Soc.*, vol. 136, p. 3388, 1989.

[106] Y. L. A. M. N. N. D. S. N. T. A. Demishev, S.; Kosichkin, "Raman scattering in amorphous gallium antimonide," *Zh. Eksp. Teor. Fiz*, vol. 104, p. 2881, 1993.

[107] M. T. J. Wihl, M.; Cardona, "Raman scattering in amorphous ge and iii–v compounds," *J. Non Cryst. Solids*, vol. 8, p. 172, 1972.

[108] J. Lannin, "Low frequency raman scattering in amorphous materials: a-ge, a-insb, and a-ge0.5sn0.5," *Solid State Commun*, vol. 11, p. 1523, 1972.

[109] A. S. Z. Algarni and U. Philipose, "Synthesis of amorphous insb nanowires and a study of the effects of laser radiation and thermal annealing on nanowire crystallinity," *Nanomaterials*, vol. 8, p. 607, 2018.

[110] M. E. Toimil-Molares, “Characterization and properties of micro- and nanowires of controlled size, composition, and geometry fabricated by electrodeposition and ion-track technology,” *Beilstein J Nanotechnol*, vol. 3, p. 860, 2012.

[111] S. G. Pandya and M. E. Kordesch, “Characterization of insb nanoparticles synthesized using inert gas condensation,” *Nanoscale Research Letters*, vol. 10, p. 258, 2015.

[112] J. L. et al., “Electrochemical fabrication of single-crystalline and polycrystalline au nanowires: the influence of deposition parameters,” *Nanotechnology*, vol. 17, p. 1922, 2006.

[113] J. K. T. M. M. Tian, J. Wang and M. Chan, “Electrochemical growth of single-crystal metal nanowires via a two-dimensional nucleation and growth mechanism,” *Nano. Lett.*, vol. 3, p. 919, 2003.

[114] J. K. T. E. M. M. Tian, J. Wang and M. H. W. Chan, “Electrochemical growth of single-crystal metal nanowires via a two-dimensional nucleation and growth mechanism,” *Nano Lett.*, vol. 3, p. 919, 2003.

[115] H. E. R. I. S. K. L. K. S. Alagha, A. Shik and S. P. Watkins, “Space-charge-limited current in nanowires,” *J. Appl. Phys.*, vol. 121, p. 174301, 2017.

[116] O. Jessensky, F. Müller, and U. Gösele, “Self-Organized Formation of Hexagonal Pore Structures in Anodic Alumina,” *Journal of The Electrochemical Society*, vol. 145, Nov. 1998.

[117] W. Lee and S.-J. Park, “Porous Anodic Aluminum Oxide: Anodization and Templated Synthesis of Functional Nanostructures,” *Chemical Reviews*, vol. 114, pp. 7487–7556, Aug. 2014.

[118] K. M. Alam, A. P. Singh, S. C. Bodepudi, and S. Pramanik, “Fabrication of hexagonally ordered nanopores in anodic alumina: An alternative pretreatment,” *Surface Science*, vol. 605, pp. 441–449, Feb. 2011.

[119] K. A. S. P. Abhay Pratap Singh, Srikrishna Chanakya Bodepudi, “High Density Integration of Carbon Nanotube Spin Valves,” *IEEE: 2011 International Conference on Nanoscience, Technology and Societal Implications*, pp. 1–4, 2011. ISSN: null.

[120] S.-H. Jeong, H.-Y. Hwang, K.-H. Lee, and Y. Jeong, "Template-based carbon nanotubes and their application to a field emitter," *Applied Physics Letters*, vol. 78, pp. 2052–2054, Mar. 2001.

[121] R. C. Furneaux, W. R. Rigby, and A. P. Davidson, "The formation of controlled-porosity membranes from anodically oxidized aluminium," *Nature*, vol. 337, pp. 147–149, Jan. 1989.

[122] S. Bandyopadhyay, M. I. Hossain, H. Ahmad, J. Atulasimha, and S. Bandyopadhyay, "Coherent spin transport and suppression of spin relaxation in InSb nanowires with single subband occupancy at room temperature," *Small*, vol. 10, no. 21, pp. 4379–4385, 2014.

[123] S. Bandyopadhyay, "Spin transport in nanowires synthesized using anodic nanoporous alumina films," *Multilayer Thin Films - Versatile Applications for Materials Engineering*, 2020.

[124] M. I. Hossain, S. Bandyopadhyay, J. Atulasimha, and S. Bandyopadhyay, "Coherent spin transport in inorganic semiconductor quantum wires," in *Contemporary Topics in Semiconductor Spintronics*, pp. 95–122, WORLD SCIENTIFIC, 2016.

[125] I. van Weperen, S. R. Plissard, E. P. A. M. Bakkers, S. M. Frolov, and L. P. Kouwenhoven, "Quantized conductance in an InSb nanowire," *Nano Letters*, vol. 13, no. 2, pp. 387–391, 2013.

[126] S. Datta and B. Das, "Electronic analog of the electro-optic modulator," *Applied Physics Letters*, vol. 56, no. 7, pp. 665–667, 1090.

[127] T. Ohgai, X. Hoffer, A. Fábián, L. Gravier, and J.-P. Ansermet, "Electrochemical synthesis and magnetoresistance properties of Ni, Co and Co/Cu nanowires in a nanoporous anodic oxide layer on metallic aluminium," *Journal of Materials Chemistry*, vol. 13, pp. 2530–2534, Sept. 2003.

[128] K. Nielsch, R. B. Wehrspohn, J. Barthel, J. Kirschner, U. Gösele, S. F. Fischer, and H. Kronmüller, "Hexagonally ordered 100 nm period nickel nanowire arrays," *Applied Physics Letters*, vol. 79, pp. 1360–1362, Aug. 2001.

[129] H. Zeng, R. Skomski, L. Menon, Y. Liu, S. Bandyopadhyay, and D. J. Sellmyer, "Structure and magnetic properties of ferromagnetic nanowires in self-assembled arrays," *Physical Review B*, vol. 65, p. 134426, Mar. 2002.

[130] K. M. Razeeb, F. M. F. Rhen, and S. Roy, "Magnetic properties of nickel nanowires: Effect of deposition temperature," *Journal of Applied Physics*, vol. 105, p. 083922, Apr. 2009.

[131] Y. Yu, J. Li, J. Wang, X. Wu, C. Yu, T. Xu, B. Chang, H. Sun, and H. Arandiyan, "Orientation Growth and Magnetic Properties of Electrochemical Deposited Nickel Nanowire Arrays," *Catalysts*, vol. 9, p. 152, Feb. 2019.

[132] A. G. N. Sofiah, J. Kananathan, M. Samykano, S. Ulakanathan, N. A. C. Lah, W. S. W. Harun, K. Sudhakar, K. Kadirgama, W. K. Ngui, and J. P. Siregar, "Electrochemical deposited nickel nanowires: influence of deposition bath temperature on the morphology and physical properties," *IOP Conference Series: Materials Science and Engineering*, vol. 257, p. 012032, Oct. 2017.

[133] J. Xu, X. Huang, G. Xie, Y. Fang, and D. Liu, "Fabrication and magnetic property of monocrystalline cobalt nanowire array by direct current electrodeposition," *Materials Letters*, vol. 59, pp. 981–984, Apr. 2005.

[134] G. Tourillon, L. Pontonnier, J. P. Levy, and V. Langlais, "Electrochemically Synthesized Co and Fe Nanowires and Nanotubes," *Electrochemical and Solid-State Letters*, vol. 3, pp. 20–23, Jan. 2000.

[135] I. Minguez-Bacho, S. Rodriguez-López, M. Vázquez, M. Hernández-Vélez, and K. Nielsch, "Electrochemical synthesis and magnetic characterization of periodically modulated Co nanowires," *Nanotechnology*, vol. 25, p. 145301, Mar. 2014.

[136] I. Minguez-Bacho, S. Rodriguez-López, M. Vázquez, M. Hernández-Vélez, and K. Nielsch, "Electrochemical synthesis and magnetic characterization of periodically modulated Co nanowires," *Nanotechnology*, vol. 25, p. 145301, Mar. 2014.

[137] M.-D. Gerngross, J. Carstensen, and H. Föll, "Electrochemical growth of Co nanowires in ultra-high aspect ratio InP membranes: FFT-impedance spectroscopy of the growth

process and magnetic properties," *Nanoscale Research Letters*, vol. 9, no. 1, p. 316, 2014.

[138] Y. Kang, J. Zhao, J. Tao, X. Wang, and Y. Li, "Electrochemical deposition of Co nanowire arrays into self-organized titania nanotubes," *Applied Surface Science*, vol. 254, pp. 3935–3938, Apr. 2008.

[139] H. Pan, B. Liu, J. Yi, C. Poh, S. Lim, J. Ding, Y. Feng, C. H. A. Huan, and J. Lin, "Growth of Single-Crystalline Ni and Co Nanowires via Electrochemical Deposition and Their Magnetic Properties," *The Journal of Physical Chemistry B*, vol. 109, pp. 3094–3098, Mar. 2005.

[140] J. Sarkar, G. G. Khan, and A. Basumallick, "Nanowires: properties, applications and synthesis via porous anodic aluminium oxide template," *Bulletin of Materials Science*, vol. 30, no. 3, pp. 271–290, 2007.

[141] H. Zeng, M. Zheng, R. Skomski, D. J. Sellmyer, Y. Liu, L. Menon, and S. Bandyopadhyay, "Magnetic properties of self-assembled co nanowires of varying length and diameter," *Journal of Applied Physics*, vol. 87, no. 9, pp. 4718–4720, 200.